

SEISMIC INVESTIGATION OF WRENCH
FAULTING AND FRACTURING AT RULISON
FIELD, COLORADO

By
Kjetil Jansen

A thesis submitted to the Faculty and the Board of Trustees of the Colorado School of Mines in partial fulfillment of the requirements for the degree of Master of Science (Geophysics).

Golden, Colorado

Date _____

Signed: _____
Kjetil Jansen

Approved: _____
Dr. Thomas L. Davis
Thesis Advisor

Golden, Colorado

Date _____

Dr. Terence K. Young
Professor and Head,
Department of Geophysics

ABSTRACT

The Reservoir Characterization Project obtained a nine-component, 3D seismic data set at Rulison Field in Western Colorado, during the Fall of 2003. This survey is the first in a series of multicomponent seismic surveys acquired to monitor stress changes associated with reservoir depletion and to better understand the subtle fracture networks that help determine gas migration and accumulation. This thesis presents the characterization of the complex wrench fault network at Rulison Field, and its linkage to enhanced natural fracture zones.

Rulison Field produces out of the Cretaceous Mesaverde tight gas sandstones which have extremely low permeabilities. Economically sustainable gas production from the tight gas sandstones at Rulison is greatly enhanced by the presence of natural fractures. Therefore, locating the fracture networks is of utmost importance as they provide the flow paths necessary for economic gas production. This study shows that the occurrence of natural fractures is linked to the fault geometry, and that tectonic fracturing is the link to gas production at Rulison. Fracture zones are associated with fault trends and areas of deformation such as structural corners and fault intersections. The subtle, yet complex, wrench faults are difficult to detect and are often overlooked in the reservoir interval. To better characterize the faults and fractures at Rulison, a newly developed tool for fault mapping was applied. The Ant Tracker algorithm™ analyzes

™ Trademark of Schlumberger

all spatial discontinuities in the seismic data and extracts surfaces likely to be faults. The Ant Tracer provides a powerful 3-D automated technology for identifying and enhancing the complex faults which are responsible for the generation of natural fractures.

In addition, the multicomponent data were also analyzed for shear wave anisotropy information. Results show that shear wave anisotropy corresponds to areas of higher fracture density and is complementary to the fault interpretation.

This study shows the importance of characterizing the complex wrench fault system as these small displacement faults give rise to natural fractures. An understanding of the fracture zones has been achieved by a better fault model integrated with results obtained from multicomponent data, time-lapse data and production data. Such integrated fracture reservoir methodology is critical for better reservoir characterization.

TABLE OF CONTENTS

ABSTRACT	iii
LIST OF FIGURES	viii
LIST OF TABLES	xvi
ACKNOWLEDGEMENTS	xvii
CHAPTER 1 INTRODUCTION	1
1.1 Motivation for Present Work.....	1
1.2 Research Objective	5
1.3 Rulison Field Location and Geologic Overview	7
1.4 Background Research.....	11
1.5 Seismic Survey Acquisition	12
1.6 RCP Data Set vs. Seitel Data Set	22
1.7 Conclusions	22
CHAPTER 2 FAULT MECHANICS OF WRENCH FAULTS	23
2.1 Introduction	23
2.2 Wrench Fault Mechanics.....	23
2.3 Wrench Fault Models	27
2.4 Conclusions	32

CHAPTER 3 “ANT TRACKING” AUTOMATED 3-D FAULT

EXTRACTION TOOL.....	34
3.1 Introduction	34
3.2 Ant Tracking Workflow	35
3.2.1 Fault Enhancing Attributes	37
3.2.2 Ant Tracking Attribute.....	42
3.3 Synthetic Model.....	53
3.4 Applications to Rulison Data	56
3.5 Conclusions	59

CHAPTER 4 INTERPRETATION OF WRENCH FAULTS AT

RULISON	60
4.1 Introduction	60
4.2 Basin Stress History	60
4.3 Regional Fault Network	63
4.4 Wrench Fault Interpretation in Rulison Field	66
4.4.1 Fault Splaying in Rulison Field.....	77
4.4.2 Fault Block Rotation and Predicted Fracture Zones	81
4.5. Correlation of Faults and EUR.....	90
4.6 Conclusions	93

CHAPTER 5 SHEAR SPLITTING PARAMETERS AT RULISON ..	95
5.1 Introduction	95
5.2 Shear Wave Anisotropy Properties	95
5.3 Shear Wave Splitting Parameters at Rulison	99
5.3.1 Time Splitting Analysis at Rulison	102
5.3.2 Amplitude Analysis at Rulison	105
5.4 Conclusions	113
CHAPTER 6 CONCLUSIONS AND RECOMMENDATIONS.....	114
6.1 Conclusions	114
6.2 Recommendations	115
REFERENCES.....	116

LIST OF FIGURES

Figure 1.1 Rulison Field annual production volumes for Wasatch Formation and Mesaverde Group reservoirs and annual well counts for the same reservoirs from 1969 to the end of 1998. (From Hemborg, 2000)	4
Figure 1.2 Location map of Rulison gas field in the Piceance Basin, Garfield County, Western Colorado, USA	8
Figure 1.3 Stratigraphic column of the Rulison Field area. The tight gas sand reservoirs are within the late Cretaceous aged Mesaverde Group. (Modified after Hintze, 1988).	9
Figure 1.4 Cross-plot of net pay vs. Estimated Ultimate Recovery (EUR) for Rulison Field and the surrounding Grand Valley and Parachute fields. (From Cumella and Ostby, 2003).....	10
Figure 1.5 Seismic acquisition grid of RCP's 4D 9C 2003 survey.....	13
Figure 1.6 P-wave fold for all offset, RCP 2003 survey	15
Figure 1.7 Useable shear wave fold with 4000 ft maximum offset, RCP 2003 survey	15
Figure 1.8 Regional Seitel survey covering 36 square miles of the central Piceance Basin, including RCP's study area at Rulison Field. (Modified after Seitel Data, 2002)	18
Figure 1.9 Fold distribution for the Seitel survey. The max fold for the survey is ~75 fold, but is normally 35-40 fold (based on the following offsets: 0-7600' X-line, 0-13,200' In-line). (Provided by Ostby, 2005).....	19

Figure 2.1 Schematic illustrating right-lateral strike-slip movement in map view. The scale of the structural features can vary from centimeters to hundreds of kilometers. (From Sylvester, 1984).....	25
Figure 2.2 Schematic illustrating the diverging characteristics of an idealized wrench fault. The splays are referred to as palm tree structures and dominate the reservoir interval at Rulison Field. (From Christe-Blick and Biddle, 1985)	26
Figure 2.3 Laboratory measurements simulating wrench fault tectonics after 10 cm strike-slip displacement. Faults are numbered to permit correlation between plan view diagram and the vertical sections. See text for discussion. (Results and image from McClay, 2001).....	29
Figure 2.4 Small scale block rotation at Kilve, Somerset, UK. Similar fault block rotation, at a much larger scale, occurs in the reservoir interval at Rulison Field. (From Kim et al., 2004).	32
Figure 3.1 Schematic illustrating the ant tracking workflow. A chaos (coherency) cube (b) is generated from seismic cube (a). Conditioning by ant tracking is applied and the faults are enhanced in the ant tracker cube (c). The fault surfaces are extracted and displayed as 3-D fault patches (d). (From Pedersen, 2002).....	36
Figure 3.2 Arrows indicate the calculated gradient vector for each point along a reflection layer. (From Randen et al., 2000).....	38
Figure 3.3 Schematic illustrating three scenarios which are distinguishable by studying the eigenvalues resulting from the principal component analysis λ_{\max} , λ_{mid} , λ_{\min} . A dominating gradient is observed along the smooth reflector in (a) and the data is considered to be continuous ($\lambda_{\max} \gg \lambda_{\text{mid}} \approx \lambda_{\min}$). Scenario (b) and (c) are considered discontinuous because the bent reflector in (b) will have two strong directions ($\lambda_{\max} \approx \lambda_{\text{mid}} \gg \lambda_{\min}$) and the damaged zone in (c) will have gradients pointing in all directions ($\lambda_{\max} \approx \lambda_{\text{mid}} \approx \lambda_{\min}$). (From Pedersen, 2002)	40

Figure 3.4 Schematic illustrating the principle of swarm intelligence, which the ant tracker algorithm is based on. Two ants start out searching for food. The ant choosing the shortest path will travel back and forth more times, thereby marking the trail with more pheromone. The next ant, which is drawn to the pheromone, is more likely to choose the shorter path. (From Pedersen, 2002)	44
Figure 3.5 a) Fault cutting through seismic section. b) Chaos cube enhancing discontinuities caused by the fault. c) Grid illustrating the magnitude of discontinuity at each voxel surrounding the fault. d) Resulting ant track cube. e) Grid illustrates how the ant tracker has only extracted and connected the peak discontinuities associated with the fault	46
Figure 3.6 Line 2050 through a synthetic seismic cube showing five clear faults	54
Figure 3.7 Line 2050 through a chaos attribute created from the synthetic cube shown in the previous figure. Shaded areas correspond to areas of faulting	54
Figure 3.8 Line 2050 through an ant track cube created from the chaos cube shown in the previous figure. The ant tracker has performed a “thinning” operation by extracting the peak discontinuities. The resulting five faults are displayed as black/gray lines.....	55
Figure 3.9 All synthetic fault patches extracted from the ant track cube. Seismic line 2050 is intersected by five faults. Color bar indicates amount of throw on the fault patches (ms).....	55
Figure 3.10 Map view of three time slices at 1200 ms (lower reservoir), illustrating the value of the ant tracker. RCP study area outlined by black square. a) Seitel P-wave volume, b) chaos cube and c) the resulting ant tracking cube. The ant tracker scale represents how many times a feature has been tracked and is a measure of confidence	57

Figure 3.11 Cross section (A-A') intersecting fault detected by ant tracker in southwest corner at RCP's study area in Rulison Field. Fault path traced by ant tracker in green has been slightly edited by author. Dotted line represents time slice at 1200 ms as seen in Figure 3.10 ..58

Figure 4.1 Seismic crossline of Seitel data through Rulison and Parachute Fields illustrating regional fault tectonics in the central Piceance Basin. RCP study area outlined by dotted lines. Interpretation is that of Steve P. Cumella and Douglas B. Ostby (2003). (From Cumella and Ostby, 2003) 65

Figure 4.2 Time slice of entire Seitel survey at 1300 ms TWT from computed ant track attribute (through Cameo Coal Zone). Blue lines indicate fault architecture at this depth. Faults trend predominantly in a northwest direction with a few northeast stepovers present. RCP survey area is outlined by black square. Red line A-A' indicates cross section shown in Figure 4.3..... 68

Figure 4.3 Cross section A-A' (Figure 4.2) illustrating fault system interpreted at Rulison. RCP survey area outlined by dotted lines. Vertical exaggeration 20x. Note the upward diverging wrench fault characteristics. See text for discussion. 69

Figure 4.4 Cross section (B-B') of the largest wrench fault observed at RCP's study area in Rulison Field. Green line is the fault traced by the ant tracker software. R1-R3 reflectors illustrate areas which are characteristic of a wrench fault. See text for discussion..... 72

Figure 4.5 Time slice at 922 ms TWT from computed ant track attribute (upper reservoir). Two potential channels identified given their high sinuous pattern and low vertical extent. The surrounding linear features are considered to be faults given their linear strike and larger vertical extent. Red line indicates cross-section A-A' shown in Figure 4.3 73

Figure 4.6 RCP study area. Time structure map of the Cameo horizon using P-wave data from RCP’s 2003 survey. Black lines represent the largest most continuous faults observed on the Seitel data. Faults parallel structural contours at this depth and will diverge into smaller fault fragments in the main reservoir interval..... 75

Figure 4.7 RCP study area. Structure map of the Cameo horizon using well top data provided by Williams Production Company. Dots indicate well top data used. Black lines are the largest, most continuous faults observed below the main reservoir using the ant tracker attribute. Faults parallel structural contours at this depth and will diverge into smaller fault segments in the main reservoir..... 76

Figure 4.8 Time slices of ant tracking attribute (a-d). RCP study area outlined by black square. Blue lines represents fault geometry and become more complex in and above the main reservoir interval. Circles illustrate fault block corner areas which are more likely to fracture due to increased stress variations..... 80

Figure 4.9 Time slice at 1130 ms TWT from computed ant track attribute (mid-lower reservoir). Blue lines represents wrench fault pattern and arrows indicate slip movement. Fault block corners E and E’ experience extension and is more likely to fracture due to increased stress variations as fault segments X-Z and Y-Z diverge 83

Figure 4.10 Time slice at 1130 ms TWT from computed ant track attribute. Dotted line illustrate seismic cross section through fault block corner shown in Figure 4.11 84

Figure 4.11 Seismic cross section C-C’ through fault block corner. Fault block has been enhanced and is bounded by Z. Right side of the fault block has been downthrown and correspond to the extensional quadrant E, seen in Figure 4.9. Dotted line represents time slice at 1300 ms seen in Figure 4.9. Vertical exaggeration 10x..... 85

Figure 4.12 a) Preliminary time lapse anomaly between 1996 DOE survey and 2003 RCP survey at 1080 ms RCP time (Approximately 1110 ms Seitel time) (Courtesy Mahendra Kusuma, 2005). Yellow dot represents best producing well in the field, Clough 19. b) Time slice at 1130 ms Seitel time from computed ant track attribute showing fault architecture at this depth. c) Overlay of fault geometry with time lapse anomaly show that drainage area (red) is within extensional quadrant highlighted by black circle 87

Figure 4.13 a) Preliminary time lapse anomaly between 1996 DOE survey and 2003 RCP survey at 980 ms RCP time. (Courtesy Mahendra Kusuma, 2005). b) Time slice of computed ant track attribute through center of time-lapse anomaly. c) Black circles illustrate areas where time lapse anomalies correspond to fault corners experiencing enhanced natural fracture density..... 88

Figure 4.14 The highlighted north and northeast fault are sealing faults, bounding the time lapse anomaly in the southeast corner 90

Figure 4.15 Estimated Ultimate Recovery (EUR) map for all the wells in the RCP study area. Note that best producing wells trend in a northwest direction, suggesting a link to the structural trends below the reservoir..... 92

Figure 4.16 Better EUR wells are associated with fault block corner areas and corresponding time lapse anomalies. EUR values decrease away from fault block corner areas 93

Figure 5.1 Schematic illustrating shear wave propagation and splitting in a unidirectional fractured medium. When encountering the fractures the incident shear wave will split into two waves with polarization of the faster (S_{\parallel}) wave parallel to the fracture planes and the slow (S_{\perp}) wave will propagate perpendicular to the fracture planes. (From Martin and Davis, 1987) 97

Figure 5.2 Yellow line represents inline 70 across RCP survey area. Comparison of seismic sections (S1 and S2) across inline 70 are shown in Figure 5.3 100

Figure 5.3 Amplitude and time splitting between S1 (a) and S2 (b) data sets along inline 70 are indicative of anisotropy. Shear wave splitting parameters between the two lines can be linked to areas of enhanced natural fracturing. Black rectangle outlines area of particularly high amplitude variations. A larger time lag is observed in the S2 volume below the black rectangle on the Cameo horizon, also indicative of anisotropy 101

Figure 5.4 Time splitting analysis (average anisotropy) calculated between Price Coal and Cameo horizon. Anisotropy ranges from 0-8% in high fold areas. High anisotropy observed in the southwest corner and along the survey boundaries are caused by edge effects in the S2 volume 104

Figure 5.5 Time splitting (average anisotropy) analysis between Price Coal and R2 horizon. Similar anisotropy anomalies, but with less magnitude observed at this interval compared to the Price Coal-Cameo interval in Figure 5.4..... 104

Figure 5.6 Shear wave splitting parameter map calculated from S1-S2 amplitudes at a 50 ms window hung from the Cameo horizon (lower reservoir). Note predominantly low anisotropy at this level caused by small orthogonal fracture sets, creating an “isotropic medium” in the coal layers..... 108

Figure 5.7 Shear wave splitting parameter map calculated from S1-S2 amplitudes at 50-100 ms below the Price Coal horizon (top of reservoir). Note numerous high amplitude variations indicative of directional fracturing..... 108

Figure 5.8 a) Time slice of ant tracking cube at 1130 ms reflecting fault pattern observed at this level. b) Shear wave splitting parameter calculated from amplitude differences between S1 and S2 over the fault pattern (50ms window). Note how the northeast stepover fault correspond to northeast anisotropy anomaly, illustrating a correspondence between fault interpretation and shear anisotropy 111

Figure 5.9 Overlay of fault pattern with amplitude variations from previous figure. Northeast stepovers correlate with negative amplitude anomaly indicating a predominant northeast fracture direction. Yellow dot represents best producing well in the field, Clough 19. Note the large negative anomaly associated with the fault block corner, where Clough 19 is located, indicating enhanced natural fracturing 112

LIST OF TABLES

Table 1.1 RCP Phase X seismic acquisition parameters	14
Table 1.2 P-wave processing flow, RCP survey	16
Table 1.3 S-wave processing flow, RCP survey	17
Table 1.4 Seitel acquisition parameters.....	20
Table 1.5 Seitel generalized processing sequence.....	21
Table 3.1 Ant tracking parameters	49-50
Table 3.2 Surface parameters	51-52

ACKNOWLEDGEMENTS

The completion of this thesis is the result of support from many people. I would like to thank my advisor, Dr. Tom Davis for his guidance and support throughout my graduate time as well as on this project. Working with him and the Reservoir Characterization Project has been a great honor for me and I appreciate his continuous support. I also thank my thesis committee members for their guidance: Mike Batzle, Bob Benson, Jennifer Miskimins and Max Peeters. I would also like to extend thanks to all RCP students for their advice and good friendship.

I would also like to acknowledge Lars Sonneland, Michael Nickel and their research group at Schlumberger Stavanger Research for teaching me some of their newest seismic developments applied in this thesis. To this I should add the sponsors of RCP for their financial support and interaction. I would also like to thank Schlumberger Denver, and in particular, Dr. Yuan Ma for helping me navigate through new software.

Special thanks go to all my friends here at School of Mines. These people have made my stay here in Golden enjoyable and memorable. While space prevents naming them all I would like to single out Shannon Higgins, Ivan Vasconcelos, Eugenia Rojas, Mark Vrijlandt, Matt Reynolds, Jyoti Behura, Rodrigo Fuck, Lauri Burke, Neil Dannemiller, Tamara Gipprich, Carlos Pacheco, Justin Modroo and Firuz Salamov.

I would also like to acknowledge my very good friends, colleagues and roommates Kasper Van Wijk and Ludmila Adam for the good times around the house. Finally, I would like to thank my family for their continuous support and encouragement.

CHAPTER 1

INTRODUCTION

1.1 Motivation for The Present Work

Unconventional gas resources have become a major source of US supply over the last 20 years and will be even more important in the future (Fletcher, 2005). The Rocky Mountain region contains the largest unconventional gas resource in the U.S. and production is to increase by 50% in 2020 (Fletcher, 2005). Unconventional gas, such as tight gas sand reservoirs at Rulison, are difficult to produce due to very low matrix permeabilities ($< 1\text{mD}$). Hence, in order to meet the expected 50% gas production increase by the year 2020, more sophisticated methods for improving gas recovery from tight gas sands are needed. The Reservoir Characterization Project (RCP) is developing improvements in 3 and 4D seismic using multicomponent data to better characterize tight gas sand reservoirs. The overall goal is increasing the production potential in tight gas sands at Rulison Field, Colorado.

Kuuskraa et al. (1997) made a gas-in-place estimate for the Piceance Basin's Williams Fork Formation based on: a recent stratigraphic study of the southern Piceance Basin (Lorenz, 1990), advanced well-log analysis of 12 key wells, and reservoir data from field operators. He concluded that 311 trillion cubic feet (Tcf) of gas exists in place in the Williams Fork reservoirs in the Piceance Basin. He also concluded that the four fields in the South

Central portion of the basin, Rulison, Grand Valley, Mamm Creek, and Parachute, contain 106 Tcf of this total 311 Tcf gas resource. Hence, Rulison Field contains one of the richest concentrations of gas in place in the U.S. The problem is unlocking the gas.

Despite the rich concentration of gas in place, only a small percentage has been produced. From the 1950s to the late 1980's a considerable amount of money and staff resources were invested in the Piceance Basin in attempts to exploit the gas-saturated tight gas sands (Hemborg, 2000). In conjunction with private sector enterprises, branches of the United States Government (Atomic Energy Commission and Department of Energy), in consort with the Gas Resource Institute (GRI), funded programs directed towards increasing deliverability and ultimate recovery from the Williams Fork Formation tight gas sands (Hemborg, 2000). A part of their extensive research to enhance permeability even included the detonation of nuclear devices in 1969 and 1973 in two separate bore holes for Williams Fork Formation fracture stimulation. Unsuccessful nuclear fracs of the Austral 25-95 Hayward (Sec. 25, T7S, R95W) and the Rio Blanco #1 (Sec. 14, T3S, R98W) occurred. Both wells were located outside the RCP study area. According to Hemborg (2000) the various attempts to exploit the large in-place Williams Fork Formation gas resources in the Piceance Basin can best be characterized as disappointing until now.

The U.S. Department of Energy has been heavily involved with the Piceance Basin tight-gas sand research efforts since 1977 (Hemborg, 2000).

In 1981, DOE began a \$40 million comprehensive study of the Multi-well Experiment (MWX) site located in the Rulison gas field, west of Rifle, Colorado. The experiment was designed to characterize low-permeability natural-gas reservoirs for the purpose of effective stimulation and production (Myal and Frohne, 1991). The reservoir interval of the Mesaverde Group rocks was studied in detail.

The various research efforts began to pay off in the 1990's, particularly beginning in 1995. A graph of annual production volumes and well counts from the Rulison tight gas sand reservoirs from 1970 through 1998 is shown in Figure 1.1. A significant growth in production can be observed in the last few years. Average annual gas production per well during 1980 through 1989 was 32 million cubic feet (MMcft), and the averaged climbed to 84 MMcft from 1995 to 1999 (Hemborg, 2000). According to Kuuskraa et al. (1997), the key factor responsible for the growth in production is detection of naturally fractured "sweet spots". Other key factors include improved well log analysis, completion and stimulation procedures, infill development programs, and recompletion of older wells. Hydraulic fracturing links the already existing natural fractures thereby increasing the gas flow, and recent developments using this technique has also been considered a key contributor to the increased gas production at Rulison.

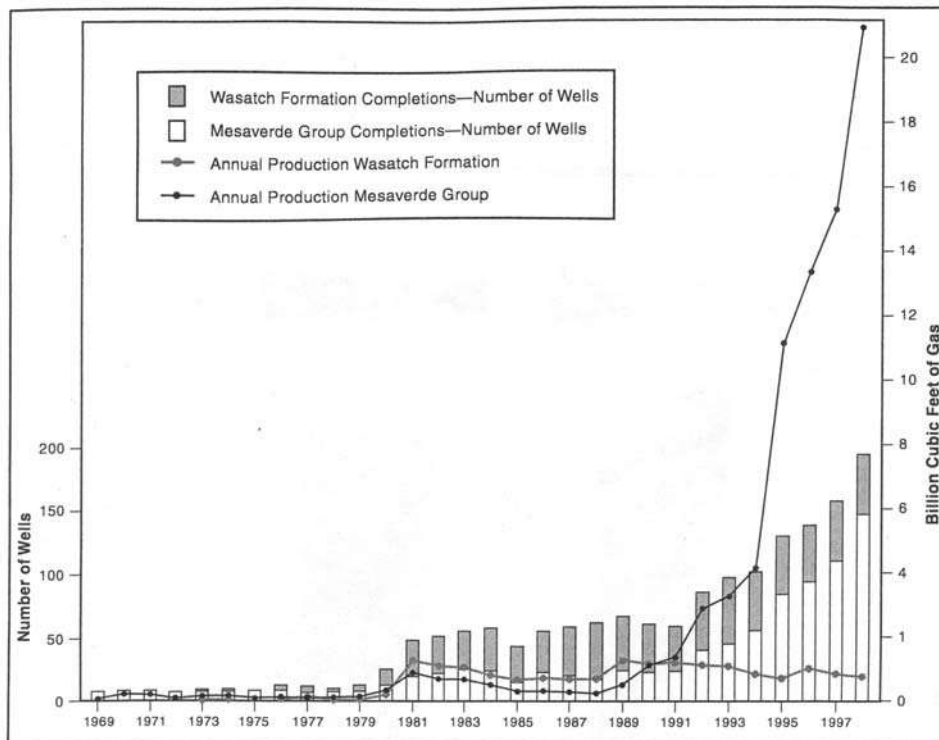


Figure 1.1: Rulison Field annual production volumes for Wasatch Formation and Mesaverde Group reservoirs and annual well counts for the same reservoirs from 1969 to the end of 1998. (From Hemborg, 2000)

Given the extremely low permeability (5-30 μD) observed in Piceance Basin Mesaverde gas reservoirs (Lorenz and Finley 1991), commercial production primarily occurs where natural fractures are present (Hoak and Klawitter, 1997). Data collected by DOE researchers at the MWX site confirm that a production increase of over two orders of magnitude occurs when natural fractures are present (Lorenz and Finley, 1991). Considerable evidence indicates that natural fractures are the primary conduits for gas movement in the Piceance Basin and that these fractures play a significant role in Mesaverde Group gas production. “Establishing

the regional presence and specific location of such natural fractures is the highest priority exploration goal in the Piceance and other western U.S. tight, gas-centered basins” (Kuuskraa et al., 1997).

1.2 Research Objective

The ability to predict the presence of faults and fractures in tight gas sands will allow the reservoir engineer to target the “sweet spots” thereby increasing well performance. The natural fractures are strongly linked to subsurface structures. It is essential to understand the subtle yet complex fault network observed at Rulison to better predict areas of enhanced natural fracturing. My research has therefore focused on further investigating the fault observations made initially by Hoak and Klawitter (1997), Kuuskraa et al. (1997), and by Ostby and Cumella (2003). By utilizing a newly developed 3-D automatic fault mapping tool, in conjunction with attribute mapping from the multicomponent seismic survey, I introduce a new fault model which can be used to predict areas of enhanced fracturing.

Multicomponent data can also help identify natural fractured zones. Seismic anisotropy, particularly shear wave anisotropy, responds to the presence of fractures in the subsurface. S-wave splitting parameters, such as amplitude and time splitting analysis, from the multicomponent data has been incorporated into this thesis to delineate natural fractures in the reservoir.

In order to best predict the areas of enhanced natural fracturing we need to integrate our fault model with results obtained from the multicomponent data, time-lapse data and production data. Such an integrated fractured reservoir detection methodology is critical to minimize the subjectivity and ambiguity that occurs when only a single data set for interpretation is used.

The objective of this research is to create a fault model which predicts areas of enhanced fracturing, and to utilize multicomponent data to interpret areas of higher fracture density. The specific details of this research are to:

- Use an automatic fault extraction tool to better characterize the complex fault pattern observed at Rulison.
- Develop a fault model to better predict areas of higher fracture density.
- Use multicomponent data to further detect, analyze and quantify the natural fractures within the reservoir.

1.3 Rulison Field Location and Geological Overview

The Piceance Basin of Colorado is a northwest-southeast trending structural basin that formed during the Late Cretaceous through Eocene “Laramide” Orogeny (Hoak and Klawitter, 1997). Rulison Field is located in the south central portion of Piceance Basin in Garfield County, Colorado (Figure 1.2). The field is basin-centered, with a continuous gas accumulation, and there is no water leg in the reservoir. Gas production is primarily from the nonmarine Late Cretaceous Williams Fork Formation, Mesaverde Group, at total depths ranging from 6000 to 9000 ft. (Cumella and Ostby, 2003). A stratigraphic column of Rulison Field is shown in Figure 1.3. Strata of the Iles and Williams Fork represent depositional environments that changed from strandline and deltaic to coastal plain to fluvial and floodplain to alluvial plain from the base to the top of the sequence (Kuuskraa et al., 1997). The Williams Fork Formation has different proportions of sandstone and mudrock. The lower 500 to 700 ft of the Williams Fork is dominated by mudrock with numerous, isolated lenticular fluvial sand bodies (i.e., a low “net-to-gross” interval), whereas the upper Williams Fork is characterized by less mudrock and thicker, more laterally continuous sand bodies (i.e., a high “net-to-gross” interval) (Pranter, 2003). The pay section consists of 1700–2400 ft intervals of stacked, highly discontinuous fluvial sandstones, which is the result of deposition as point bars by meandering streams. The sand bodies are normally pressured to slightly over-pressured. Subsurface and outcrop

studies suggest that the stacked point bar reservoirs range from 20 to 60 ft, with a lateral extent of 500-1500 ft. (Kuuskraa et al., 1997). The tight gas reservoir at Rulison has extremely low permeabilities (5-30 microdarcies) and is observed in all Piceance Basin Cretaceous-age gas reservoirs (Reinecke et al., 1991; Lorenz et al., 1991). The presence of authigenic clays, carbonate cement and quartz overgrowth is the reason why the sands have low porosities of 6 to 12% (Kuuskraa et al., 1997).

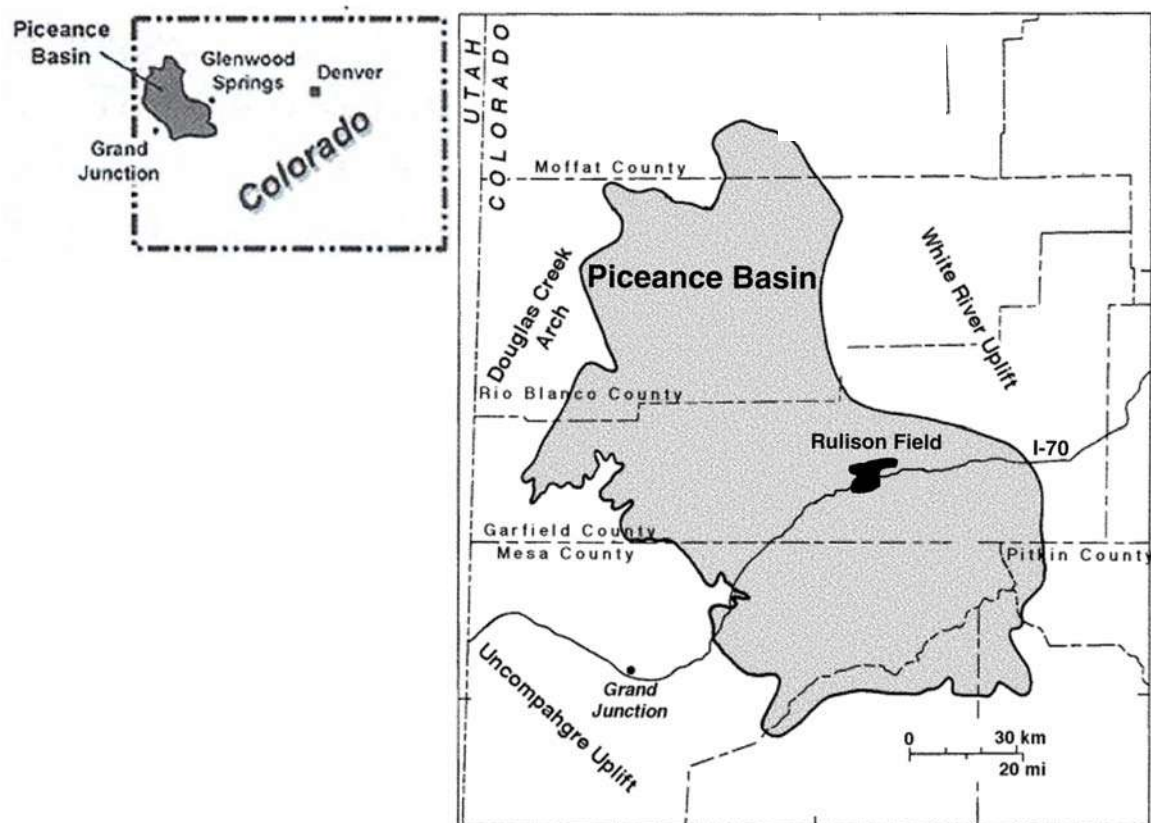


Figure 1.2: Location map of Rulison gas field in the Piceance Basin, Garfield County, Western Colorado, USA.

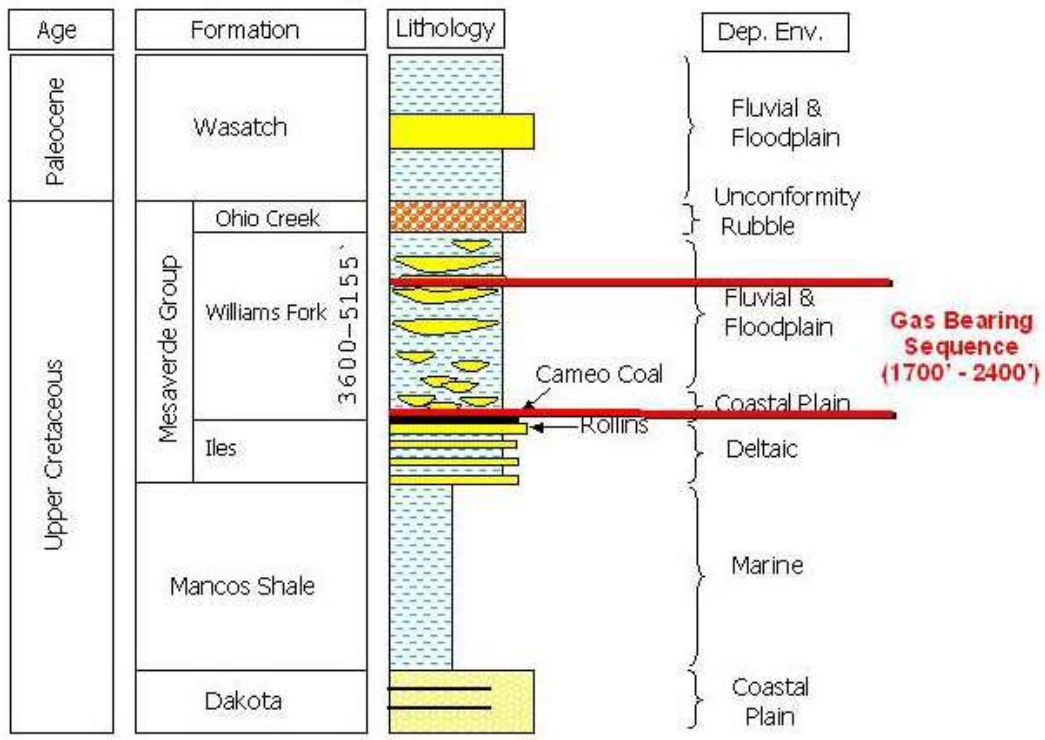


Figure 1.3: Stratigraphic column of the Rulison Field area. The tight gas sand reservoirs are within the Late Cretaceous Mesaverde Group. (Modified after Hintze, 1988).

Rulison Field is not a conventional reservoir. There is no correlation between net sand thickness and well productivity. The scattered trend observed in Figure 1.4 suggests that net sand thickness is not the primary control on gas production. Instead, the presence of natural fractures is the dominating control on wellbore deliverability and therefore economic production according to (Hoak and Klawitter, 1997; Kuuskraa et al., 1997; Lorenz and Finley, 1991). Rulison field is therefore considered a fractured reservoir because its productivity and performance are strongly affected by the presence or absence of faults and fractures.

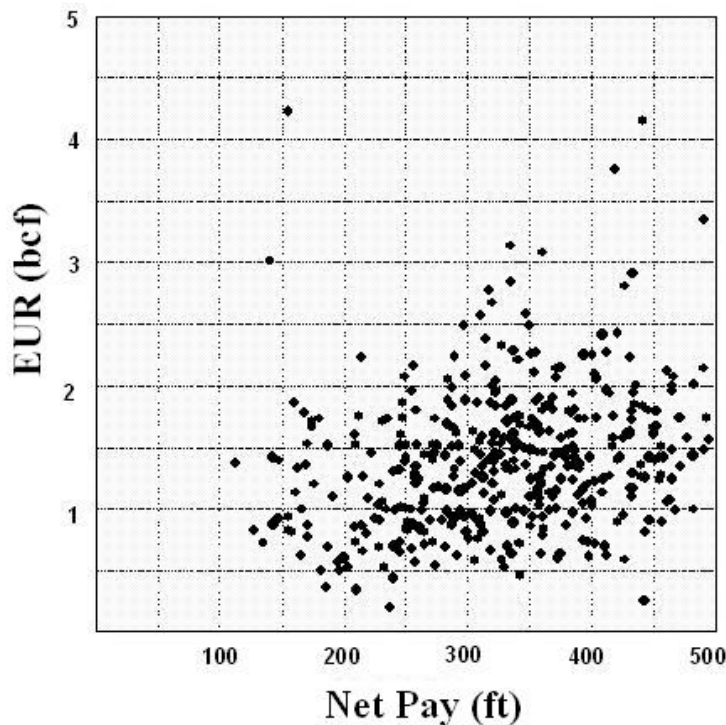


Figure 1.4: Cross plot of net pay vs. Estimated Ultimate Recovery (EUR) for Rulison Field and the surrounding Grand Valley and Parachute fields. (From Cumella and Ostby, 2003)

1.4 Background Research

A review of the structural and tectonic evolution of the Piceance Basin indicates that basement controlled faulting, resulting from tectonics during Precambrian, Pennsylvanian and Late Cretaceous/Early Tertiary time, has influenced the development of the major fault systems in the basin (Kuuskraa et al., 1997). Hence, the natural fractures are linked to subsurface structures. The close relationship between basement structures and fracture-controlled production trends has led Kuuskraa (1997) and Hoak and Klawitter (1997) to characterize basement deformation and fracture reservoir production. Kuuskraa et al. (1997) suggested that fault planes terminate within mid pay section, and splay into a wedge of fracture systems characterized by reflector offset, amplitude dimming and generally poor amplitude coherency. He observed that areas where faults splay into the reservoir are more likely to be naturally fractured thereby increasing the wellbore deliverability.

In addition, Hoak and Klawitter (1997) also observed that subsurface structures corresponded to areas of enhanced gas production at Divide Creek, located 13 miles to the southeast of Rulison Field. His integrated research suggested that the Divide Creek Anticline had been broken into a series of fault blocks by both the northwest-trending thrusts, and also by northeast trending normal faults. The fault blocks have offset the reservoir continuity thereby compartmentalizing the Divide Creek reservoir interval.

1.5 Seismic Survey Acquisition

The RCP Phase X seismic survey was acquired by Solid State Geophysical during October 2003. It took place on Sharrad Park and is of rectangular configuration approximately 2.2 km by 2.5 km, for a total area of 5.5 square kilometers (Figure 1.5). An orthogonal acquisition geometry was used to make the survey layout more economical and promote good azimuthal distribution. The northern extent of the survey is dictated by steep slopes of the Roan Cliffs. As seen in Figure 1.5, topography in the northern part of the survey limited the layout of sources and receivers. The 2003 survey featured dry conditions, but some noise was introduced due to drilling operations, the railroad traffic and highway I-70 which bordered the survey grid to the south.

The RCP survey was designed primarily for shear wave acquisition. The survey parameters are listed in table 1.1. Designing the survey using the parameters listed in table 1.1 produced high fold data, which reduced noise in the stacking process. The small tight gas sand bodies require high vertical resolution data with low noise to make accurate estimates of anisotropy and improved reservoir characterization. The survey fold using 50'x 50' bin size is 225 at all offsets for the compressional data, and up to 65 at 4000 ft maximum offset for the shear wave data (Figure 1.6 and 1.7). The acquisition geometry promoted uniform azimuthal and uniform offset trace distribution to optimize anisotropy and amplitude analysis techniques.

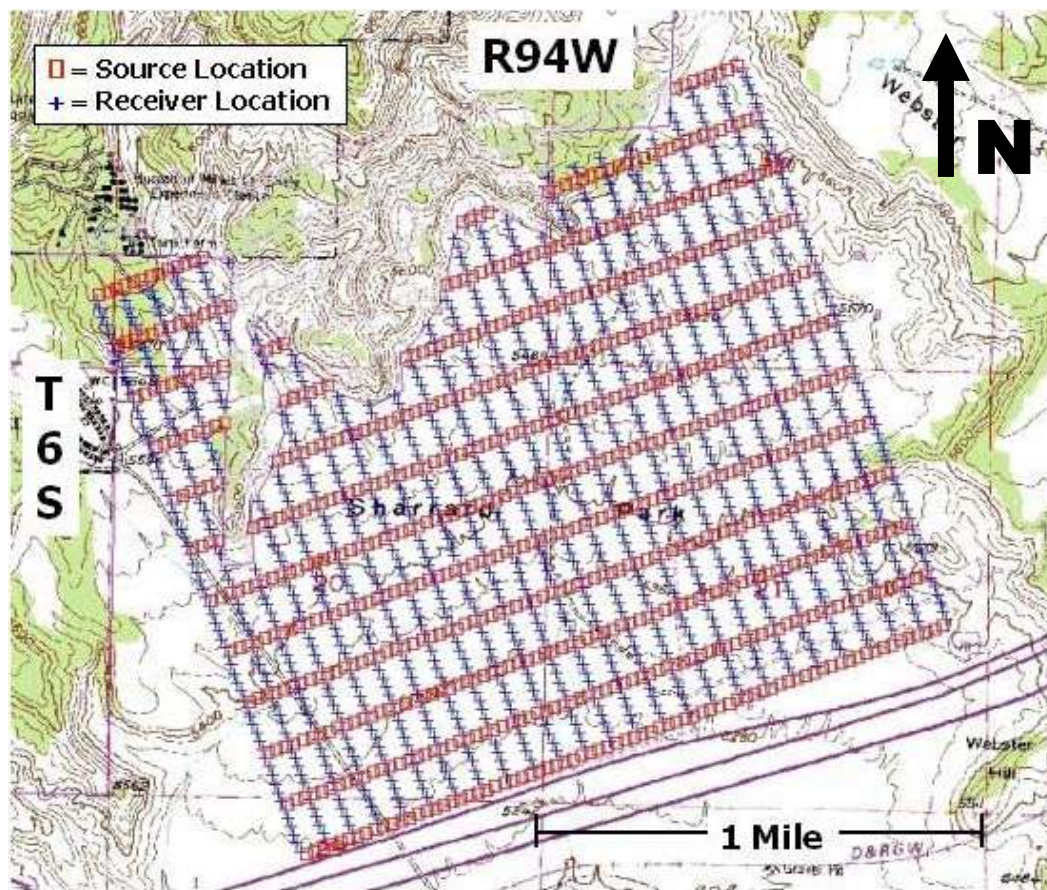


Figure 1.5: Seismic acquisition grid of RCP's 4D 9C 2003 survey.

Table 1.1: RCP Phase X seismic acquisition parameters

Type Survey	4-D, 9-C (time-lapse)
Subsurface bin size	55' X 55'
Number of receiver locations	1500
Number of source locations	770
Receiver grid	Stationary: 7260' X 8250'
Receiver grid	110' inline spacing, 330' between lines
Source grid	110' inline spacing, 660' between lines
Instrumentation	I/O VectorSeis [®] System Four [™] VR & VC
Receiver array	1, 3-C VectorSeis [®] SVSM [™] Sensor
Source array (P-wave)	Mertz 18
Source array (S-wave)	IVI TRI-AX / Mertz
S-wave sweep range	5-50 Hz
P-wave sweep range	6-120 Hz

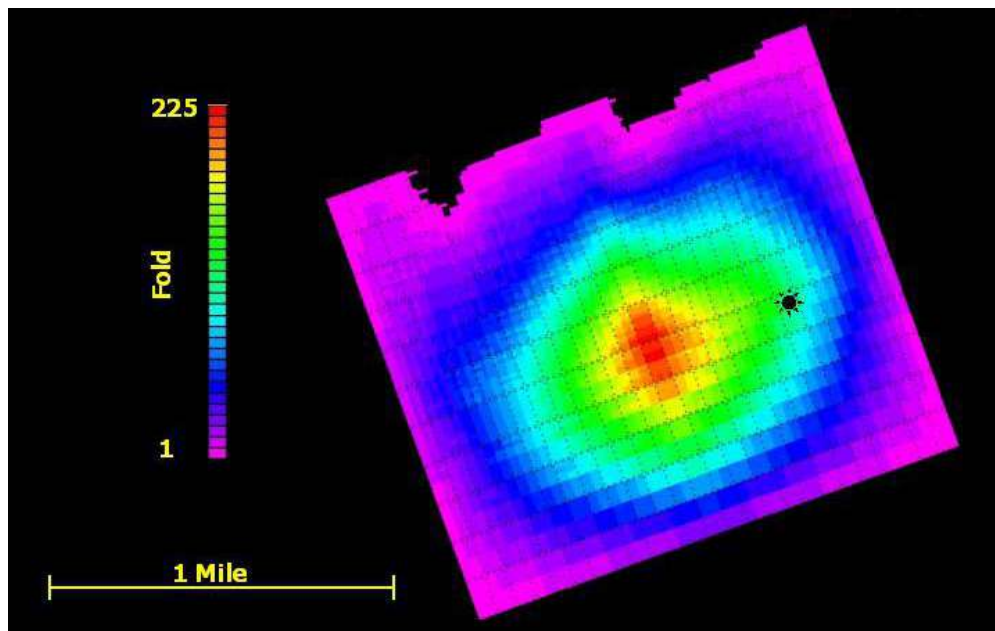


Figure 1.6: P-wave fold for all offset, RCP 2003 survey.

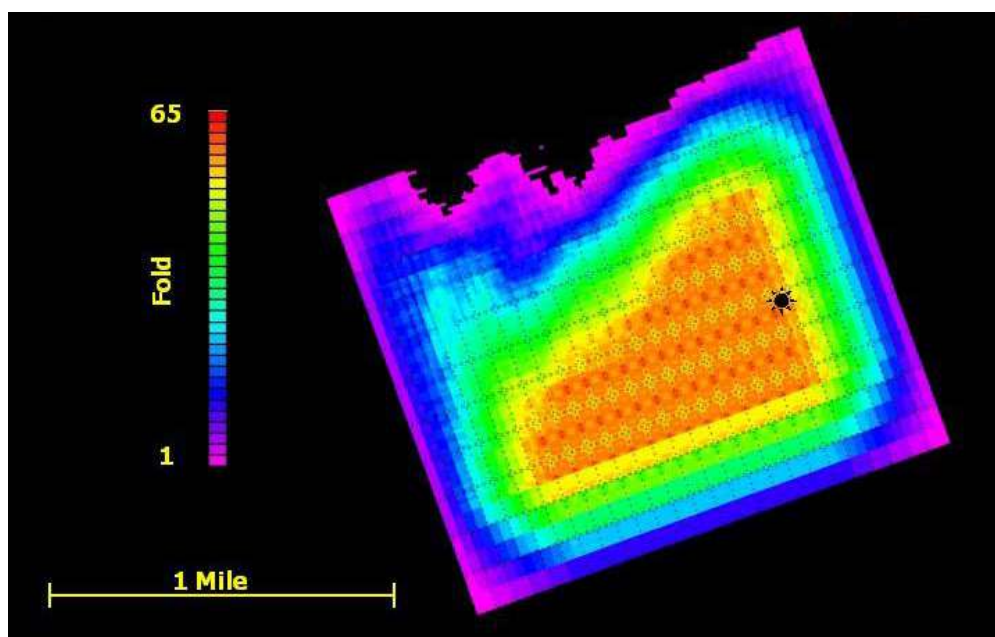


Figure 1.7: Useable shear wave fold with 4000 ft maximum offset, RCP 2003 survey.

The processing of the RCP seismic data was performed by Veritas, DGC in Calgary. The processing flow of the 2003 P and S wave data is outlined in table 1.2 and 1.3.

Table 1.2: P-wave processing flow, RCP survey

• Tilt correction for Vectorseis phone applied in Field
• Demultiplex/Geometry/First Break Picks
• Refraction Tomography Statics
• Manual Trace Edits/Amplitude Recovery – T2
• Surface Consistent Amplitude Equalization
• Surface Consistent Deconvolution
• Velocity Analysis (Preliminary)
• Surface Consistent Statics (Preliminary)
• Velocity Analysis (Final)
• Surface Consistent Statics (Final)
• First Break Mutes
• Trim Statics
• Amplitude Equalization – Mean Scaling
• Stack
• Noise Attenuation (FXY Deconvolution)
• Migration – Kirchhoff
• Filter – 5/10-100/110hz 0-1600 ms, 5/10-80/95hz 1600-2800 ms
• Amplitude Equalization – Mean Scalining

Table 1.3: S-wave processing flow, RCP survey

• Tilt correction for Vectorseis phone applied in Field
• Demultiplex
• Geometry
• Manual Trace Edits
• Polarity Correction – Receiver and Shot
• Amplitude Recovery – T2
• Surface Consistent Amplitude Equalization
• Alford Rotation – N45W
• Surface Consistent Deconvolution
• Apply phase and static correction to Match Mertz with IVI
• Source/Receiver Statics – From P-S Data
• CDP Gather
• Velocity Analysis (Preliminary)
• Noise Attenuation – Radon Transform
• Surface Consistent Statics (Preliminary)
• Velocity Analysis
• Surface Consistent Statics
• First Break Mutes
• Trim Statics
• Re-iterate Noise Attenuation – Radon Transform (Apply all statics and velocities)
• Trim Statics
• Amplitude Equalization – Mean Scaling
• Stack
• Migration – Kirchhoff
• Filter – 4/8-30/40 Hz 0-3000 ms, 4/8-25/35 Hz 3000-6000 ms
• Amplitude Equalization – Mean Scaling

A regional 3-D seismic survey covering 36 square miles was provided to RCP by Seitel (Figure 1.8). The Seitel survey was shot in 2001 by Seitel Data with a 110 ft x 110 ft bin size and 35 fold at full offset range. The fold distribution for the Seitel survey can be seen in Figure 1.9. Structural interpretation was mostly carried out on the Seitel data. The seismic acquisition parameters, and processing flow is listed in table 1.4 and 1.5.

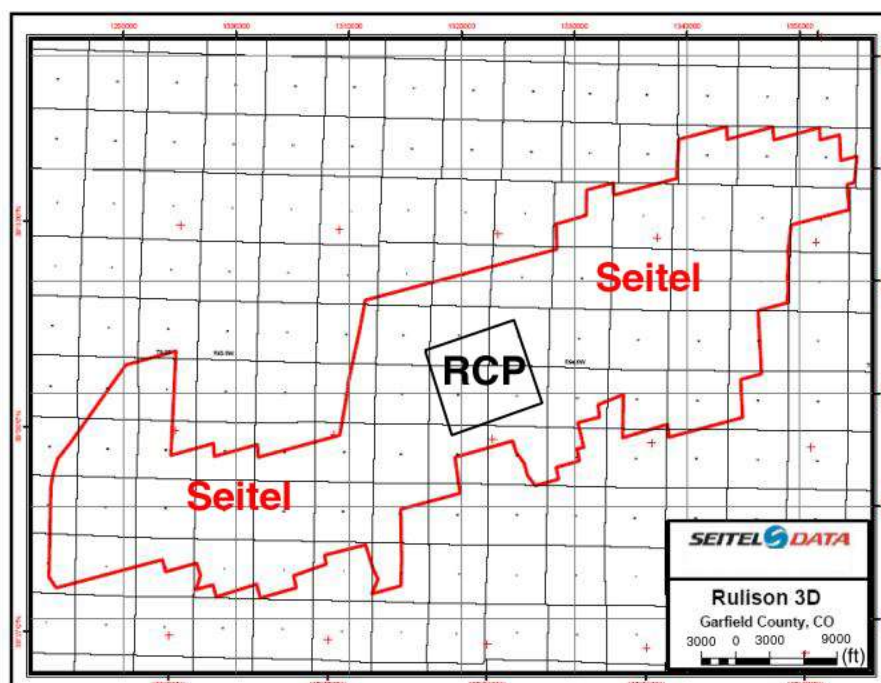


Figure 1.8: Regional Seitel survey covering 36 square miles of the central Piceance Basin, including RCP's study area at Rulison Field. (Modified after Seitel Data, 2002).

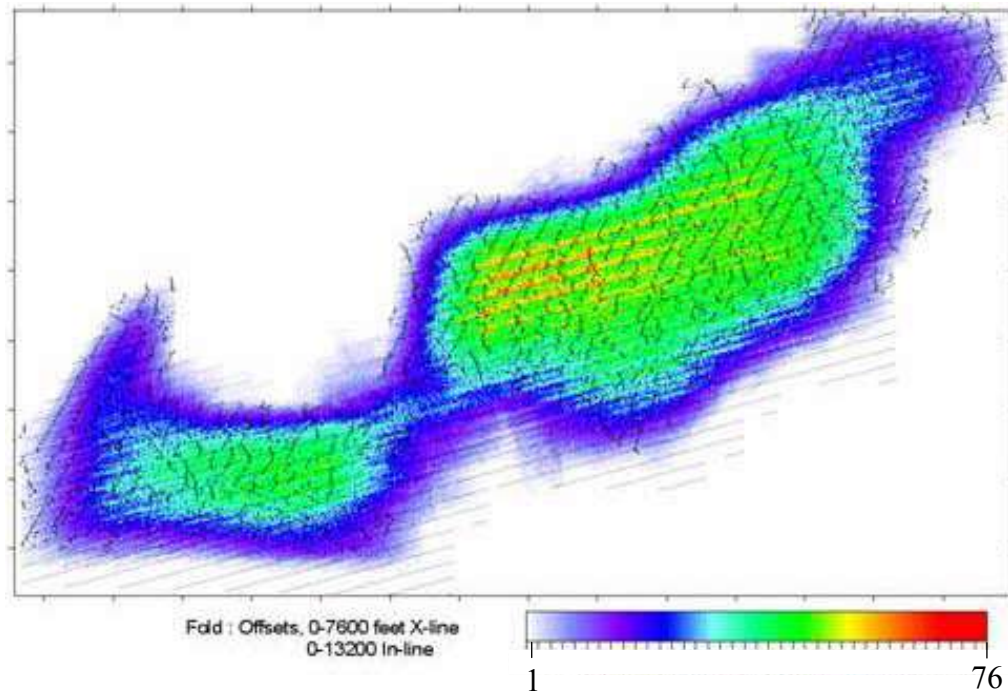


Figure 1.9: Fold distribution for the Seitel survey. The max fold for the survey is ~75 fold, but is normally 35-40 fold (based on the following offsets: 0-7600' X-line, 0-13,200' In-line). (Provided by Ostby, 2005).

Table 1.4: Seitel acquisition parameters

• Recording System	I/O System II
• Survey Size	36.00 Square Miles
• Acquired	September 2001
• Sample Rate	2 Milliseconds
• Record Length	5 Seconds
• Source I	11 lbs. Pentolite @ 60 ft.
• Source II	4 50,000 lb. peak force vibratrs.
• Sweep	8 8-seconds sweeps per v.p.
• Receiver Array	6 Phones (15' diameter circle)
• Bin Size	110 x 110 feet
• Designed Fold @ full offset range	35
• Receiver Line Orientation	NE-SW
• Survey Method	GPS and conventional
• No channels	1,120
• Spread	14 lines x 80 channels
• Patch	14,300 feet x 17,380 feet
• Group interval	220 feet
• Shot interval	220 feet (5 shots per salvo)
• Receiver Line Interval	1,100 feet
• Shot Line interval	1,760 feet (45 degree diagonal)

(Seitel Data, 2002).

Table 1.5: Seitel generalized processing sequence

• Reformat	
• Geometry Definition and Application	
• Q.C. Surveying/Positioning Data	
• Display Field Records and Edit	
• 3D Refraction Statics	
• Spherical Divergence and Gain Correction	
• Deconvolution	
• Binning of Data into 110' x 110' bins	
• Regional Velocity Analysis	
• Initial Stacks	
• Structural Velocity Analysis	
• 3-D NMO Correction and Stack	
• 3-D Surface Consistent Residual Statics	
• Velocity Refinement	
• Second Iteration of 3-D Surface Consistent Residual Statics	
• Receiver Line Interval	1,100 feet
• Shot Line interval	1,760 feet (45 degree diagonal)

(Seitel Data, 2002)

1.6 RCP Data Set vs. Seitel Data Set

The Seitel and RCP surveys vary in size, survey acquisition and processing flow. Hence, they each serve a different purpose. The RCP survey was processed for time-lapse analysis enabling accurate differencing and not necessarily structural imaging. The high fold RCP data was shot for multicomponent analysis. The Seitel data provided more regional structural imaging. The two data sets are complementary as the majority of fault interpretation was carried out on the Seitel survey and the high fold RCP survey was used for multicomponent and time-lapse analysis.

1.7 Conclusions

Rulison is considered an unconventional gas reservoir due to the extremely low permeabilities which dominate the tight gas sand reservoirs in the field. Considerable evidence indicates that natural fractures are the primary conduits for gas movement in the Piceance Basin, and that these fractures dominate the production from the Measaverde tight gas sands. The natural fractures are strongly linked to the faults. The goal of this thesis is therefore to understand the faults and to predict areas of enhanced fracturing. Multicomponent data were used to verify areas of higher fracture density.

CHAPTER 2

FAULT MECHANICS OF WRENCH FAULTS

2.1 Introduction

Interpretation and analysis of complex 3-D structures in the subsurface is one of the major challenges in hydrocarbon exploration (McClay, 2001). More specifically, wrench faults, synonymous with strike-slip fault systems, have received considerable attention in recent years. The uncertainty in interpretation of wrench fault systems can be linked to the mechanism of strike-slip movement which produce numerous faults of diverse nature, orientation and scale (Asgarov, 2004). Recognition of wrench-faulting is difficult and complicated, but it is also essential to better characterize and predict areas of enhanced natural fracturing at Rulison Field. In order to gain an understanding of wrench fault systems and set a rational framework for their identification and interpretation a description of wrench fault mechanics and associated wrench fault models follow in this chapter.

2.2 Wrench Fault Mechanics

Strike-slip faults form in response to horizontal shear movement within the subsurface caused by either compression or extension. Strike-slip deformation typically occurs where one crustal block moves laterally with respect to an adjacent block and the resulting strike-slip faults are

characterized by linear or curvilinear principal displacement zone in plan view (Christie-Blick and Biddle, 1985) (Figure 2.1). Other fundamental features such as oversteps, branching and braiding are associated with strike-slip fault zones and fault systems. As a result, strike-slip faults have a narrow sub-vertical displacement zone at depth, but diverge upward into the sedimentary cover (Figure 2.2). Faults with such geometry are commonly termed wrench faults, and the arrays of upward-diverging fault splays are known as “palm tree structures” (Terminology from: A. G. Sylvester and R. R. Smith, Sylvester, 1984) or “flower structures” attributed to R. F. Gregory by Harding and Lowell, 1979, (Christie-Blick and Biddle, 1985). The branching of the faults is caused by the redistribution of stresses in the process of tectonic faulting. According to Mandl (1988), relatively small changes in the horizontal principal stresses are required for the principal stress direction to switch, allowing conjugate wrench faults to develop. The branching palm tree structures combine with each other to produce complicated fracture patterns. These structures have been interpreted because they are strongly linked to the occurrence of natural fractures at Rulison Field.

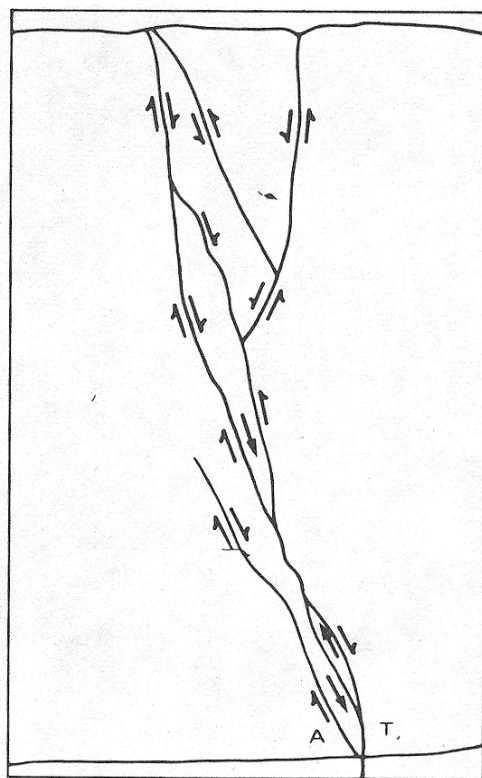


Figure 2.1: Schematic illustrating right-lateral strike-slip movement in map view. The scale of the structural features can vary from centimeters to hundreds of kilometers. (From Sylvester, 1984).

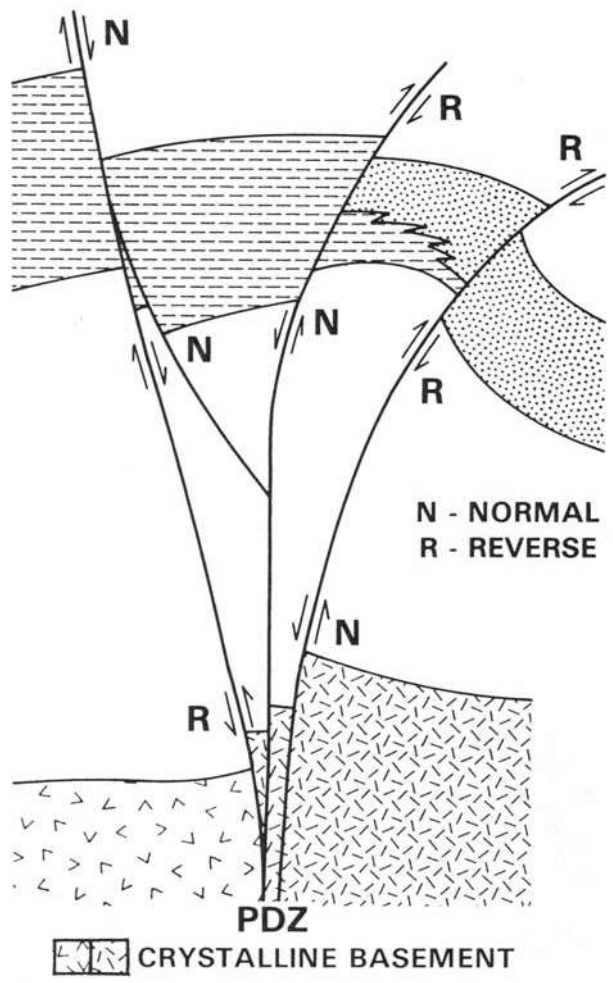


Figure 2.2: Schematic illustrating the diverging characteristics of an idealized wrench fault. The splays are referred to as palm tree structures and dominate the reservoir interval at Rulison Field. (From Christie-Blick and Biddle, 1985).

2.3 Wrench Fault Models

Given the complexities of wrench fault structures a series of laboratory measurements simulating wrench fault tectonics have been conducted in recent years. McClay (2001) developed scaled sandbox models to develop an understanding of the geometries and kinematics of complex 3-D structures in sedimentary basins. His laboratory measurements simulate the formation of wrench faults using scaled analog sandbox models. His models and observations have been applied to the Rulison data by the author, and clear analogies can be observed. The next section will briefly outline the laboratory work conducted by McClay (2001), with frequent references to observations made by other authors who have conducted similar laboratory experiments.

The scaled analog models, created by McClay (2001), were carried out using 5 cm thick sandpucks in a 120 x 60 cm deformation sandbox. The baseplates of the model were displaced by a stepper motor to produce sinistral strike slip displacement at the base of the model. The models have a scaling ratio of $\sim 10^{-5}$ such that 1 cm in the models represents ~ 1 km in nature. Figure 2.3 shows a series of vertical sections and a line diagram of the surface of experiment W303 after 10 cm sinistral strike-slip displacement on the basement fault system. The vertical cross sections clearly show how the basement faults splay and diverge into the sandbox model, forming the characteristic palm tree structures. The palm tree structures initially formed as separate segments and eventually

interconnected to form continuous faults as the shearing continued on the basement faults. The braided palm tree structures are asymmetric and dominated by the same slip sense as the basement fault. Reverse and normal faulting is also evident, but not as dominant as strike-slip motion. The sandbox model illustrate the structural complexities associated with wrench fault systems.

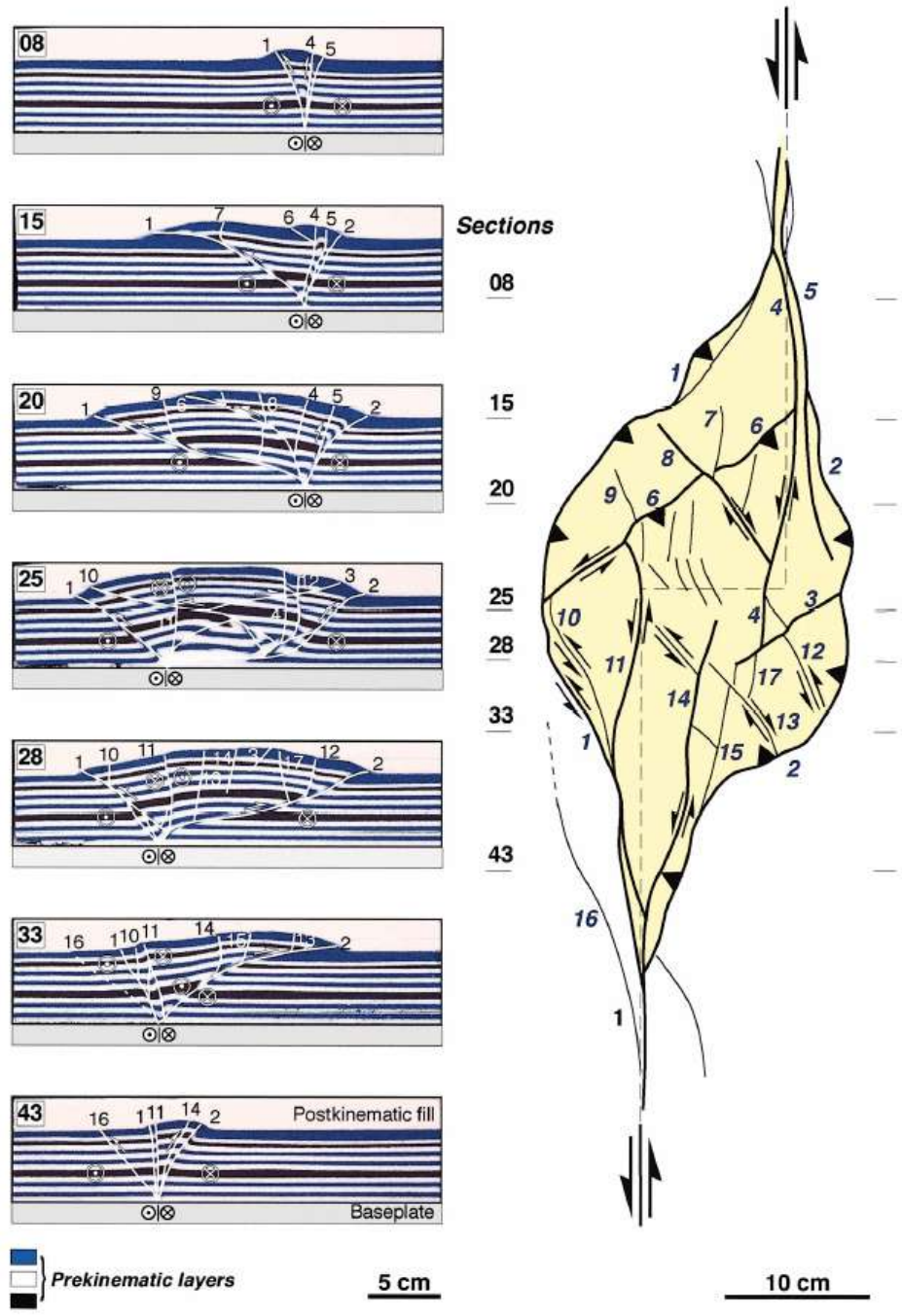


Figure 2.3: Laboratory measurements simulating wrench fault tectonics after 10 cm strike-slip displacement. Faults are numbered to permit correlation between the plan view diagram and the vertical sections. See text for discussion. (Results and image from McClay, 2001).

In addition to the palm tree structures, stepovers are created, connecting the main strike-slip events (Figure 2.3). Such stepovers, often referred to as en echelon faults are a prominent feature in wrench fault systems. The term en echelon refers to “a stepped arrangement of relatively short, consistently overlapping or underlapping structural elements that are approximately parallel to each other, but oblique to the linear zone in which they occur” (Biddle and Christi-Blick, 1985). As the amount of displacement on the main strike-slip faults increase, more en echelon stepovers develop connecting the main strike-slip events. The stepovers experience less sense of displacement than the major strike-slip events (McClay, 2001; Sylvester, 1984). Note that some of the stepover faults have a displacement sense opposite that of the main strike-slip faults, and are right-lateral in this left-lateral wrench model. These oblique movements causes the faults to converge or diverge as wrenching proceeds. Areas where converging or diverging faults intersect experience change in stress conditions and are more likely to fracture. Diverging fault intersections creates zones of compression and diverging fault intersections create zones of extension. Extension fractures are dominantly developed in the extensional quadrants of the fault segments (Y.S. Kim et al., 2004). Areas of fault intersections are therefore important to identify as they may contain zones of enhanced natural fractures, providing the necessary permeability for commercial gas production at Rulison Field.

The en echelon faults combined with the palm tree structures break the model up into a variety of fault blocks within the principal displacement zone, colored in yellow (Figure 2.3). The individual fault blocks are separated by faulting, and tend to deform independently. The majority of the fault blocks in McClay's model rose due to the compression in the stepover zone. However, laboratory clay models simulating similar wrench tectonics by Wilcox et al. (1973) showed that some fault blocks rise, some sink, some are folded and some are faulted again in a wrench fault system. The compressive deformation and wrenching causes the fault blocks to rotate. Although rotation directions may vary, a left-lateral wrench has an external sense of rotation that is counterclockwise, whereas right-lateral wrenches have clockwise external rotation (Wilcox et al., 1973). The rate of fault block rotation also varies significantly and is dependent on size, state of stress and lithology. McClay (2001) noted that smaller fault blocks experienced an increase in rotation compared to larger fault blocks. As the individual fault blocks rotate their edges experience higher stress concentrations and are more likely to fracture. Kim et al. (2004) observed extension fractures around rotated fault blocks at Kilve, Somerset, UK., (Figure 2.4). He also pointed out that fault block corner areas experienced an increase in fracturing compared to the remaining edges of the fault blocks.

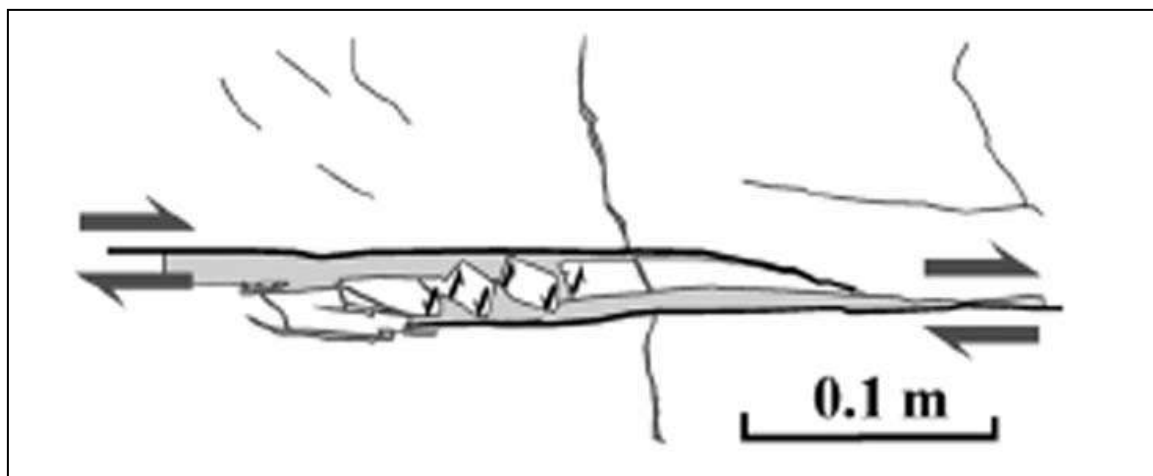


Figure 2.4: Small scale block rotation at Kilve, Somerset, UK. Similar fault block rotation, at a much larger scale, occurs in the reservoir interval at Rulison Field. (From Kim et al., 2004).

2.4 Conclusions

Experimental laboratory results provide templates for seismic interpretation of the complex wrench fault system at Rulison. We know from these laboratory measurements and natural examples that fault block rotation occurs in wrench fault systems. Natural fractures are strongly controlled by the fault block rotation and the intersections between fault segments. Observations show that fault block corner areas which experience extension are more likely to be naturally fractured. The enhanced fracture density at these extensional quadrants facilitate the transfer of considerable volumes of gas from source beds to reservoir. Fault block corners which

experience extension will therefore be essential to identify in the reservoir interval at Rulison Field to increase the production potential.

Other factors are also likely to influence the development of natural fractures, including lithology, fluid pressure and temperature. No simple model will describe all of the complexity in the deformation that occurs around faults (Kim et al., 2004). Despite the limitations, the usefulness of the analog models in understanding the progressive evolution of wrench fault systems is demonstrated by the strong geometric relationship between the models and the Rulison Field. Natural fracture prediction based on structural interpretation is more reliable by applying analog laboratory observations. Nevertheless, these analogs help give a 3-D view of typical deformation structures and geometries associated with wrench fault systems.

CHAPTER 3
“ANT TRACKING”
AUTOMATED FAULT EXTRACTION TOOL

3.1 Introduction

Fault interpretation has commonly been a very manual task. The traditional 2-D approach, where the interpreter draws faults on top of seismic cross-sections, is time-consuming, subjective and can lead to biased fault interpretation. In most cases, there are many more seismically resolvable faults within a 3-D data set than are normally mapped during seismic interpretation (Townsend et al., 1998). As a result, seismic attributes, imaging discontinuities caused by faults and other stratigraphic features, have been developed. Coherence calculations can help extract fault surfaces, but are often heavily contaminated by noise and other artifacts making fault distinction a difficult task. To better characterize the subtle, yet complex, fault system observed at Rulison, an automated fault mapping routine was applied. The ant tracker, developed by Schlumberger Stavanger Research, is a 3-D auto-tracking fault tool which detects faults in a 3-D volume. The ant tracker analyzes all spatial discontinuities in a processed seismic volume, and extracts surfaces likely to be faults. I had the opportunity to work with the ant tracker software during a summer internship in Stavanger, Norway. The software became commercially available as part of the 2004 Petrel release.

The ant tracker was applied to the Seitel survey as well as the RCP survey to track the regional and local fault network at Rulison. The ant tracker algorithm provides reliable images of the complex faults observed in the reservoir interval at Rulison Field.

3.2 Ant Tracking Workflow

The ant tracking workflow, illustrated in Figure 3.1, consists of three independent steps:

1. Create an attribute cube which enhances the spatial discontinuities in the seismic data (e.g. chaos, coherency, variance, etc.)
2. Apply ant track algorithm which automatically analyzes all spatial discontinuities in the attribute and extracts surfaces likely to be faults to a new ant track cube.
3. Extract, validate and edit fault patches.

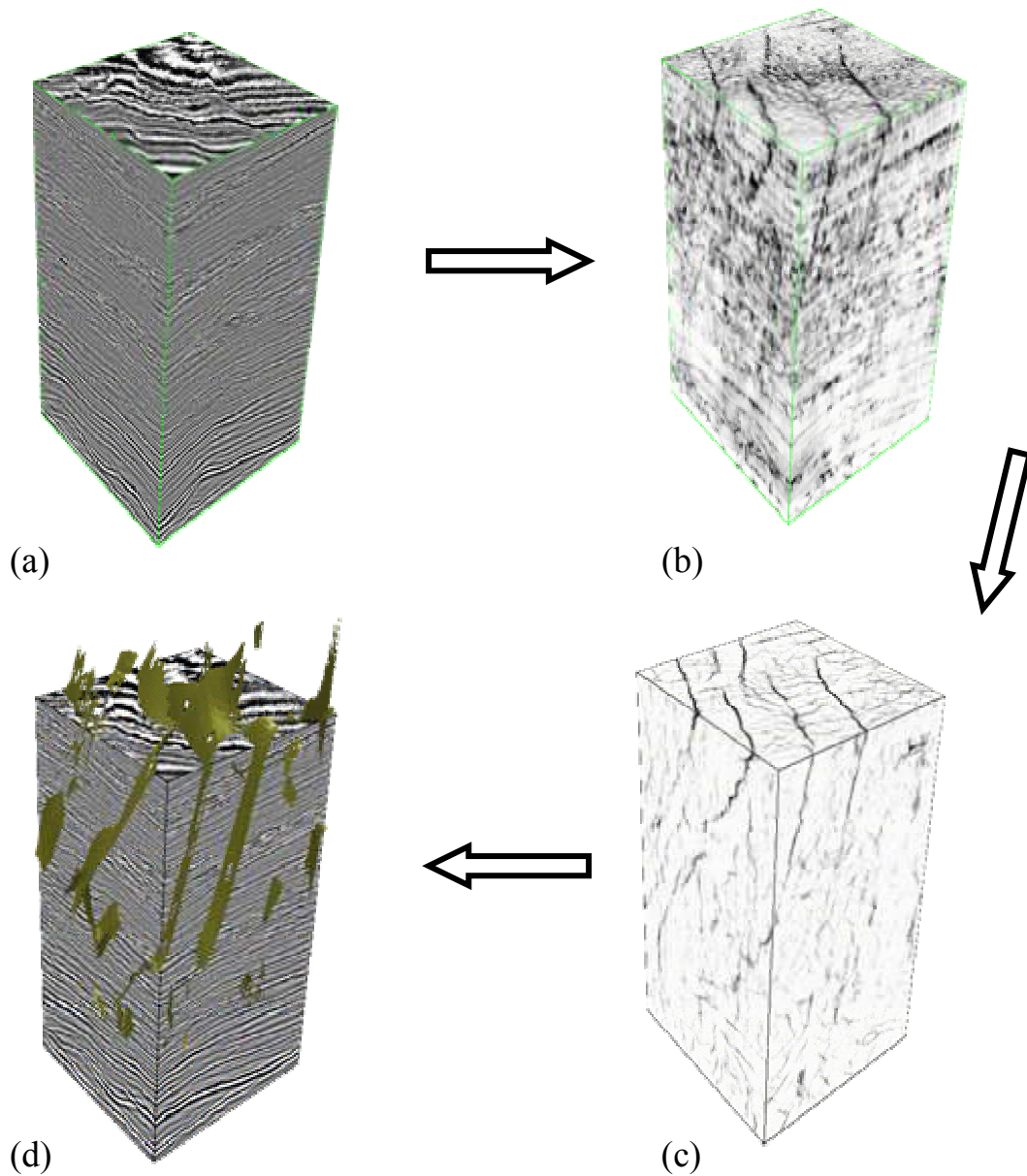


Figure 3.1: Schematic illustrating the ant tracking workflow. A chaos (coherency) cube (b) is generated from seismic cube (a). Conditioning by ant tracking is applied and the faults are enhanced in the ant tracker cube (c). The fault surfaces are extracted and displayed as 3-D fault patches (d). (From Pedersen, 2002)

3.2.1 Fault Enhancing Attributes

The first step in the ant tracker workflow is to create an attribute which amplifies the faults. Enhancing faults means tracking discontinuities in the seismic data. The Chaos attribute is a new 3-D algorithm, developed by Stavanger Schlumberger Research, to enhance discontinuities in the seismic data. The Chaos algorithm utilizes gradient vector analysis to extract areas of discontinuity. The approach consists of three steps (Randen et al., 2000):

1. Gradient vector estimation, $\nabla x(t_1, t_2, t_3)$
2. Local gradient covariance matrix estimation, $C(t_1, t_2, t_3)$
3. Principal component analysis. The principal eigenvector represents the normal to the local reflection dip and azimuth.

The gradient vector, ∇x , represents the local dip and azimuth for each dimension in the seismic data. It is estimated by obtaining the derivative of each dimension (t_1, t_2, t_3) in a 3-D data set where each dimension has a fixed dip and azimuth (Randen et al., 2000).

$$\nabla x(t_1, t_2, t_3) = \begin{bmatrix} \frac{\partial x(t_1, t_2, t_3)}{\partial t_1} \\ \frac{\partial x(t_1, t_2, t_3)}{\partial t_2} \\ \frac{\partial x(t_1, t_2, t_3)}{\partial t_3} \end{bmatrix} \quad (3.1)$$

Calculating the gradient for each point results in one partial derivative for each dimension (t_1, t_2, t_3). The arrows in Figure 3.2 correspond to the calculated gradient vector along a reflector and illustrate the normal for each point along the layer. The reflector in Figure 3.2 varies in dip which leads to large variations in the gradient estimate for each point along the layer. From these variations we must estimate the *local dominating* dip and azimuth. The dominating orientation is computed by using principal component analysis (Randen et al., 2000).

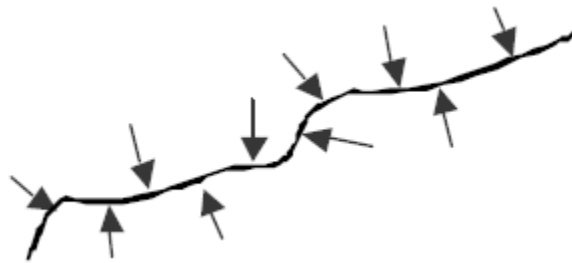


Figure 3.2: Arrows indicate the calculated gradient vector for each point along a reflection layer. From Randen et al., 2000.

The following description of principal component analysis is based on Randen et al (2000). The dominating orientation is computed by sorting the calculated gradients into a covariance matrix C :

$$C = \begin{bmatrix} C_{11} & C_{12} & C_{13} \\ C_{21} & C_{22} & C_{23} \\ C_{31} & C_{32} & C_{33} \end{bmatrix} \quad (3.2)$$

The gradients, representing the normal for each point on the reflection layer, are decomposed into its corresponding eigenvectors and eigenvalues. “The eigenvectors correspond to the three principal directions of the gradients involved in the covariance matrix with the eigenvalues indicating their magnitude. The dominating orientation is the eigenvector with the highest eigenvalue, and this vector is chosen as our local orientation estimate” (Randen et al., 2000).

The Chaos attribute follows from analyzing the dominating orientation in each point of the seismic cube. Figure 3.3, from Randen et al (2000), illustrates three situations which are distinguishable by studying the eigenvalues resulting from the principal component analysis λ_{\max} , λ_{mid} , λ_{\min} . A smooth continuous horizon will have one dominating gradient direction as illustrated in Figure 3.3a. The larger the difference between the dominating gradient λ_{\max} and the remaining λ_{mid} and λ_{\min} the more continuous the seismic data is. On the contrary, if λ_{\max} , λ_{mid} , and λ_{\min} , are similar in magnitude, the gradients will point in all directions, indicating a discontinuity, as illustrated in Figure 3.3c. Hence, a fault damage zone will have gradients pointing in all directions, and the discontinuities in the seismic data will be highlighted. By using this method, regions with low consistency, e.g. faults, correspond to regions with chaotic signal patterns.

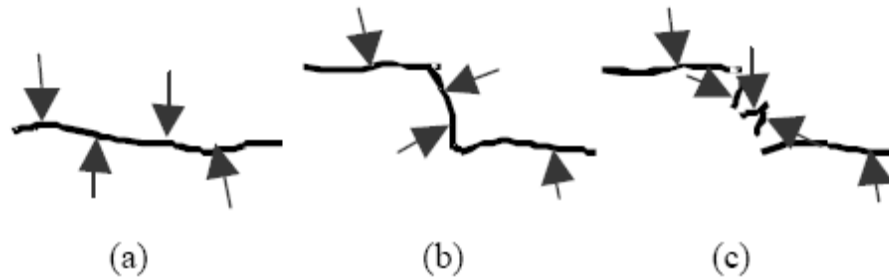


Figure 3.3: Schematics illustrating three scenarios which are distinguishable by studying the eigenvalues resulting from the principal component analysis, λ_{\max} , λ_{mid} , λ_{\min} . A dominating gradient is observed along the smooth reflector in (a) and the data is considered to be continuous ($\lambda_{\max} \gg \lambda_{\text{mid}} \approx \lambda_{\min}$). Scenario (b) and (c) are considered discontinuous because the bent reflector in (b) will have two strong directions ($\lambda_{\max} \approx \lambda_{\text{mid}} \gg \lambda_{\min}$) and the damaged zone in (c) will have gradients pointing in all directions ($\lambda_{\max} \approx \lambda_{\text{mid}} \approx \lambda_{\min}$). (From Pedersen, 2002).

In addition to structural information, the chaos attribute typically contains artifacts due to noise, residual responses from reflector interfaces, channel features, etc making it more difficult to map the faults (See figures 3.1 (b) and 3.9 (b)). In order to remove the noise and further enhance the faults conditioning of the attribute is performed by the ant tracker.

Other fault enhancing attributes such as coherence calculations is a common attribute applied to 3-D seismic data to highlight discontinuities. It differs from the chaos cube because it is based on cross-correlation of traces, not gradient analysis. “By calculating localized waveform similarity in both in-line and cross-line directions, estimates of 3-D dimensional seismic

coherence are obtained” (Bahorich and Farmer, 1995). Regions of seismic traces which propagate through a faulted zone will have a different seismic character in terms of waveform and amplitude compared to the corresponding regions of neighboring traces. As a result, sharp discontinuities appear in local trace-to-trace coherence along a faulted zone. Fault planes lack coherence and will therefore be highlighted by the 3-D coherence technique because traces are not identical on opposite sides of a fault.

Any fault enhancing attributes tracking discontinuities in the seismic data can be applied to the ant tracking workflow. However, it is essential to choose an attribute or attributes that images the faults most accurately. Several fault enhancing attributes such as chaos, coherence, variance and edge enhancement were applied to the seismic data. The chaos attribute was the preferred attribute. Randen et al (2000) pointed out that processing signatures such as vertical striping effects seen in other attributes are not present in the chaos attribute. The chaos attribute imaged the small spatial fault discontinuities observed at Rulison the best, and was therefore applied to the ant tracking workflow.

3.2.2 Ant Tracking Attribute

The ant tracker algorithm is an extension of the ant system algorithm described in Dorigo et al (1996), which was designed to solve hard combinatorial optimization problems. In order to find the optimal solution the ant tracking algorithm analyzes all spatial discontinuities in the chaos attribute to extract surfaces likely to be faults. It is based on heuristic techniques. “The term heuristic means a method which, on the basis of experience and judgement, seems likely to yield a reasonable solution to a problem, but which cannot be guaranteed to produce the mathematically optimal solution” (Silver, 2004). The term heuristic derives from the Greek *heuriskein* meaning to find or discover (Dowsland, 1993), and is used for algorithms which find “best fit” solutions among all possible ones. It pertains to the process of gaining knowledge or some desired result by intelligent guesswork rather than by following some preestablished formula. “Heuristics are usually more flexible and are capable of coping with more complicated (and more realistic) objective functions and/or constraints than exact algorithms” (Dowsland, 1993). In addition, “heuristics can be less sensitive to variations in problem characteristics and data quality” (Silver, 2004). The ant tracker uses a heuristic approach to extract optimal “best fit” solutions (fault planes) in the chaos cube.

The heuristic approach used by the ant tracker algorithm follows the principles of swarm intelligence (Pedersen, 2002). “Swarm intelligence is a term describing the collective behavior that emerges from a group of social

insects. An example is how ants find the shortest path between the nest and a food source by communicating via pheromone, a chemical substance that attracts other ants” (Pedersen, 2002). A moving ant leaves some pheromone on the ground, thus marking its path by a trail of this substance. “While an isolated ant moves essentially at random, an ant encountering a previously laid trail can detect it and decide with high probability to follow it, thus reinforcing the trail with its own pheromone. The collective behavior where the more ants following a trail, the more attractive that trail becomes and is more likely to be followed. The process is thus characterized by a positive feedback loop, where the probability which an ant chooses a path increases with the number of ants that previously chose the same path” (Dorigo, et al., 1996). Figure 3.4 shows how the shortest trail will be marked with more pheromone than the longest trail. As a result, the probability of which path the ant will follow is quickly biased towards the shorter one as it is marked by more pheromone.

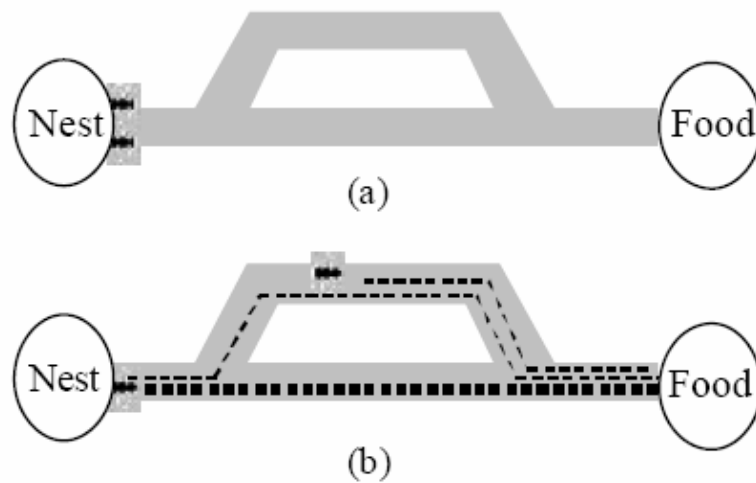


Figure 3.4: Schematic illustrating the principle of swarm intelligence, which the ant tracker algorithm is based on. Two ants start out searching for food. The ant choosing the shortest path will travel back and forth more times, thereby marking the trail with more pheromone. The next ant, which is drawn to the pheromone, is more likely to choose the shorter path. (From Pedersen, 2002).

The ant tracker disperses a large number of these electronic “ants” at different locations in a fault attribute volume, such as a chaos cube. “The electronic ants, referred to as agents, will act very similar to an ant in the foraging situation described previously, by making decisions on its pre-coded behavior and emitting “electronic pheromone” along its trail” (Pedersen et al., 2002). The agents will seek the signature of a fault along discontinuities in the chaos cube. A fault will typically form a plane of peak discontinuities rather than a volume. “For each voxel in the chaos cube, the algorithm (i.e. agents) will check whether the current voxel is the peak value of a neighborhood of n voxels forming a line perpendicular or nearly

perpendicular to the fault. If so, it is retained, otherwise it will be discarded” (Randen et al., 2001). The process repeats until the discontinuity terminates. The tracked surfaces will only be one voxel thick and are therefore easily extracted as connected components of peak discontinuities. The tracked surfaces are written to the ant tracking cube. Figure 3.5 is a schematic illustrating how the ant tracker works. A fault with offset is clearly present in Figure 3.5a. To enhance the fault a chaos attribute is created by extracting the discontinuities caused by the fault. The resulting chaos attribute is seen in Figure 3.5b and the accomodating grid of voxels (Figure 3.5c) illustrates all the extracted discontinuities and their magnitude. Note how the highest discontinuities fall directly on the fault plane and decrease away from the fault surface. The result is a “volume” of discontinuities rather than a distinct fault plane. To limit the uncertainty of where the fault plane actually is within the extracted discontinuities, the ant tracker algorithm is applied. The ant tracker algorithm releases a large number of agents into the (sub-optimal) chaos cube and searches the attribute for a more accurate solution. By applying a heuristic technique the algorithm will check each voxel and extract peak discontinuities which form a plane. The result is a much more accurate representation of the fault plane as seen in Figure 3.5d. Furthermore, Figure 3.5e illustrates how the ant tracker has extracted and connected the peak discontinuities to form a much narrower and more accurate fault plane. These planes of peak discontinuities are written to the ant tracking cube and is more likely to achieve a more optimal fault model than conventional fault enhancing attributes.

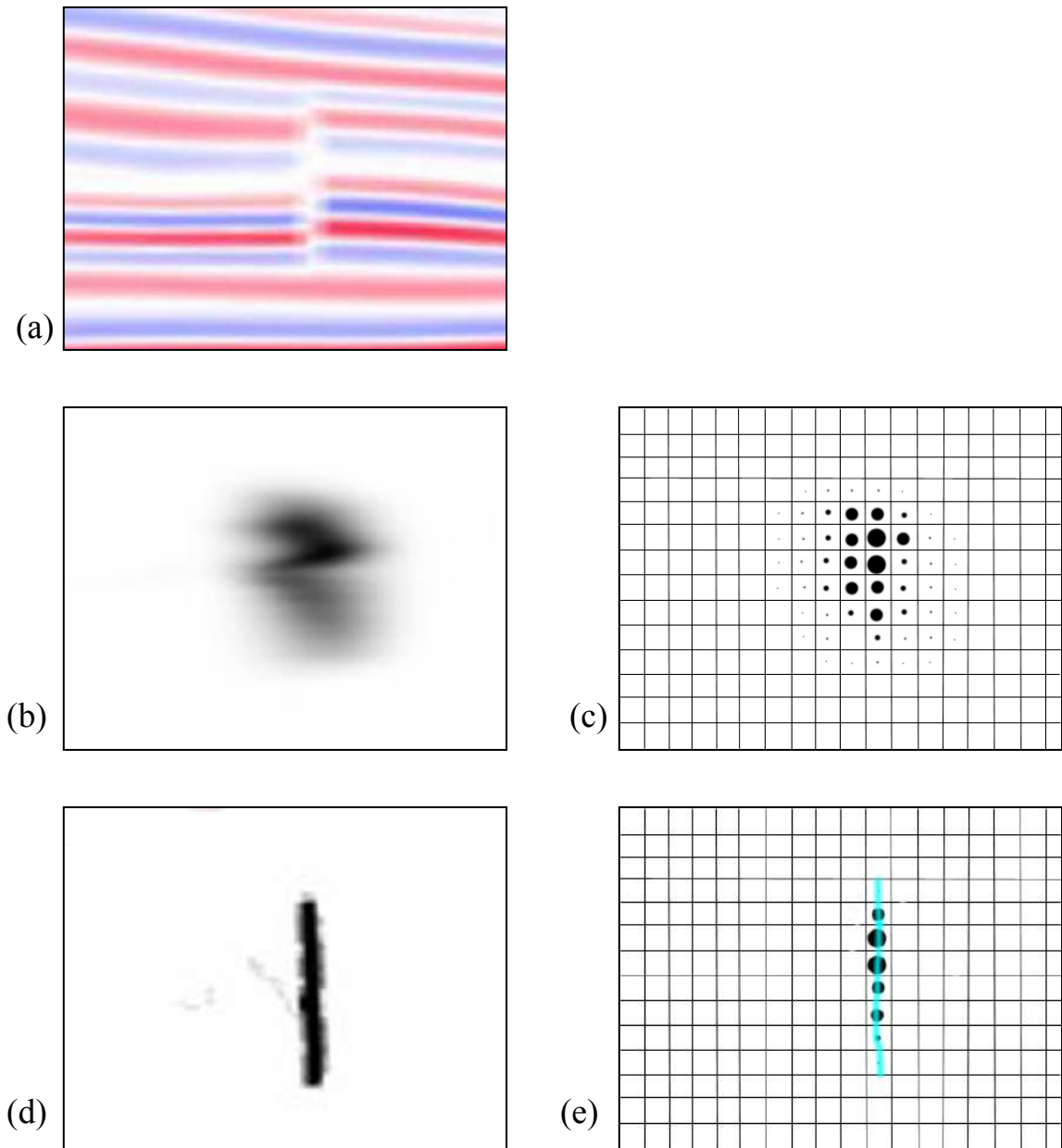


Figure 3.5: a) Fault cutting through seismic section. b) Chaos cube enhancing discontinuities caused by the fault. c) Grid illustrating the magnitude of discontinuity at each voxel surrounding the fault. d) Resulting ant track cube. e) Grid illustrates how the ant tracker has only extracted and connected the peak discontinuities associated with the fault.

By deploying a large number of agents into the chaos attribute, each agent will move along what appears to be a fault surface while emitting pheromone. “Agents deployed at points where there is no surface, only unstructured noise, or where there is a surface which does not fulfill the conditions of a fault (e.g. remains of a reflector or a channel), will be terminated shortly or immediately after their deployment” (Pedersen et al., 2002). Surfaces meeting expectations of a fault will be heavily marked by “pheromone”. Hence, if many agents follow the same path of peak discontinuities, and the trail has the appearance of a plane, it is an indication that the tracked discontinuities could be a fault. The amount of “pheromone” left behind is a confidence measure. The result is a 3-D attribute cube which enhances fault zones with more accuracy than conventional coherency cubes.

According to Pedersen (2005), non structural features such as noise and channels will typically have chaotic texture internally, and this may prevent noise and channel features from being extracted equally well as faults. The ant tracker extracts features that have a surface shape. If the chaotic texture of noise and/or a channel makes them appear more like a volume in the attribute than a bounding surface, the ant tracker may avoid extracting the noise and channel features. As a result, fault surfaces are enhanced and non-structural features such as noise and/or channels with the appearance of a volume in the attribute will be repressed.

Unlike the coherency and other conventional fault attributes, the ant tracker allows the user to manually interact with the data. The user can adjust the level of detail to be extracted from the data by adjusting up to six parameters. For example, the more agents released into the volume, the more details will be extracted. Also, if a higher “freedom” is given to the agents, they will search a larger number of voxels on either side of the tracking direction allowing more connections to be made. Increasing such parameters as deviation and step size will allow the agents to search further, finding more connections, but at a coarser resolution. The agents can also be instructed to search beyond its current location where no edge has been detected, referred to as an illegal step. This is an important parameter for tracking discontinuous edge events often associated with the strike-slip faults observed at Rulison. The latter parameter can be constrained by requiring a certain number of “legal steps” to be made after an illegal step has been applied. By adjusting these parameters one can guide the agents to extract structural features at a much more detailed level than conventional fault attributes. Table 3.1 lists the parameters which can be adjusted to guide the agents.

Table 3.1: Ant tracking parameters (Conditions the behaviour of the agents)

- Initial Ant Boundary (Number of voxels):

This parameter controls how closely the number of Ant agents is deployed within the volume. The distance is measured in terms of voxels. The larger this number, the fewer the Ants will be deployed and consequently, the less detail will be captured.

Minimum: 1

Maximum: 30

- Ant Track Deviation (Number of voxels):

This parameter will allow the Ants to search for a larger number of voxels on either side of its tracking direction. A larger value will allow the ants agents to find more connections between points.

Minimum: 0

Maximum: 3

- Ant Step Size (Number of voxels):

This parameter defines the amount of voxels an Ant agent advances for each increment within its searching step. Increasing this value will allow an Ant agent to search further, but it will lower the resolution of the result.

Minimum: 2

Maximum 10

- Illegal Steps (Number of voxels):

This parameter defines how many voxels an Ant agent is allowed to search beyond its current location when a zone without an edge has been detected. This will determine the behavior while tracking discontinuous fault events. The larger this value, the further an Ant agent will look for a connection.

Minimum: 0

Maximum: 3

- Legal Steps (Number of voxels):

This parameter works in combination with the Illegal Steps parameter. It describes the number of required valid steps after an Illegal step. The lower this number, the less restrictive the action and consequently more connections can be made.

Minimum: 0

Maximum: 3

- Stop Criteria (%):

This parameter also works in combination with the Illegal steps. It controls the termination of Ant agents advancing when too many Illegal steps have been taken. The larger this value in percentage, the further Ants will be allowed to advance.

Minimum: 0

Maximum: 50

(From Petrel Workflow Tools, 2004)

The discontinuities corresponding to fault surfaces in the ant tracker cube can be extracted and viewed as 3-D fault patches. The parameters listed in Table 3.2 conditions the surface to be extracted from the ant tracking cube. The extracted fault patches are evaluated and filtered in order to obtain the final interpretation. This editing is done “using an innovative approach applying interactive stereo-net and histogram filter tools” (Pedersen, 2002). The ant tracker is an automatic fault extraction tool, but this last step allows the interpreter to edit the data. The final fault patches accompanied by time slices of the ant tracker cube are used to understand and better characterize the complex fault network present at Rulison. The results will be discussed in Chapter 4.

Table 3.2: Surface parameters (Conditions surfaces to be extracted from ant tracking cube)

- Minimum Patch Size (Points)

Fault patches containing fewer than this number of points will be excluded from the fault patch set. A larger number will consequently yield to larger fault patches and leave out the small fault patches, hence generating less fault patches in total. You can also filter fault patches using the histogram filter on the Fault Patch settings.

- Patch Down Sampling (Voxels)

This parameter controls the density of points within each fault patch. This parameter works in combination with the Minimum Patch Size. The output points in a patch will be no closer together than the defined points.

Minimum: 1

Maximum: 20

- Maximum Separation (Voxels)

This parameter controls how many voxels apart two fault patches have to be in order to be merged. It also controls how far a patch can be from an estimated plane.

- Maximum Change in Dip (Degrees)

This parameter estimates and compares the maximum change in average dip between two patches as an acceptance criterion for merging.

Minimum: 0

Maximum: 90

- Maximum Change in Azimuth (Degrees)

This parameter estimates and compares the maximum change in average azimuth between two patches as an acceptance criterion for merging.

Minimum: 0

Maximum: 90

(From Petrel Workflow Tools, 2004)

3.3 Synthetic Model

Before applying the software to the Rulison data, I tested its accuracy on a synthetic data set created in conjunction with researchers at SSR Schlumberger. Eleven fault patches with different strike and dip were created in a synthetic seismic cube. The goal was to test how accurately the ant tracker would image the faults. The previously described ant tracking workflow was applied to the synthetic data. The results can be seen in Figures 3.6-3.9, which show a vertical slice through the synthetic seismic cube, the corresponding chaos cube, the resulting ant tracking cube and finally the extracted fault patches, respectively. Inline 2050 (Figure 3.6-3.9) intersected five of the eleven synthetic faults. The 3-D fault patches which were extracted from the ant tracking cube can be seen in Figure 2.8. All the faults were accurately extracted using the ant tracker. Note that the final fault patches in the synthetic cube (Figure 3.9) also include an estimate of displacement. The displacement algorithm was not applied to the Rulison data as it is still being tested.

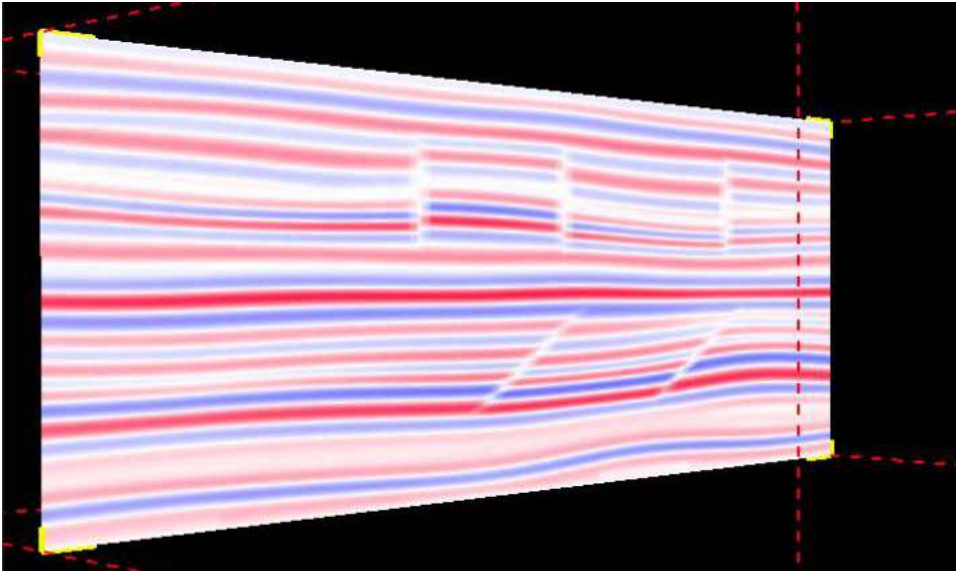


Figure 3.6: Line 2050 through a synthetic seismic cube showing five clear faults.

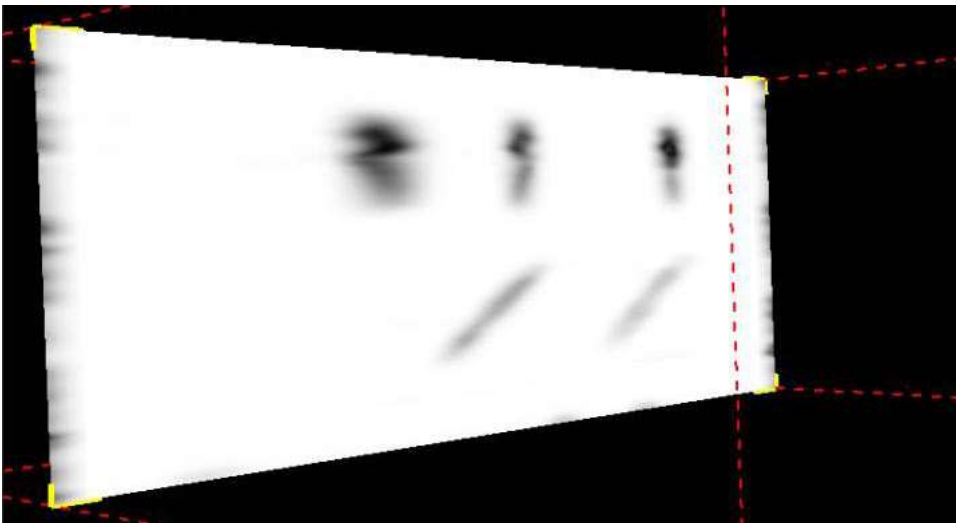


Figure: 3.7: Line 2050 through a chaos attribute created from the synthetic cube shown in the previous figure. Shaded areas correspond to areas of faulting.

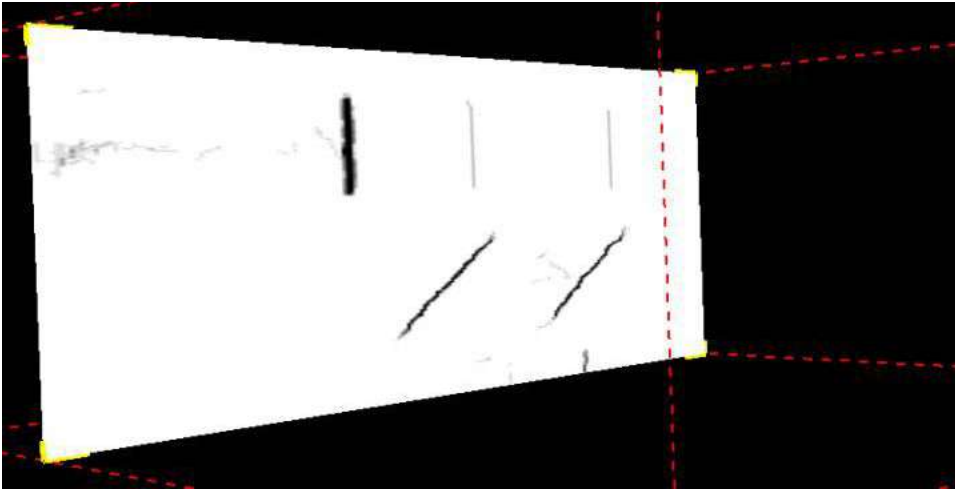


Figure 3.8: Line 2050 through an ant track cube created from the chaos cube shown in the previous figure. The ant tracker has performed a “thinning” operation by extracting the peak discontinuities. The resulting five faults are displayed as black/gray lines.

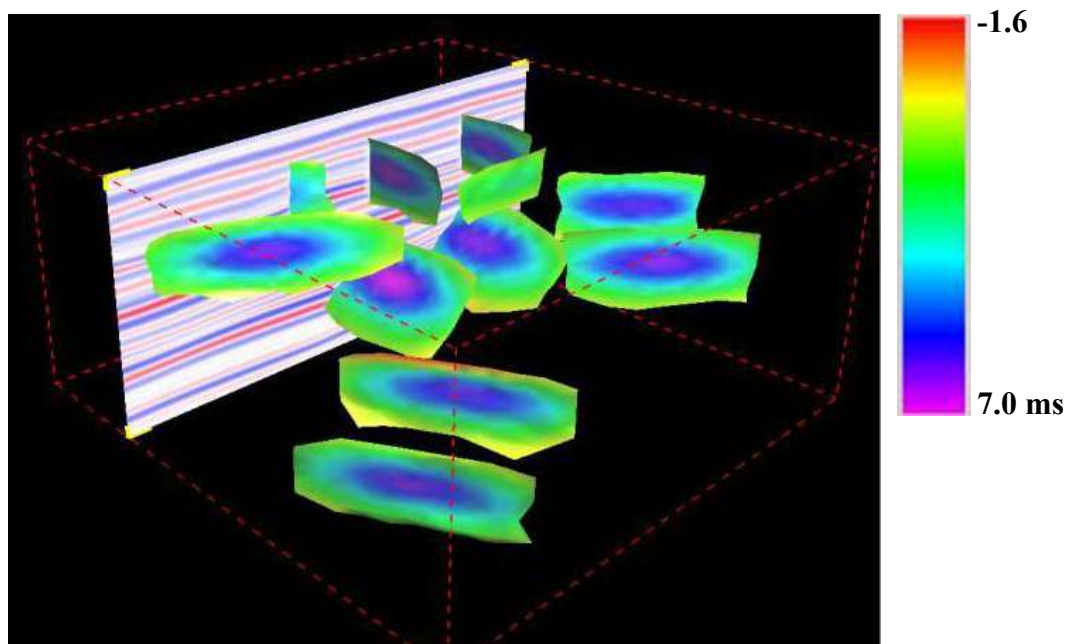


Figure 3.9: All synthetic fault patches extracted from the ant track cube. Seismic line 2050 is intersected by five faults. Color bar indicates amount of throw on the fault patches (ms).

3.4 Applications to Rulison Data

The main obstacle encountered in interpreting seismic data for fault recognition at Rulison Field is the small vertical displacement on the faults. Even in the case of high definition 3-D seismic these small displacement faults are difficult to detect and are therefore often overlooked at Rulison (Kuuskraa et al., 1997). The ant track attribute provides a smoother image of the faults compared to conventional P-wave data and the resulting chaos cube. To further illustrate the value of the ant tracker, a time slice at 1200 ms (lower reservoir) has been extracted from the Seitel P-wave volume, the resulting chaos cube and the calculated ant track cube (Figure 3.10). The RCP study area has been outlined by black square. The faults are clearly more visible in the ant tracker attribute compared to the corresponding time slice through the chaos cube. The faults in the ant tracker attribute are more continuous and narrower making it easier to identify the faults with higher precision. Note the southwest corner where the chaos cube has traced unstructured noise making fault interpretation a difficult task. The fault detected by the ant tracker in the same area has not been affected by the unstructured noise and can clearly be interpreted. The actual fault is shown on a cross section of the raw data in Figure 3.11. The ant tracker algorithm isolates real structural features from noise and surfaces that do not fill the requirements of a fault surface in Rulison Field. The level of structural detail provided by the ant tracker algorithm allows for a much more descriptive characterization and understanding of the subtle fault network at Rulison Field.

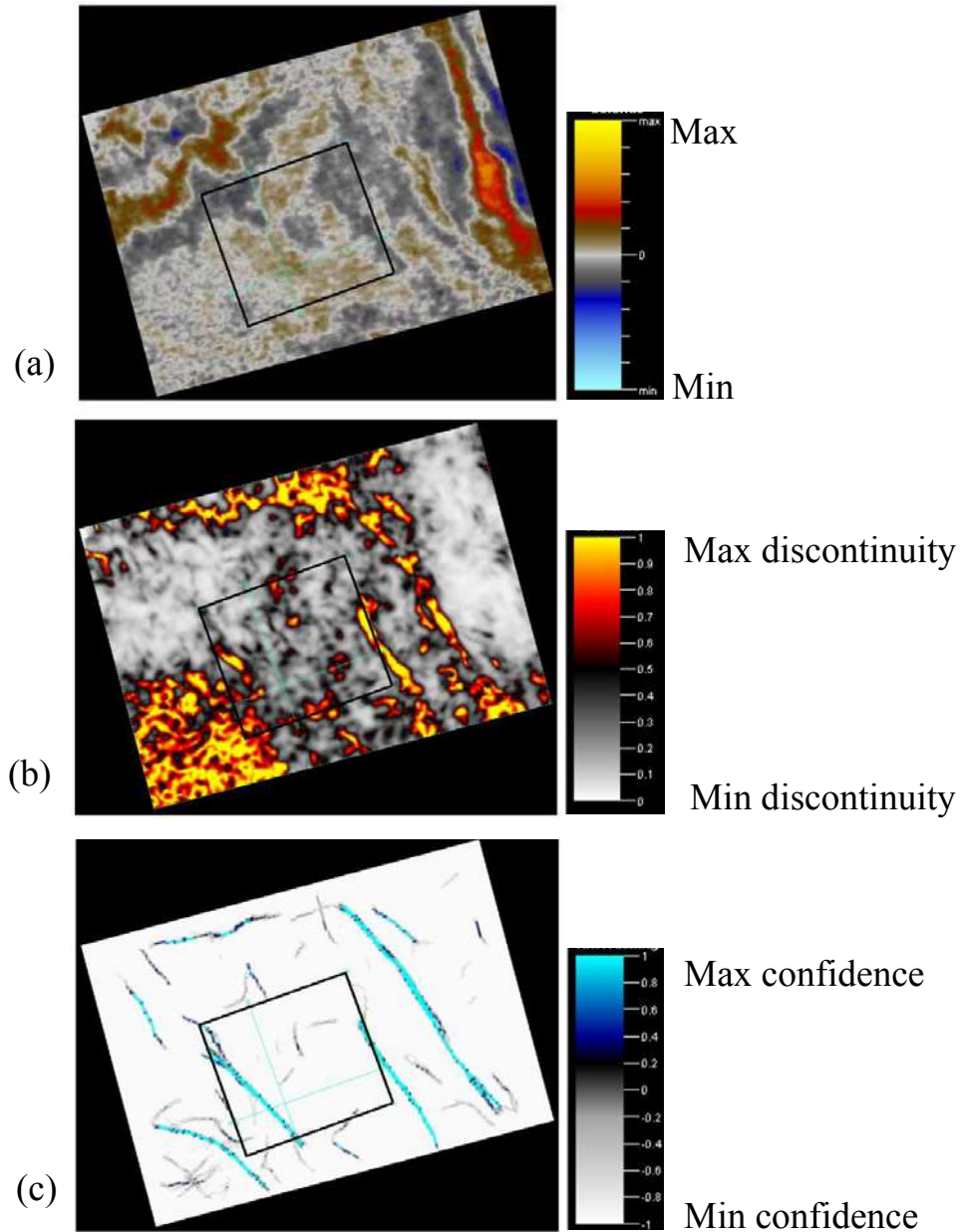
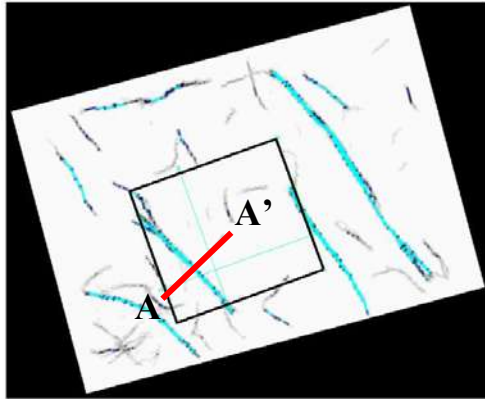


Figure 3.10: Map view of three time slices at 1200 ms (lower reservoir), illustrating the value of the ant tracker. RCP study area outlined by black square. a) Seitel P-wave volume, b) chaos cube and c) the resulting ant tracking cube. The ant tracker scale represents how many times a feature has been tracked and is a measure of confidence.



A
SW

A'
NE

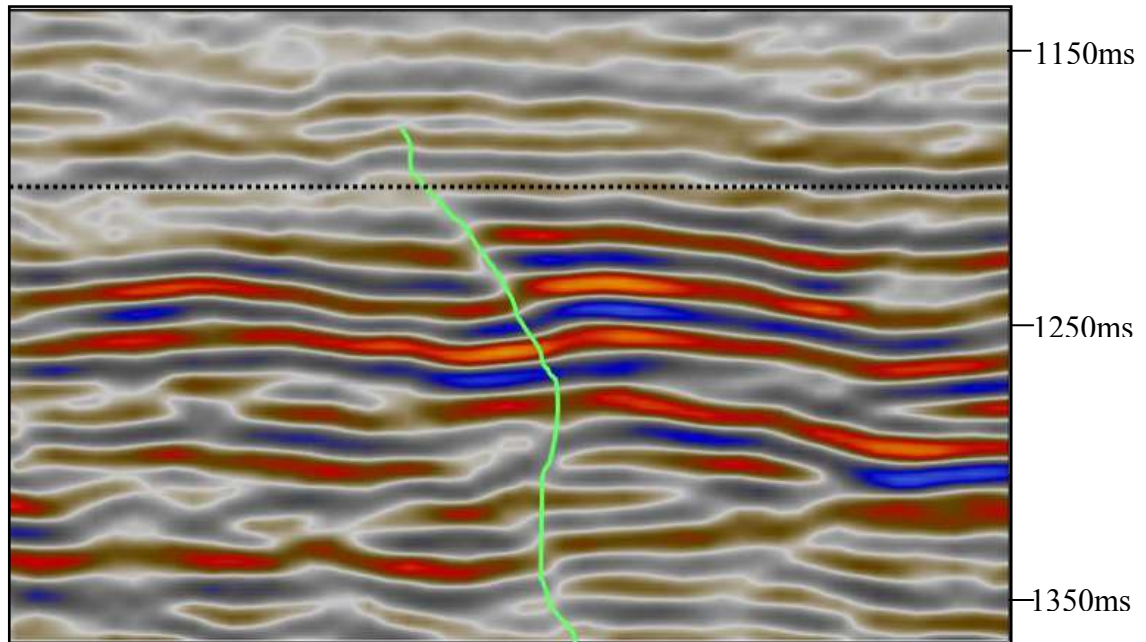


Figure 3.11: Cross section (A-A') intersecting fault detected by ant tracker in southwest corner at RCP's study area in Rulison Field. Fault path traced by ant tracker in green has been slightly edited by author. Dotted line represents time slice at 1200 ms as seen in Figure 3.10.

3.5 Conclusions

The subtle faults observed in the reservoir are extremely difficult to trace as they show very little reflector offset. These subtle faults are therefore often overlooked, but are essential to detect in order to predict areas of enhanced fracturing. Kuuskraa et al. (1997) pointed out how subtle fault systems can significantly fracture an otherwise tight gas reservoir, and are therefore crucial to characterize. The ant tracker algorithm provides a powerful 3-D automated technology for identifying and enhancing the subtle structural features observed at Rulison. Modeling these faults is essential to gain a detailed insight into the evolution, structure and properties of the natural fractures at Rulison.

CHAPTER 4

INTERPRETATION OF WRENCH FAULTS AT RULISON

4.1 Introduction

Natural gas production from the low permeability Mesaverde Formation in the Piceance Basin is enhanced by the presence of open natural fractures (Hoak and Klawitter 1997; Kuuskraa et al., 1997; Hemborg, 2000, Cumella and Ostby, 2003). The occurrence of these natural fractures is linked to faults. Fracture zones are associated with fault corners and fault intersections. The small displacement faults are difficult to detect and often overlooked at Rulison (Kuuskraa et al., 1997), but with the help of fault enhancing attributes the complex fault system has been characterized revealing that wrench faulting is the main characteristic.

4.2 Basin Stress History

Natural fractures in a given rock mass are the result of its integrated tectonic and stress histories (Lorenz, 1985). A review of the tectonic and stress histories of the Piceance Basin will therefore be given in this section. The tectonic and stress history information has mostly been gathered from John C. Lorenz's work based on analysis and interpretation of compiled data, including results from the Department of Energy's Multiwell Experiment site (Lorenz, 1985; Lorenz and Finley, 1991 and Lorenz et al., 1997). The stress and tectonic histories create an empirical framework for

modeling the fault network and its link to natural fractures in the Mesaverde Formation.

The Cretaceous to present tectonic history of the Piceance Basin has three basic subdivisions: Sevier, Laramide, and post-Laramide (Lorenz, 1985). The Sevier orogenic episode, lasting from about 160 to 72 m.y. (million years before present), was a time of regional east-west compression. During this time a fold and thrust belt formed in Utah, west of the Rulison Field. The fold and thrust activity formed mountains which brought sediments eastward filling in the Cretaceous Seaway.

At about 72 m.y. the tectonic pattern changed to that of the Laramide orogenic episode, but the stress regime was still one of east-west compression, and there was chronological overlap of the two orogenic styles of deformation (Tweto, 1980). The continuous overthrust belt from the Sevier orogenic episode, gradually became inactive, while the more isolated mountain ranges of the Cordilleean foreland to the east (such as the Wind River, Uinta, and Laramide Mountains) began to be uplifted. Deposition of the upper Mesaverde group ceased at this time, and the Rulison area was influenced by uplift and erosion. Spencer (1984) has suggested that significant gas generation in the nonmarine Mesaverde rocks began at about 48-52 m.y., caused by organic maturation of the coal-bearing intervals, and high pore pressures accompanied this maturation process (Lorenz, 1985).

Lorenz (1985) reported that the difference in the structural deformation styles between the Laramide and Sevier tectonics of the central Rockies has been ascribed to a change in the subduction angle of the Pacific plate in that region (Cross and Pilger, 1978). An alternate interpretation involves changes in thermal properties of the local crust associated with the extensive plutonism of the Sierra batholiths (Armstrong, 1974).

There is still controversy regarding the mechanisms of uplift of the Laramide mountain ranges. However, Berg, 1962 and Gries', 1983b, theory has been most widely accepted. It suggests that horizontal compressive forces created low-angle thrust faults which cut through basement, and that the mountain ranges were uplifted by thrusting blocks of thick crust along these faults (Lorenz, 1985).

The Mesaverde reservoir was at maximum depth of burial at about 36-40 m.y. during the early stages of the Post-Laramide Tectonics (40 m.y. – present) (Lorenz and Finley, 1991) Since then, the Mesaverde Formation has been uplifted by several episodes of regional uplift. The Post-Laramide regional uplift has been associated with volcanism and the formation of the Basin and Range extensional tectonic regime (Lorenz, 1985).

The most likely times of fracture formation are during times of tectonically induced stress and deformation. Some stresses were induced to the Mesaverde Formation through time by the overburden, by increased heat with depth, and by internal pore pressure. However, tectonism is required to produce a horizontal stress differential sufficient to both create fractures and

to control their orientation (Lorenz et al., 1991). The Sevier overthrust belt to the west in Utah, and the Laramide, White River upthrust block at the eastern edge of the basin (Figure 1.2) are the two most likely tectonic sources of horizontal stress anisotropy (Lorenz and Finley, 1991). This stress system could have produced the observed wrench fault network that I have linked to the formation of the natural fractures at Rulison Field.

4.3 Regional Fault Network

The faults interpreted at RCP's study area at Rulison are part of a larger scale fault system for which wrench faulting is characteristic. It is important to understand the regional fault network before we focus on the specific fault tectonics which influence RCP's study area at Rulison. I therefore combined my own observations on the Seitel data, with those of Cumella and Ostby (2003), to get a regional overview of the fault tectonics in the central Piceance Basin. A summary of the regional fault observations follows in this section.

Figure 4.1 illustrates faults that were interpreted on the regional Seitel survey by Stephen P. Cumella and Douglas B. Ostby (Cumella and Ostby, 2003). They reported that left-lateral strike-slip faults exist along pre-existing northwest-trending faults, and that these faults resulted from east-west Laramide compression in the Piceance Basin. Their observations also showed that major fault zones in the Mesaverde are typically located above

deeper fault zones as seen in Figure 4.1. Major faults show large offsets at the Dakota level and are easy to detect at Parachute Field. Minimal offset has been observed at the Dakota level at Rulison Field, making fault interpretation more ambiguous. The faults are difficult to trace through the relatively seismically transparent Mancos Shale interval. However, the faults clearly show offset again in the coal layers below the Cameo level. Cumella and Ostby (2003) reported that the faults splay and die out upward leaving the upper part of the Mesaverde formation relatively unfaulted. My studies show that the reservoir zone is extensively faulted and will be discussed in section 4.4.

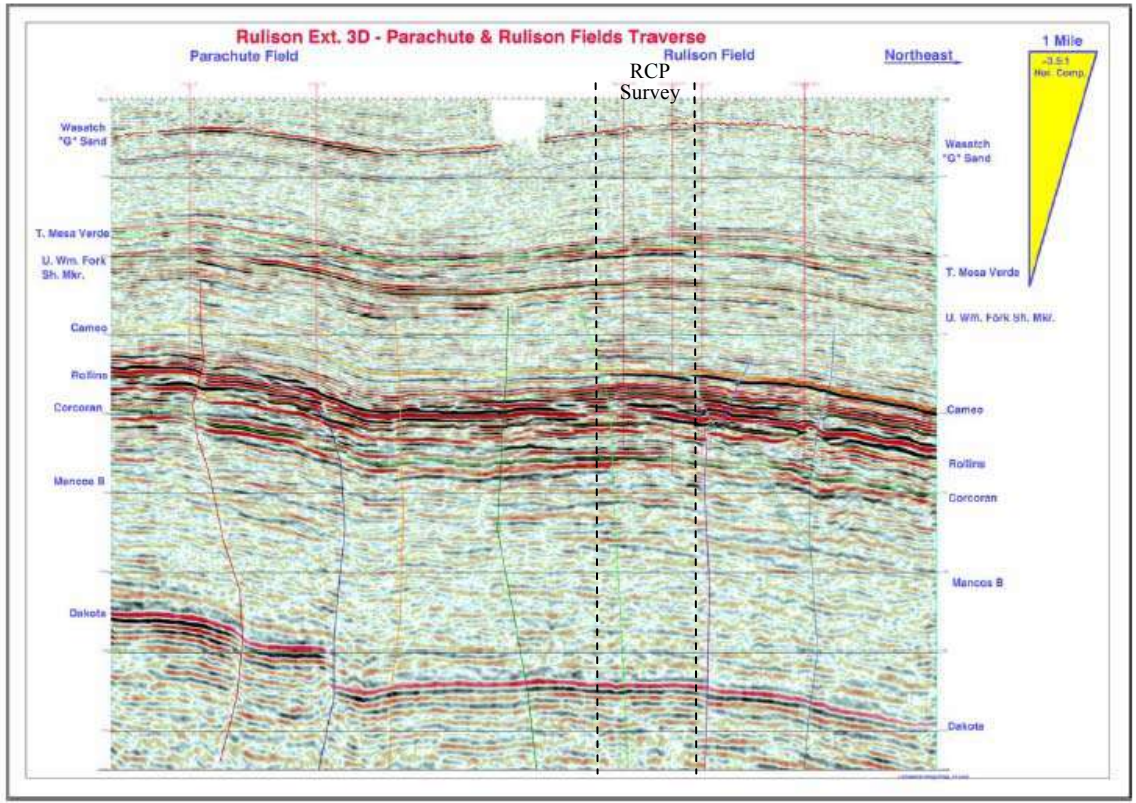
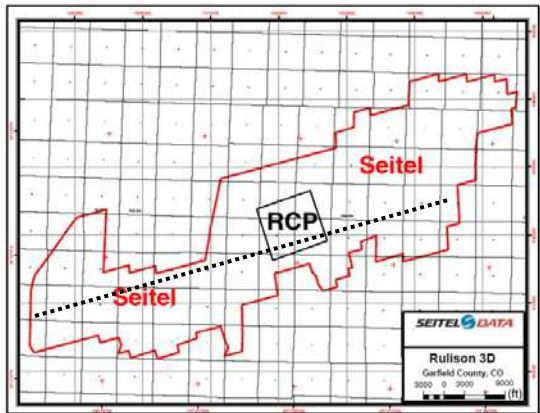


Figure 4.1: Seismic crossline of Seitel data through Rulison and Parachute Fields illustrating regional fault tectonics in the central Piceance Basin. RCP study area outlined by dotted lines. Interpretation is that of Steve P. Cumella and Douglas B. Ostby (2003). (From Cumella and Ostby, 2003).

4.4 Wrench Fault Interpretation in Rulison Field

Wrench fault tectonics controls the formation of natural fractures at Rulison Field. The subtle, yet complex, wrench faults are difficult to detect and are therefore often overlooked (Kuuskraa et al., 1997). The ant tracker algorithm provides a powerful tool for identifying the faults that provide the essential fractured flow pathways necessary for commercial production from the low permeability reservoirs at Rulison Field.

The ant tracker software for fault detection, provided by SSR Schlumberger, was applied to the Seitel data set (Figure 4.2). The black square represents the RCP study area at Rulison. The time slice of the ant track cube at 1300 ms (through the Cameo Coal Zone) clearly shows a linear northwest trend of the faults. The northwest trend direction is sub-parallel to the present day west-northwest horizontal principal compressive stress as discussed previously (Lorenz and Finley, 1991). Analysis of the ant tracker cube shows that the faults at the Dakota level and deeper also trend in a northwest direction suggesting there is a linkage between deeper faulting and the shallower subsurface structures affecting the reservoir. One can also detect minor northeast trending stepovers, connecting the larger, more continuous northwest trending faults. Analysis of the ant tracking cube shows that more northeast stepovers occur in the vicinity of the RCP survey. Here the formation has been broken up into a series of fault blocks by both the northwest trending faults and the northeast stepovers. These fault blocks experience rotation and are much more likely to generate natural fractures

than areas where no block rotation occurs. Note that the ant tracker has traced the edges of the Seitel survey, with no edge effects across the RCP study area. With these regional observations in mind I focused my fault analysis on an approximately 8 km grid, covering the RCP survey area.

The majority of the faults in the Piceance Basin, which influence the reservoir interval, are interpreted to be wrench faults due to their limited vertical offset, linear strike and upward diverging characteristics. Figure 4.3 shows cross section A-A' taken perpendicular to the major northwest trending faults at Rulison. The majority of the interpreted faults on the cross-section possess the wrench characteristics mentioned. Note how the larger faults diverge and splay upward into a series of branches characterized by reflector offset, amplitude dimming and generally poor amplitude coherency. The diverging nature of these faults have also been discussed by Kuuskraa et al. (1997).

The faults system shown in Figure 4.3 includes more details than the fault system presented by Steve P. Cumella and Douglas B. Ostby (2003) in Figure 4.1. Cumella and Ostby have identified the largest fault zones at Rulison, but have not presented the diverging nature of these faults. My interpretation shows that the faults are more extensive and splay upward as they propagate into the reservoir zone. Such wrench fault interpretation is more realistic at Rulison given the complex structural and tectonic evolution of the Piceance Basin.

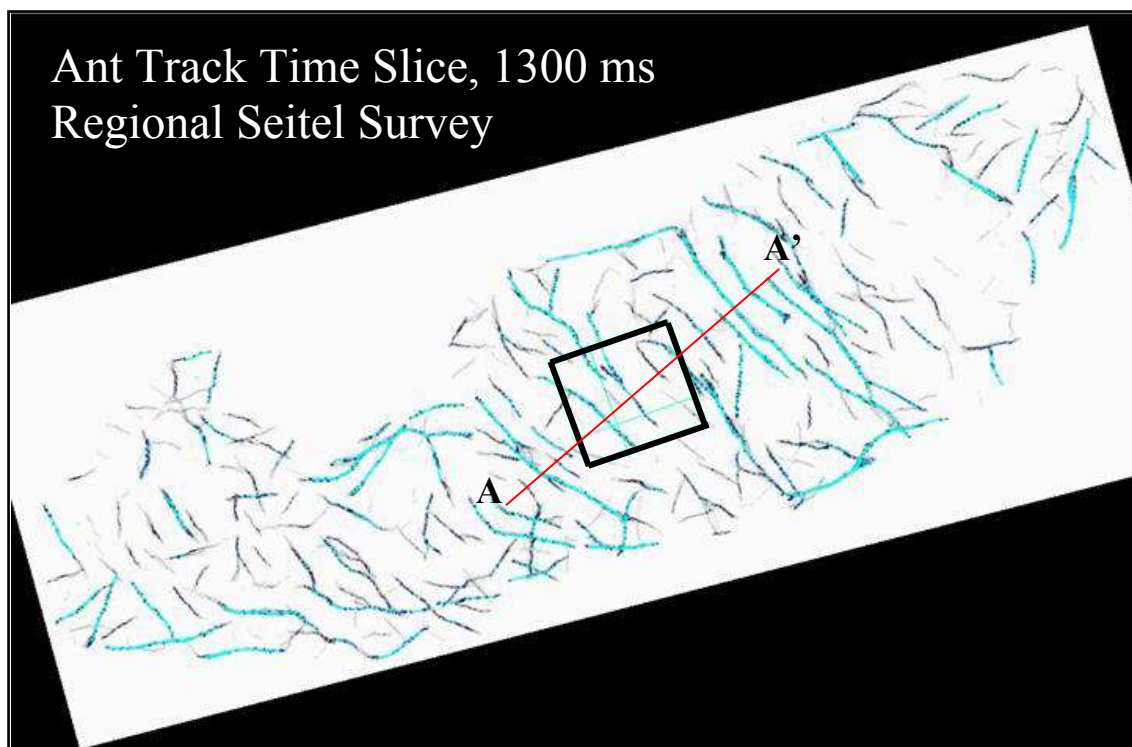


Figure 4.2: Time slice of entire Seitel survey at 1300 ms TWT from computed ant track attribute (through Cameo Coal Zone). Blue lines indicate fault architecture at this depth. Faults trend predominantly in a northwest direction with a few northeast stepovers present. RCP survey area is outlined by black square. Red line A-A' indicates cross section shown in Figure 4.3.

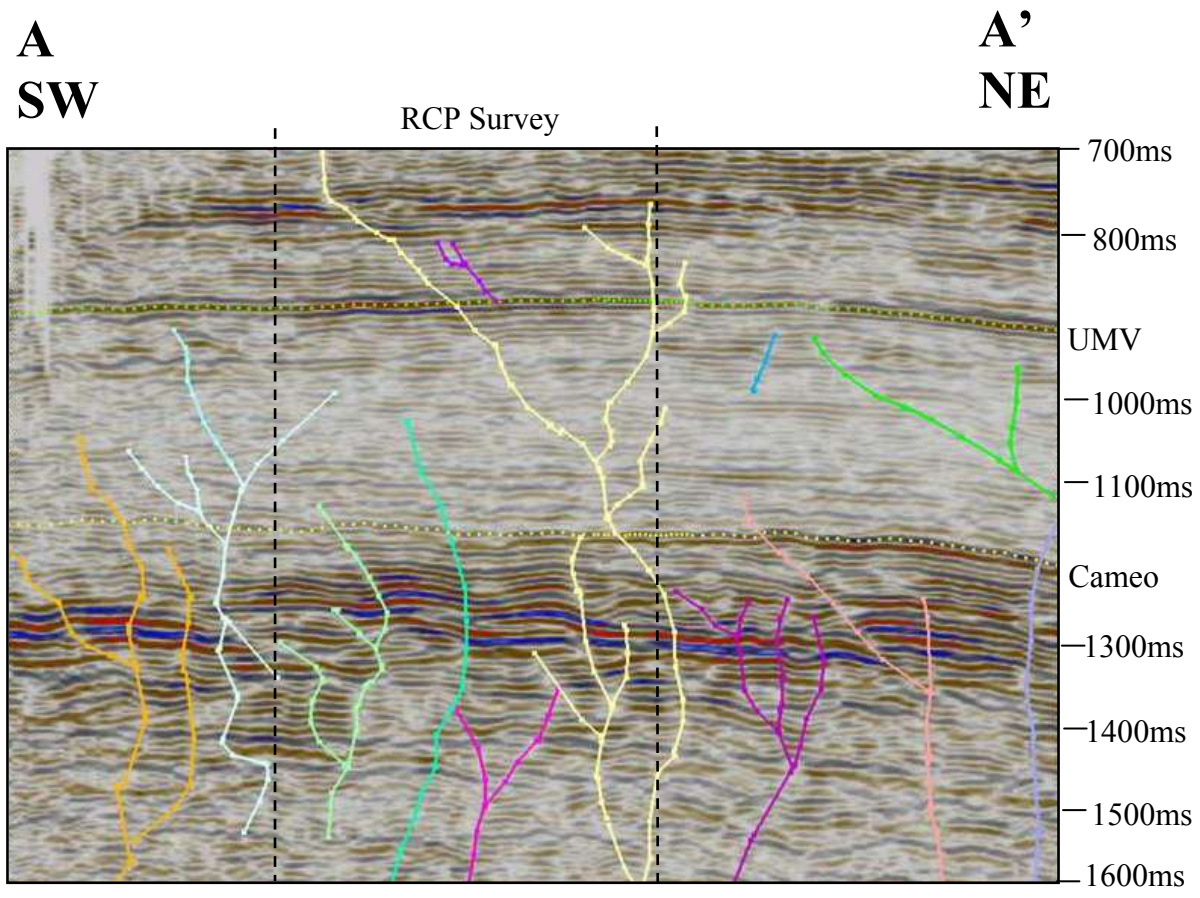


Figure 4.3: Cross section A-A' (Figure 4.2) illustrating fault system interpreted at Rulison. RCP survey area outlined by dotted lines. Vertical exaggeration 20x. Note the upward diverging wrench fault characteristics. See text for discussion.

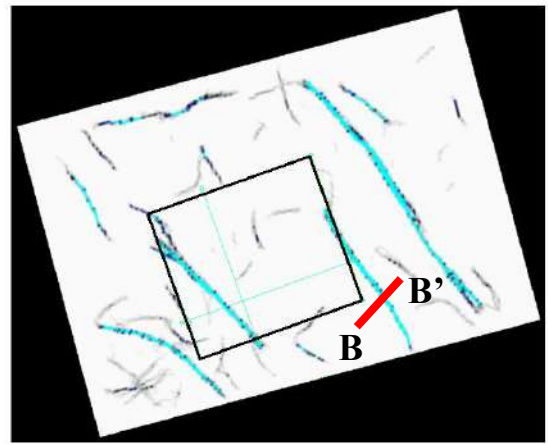
According to P.D Onfro and P. Glagola (1983) there are five criteria for identifying a wrench fault on a single seismic profile. The criteria are:

1. Presence of “palm tree” structures
2. Abrupt dip changes across faults
3. Reversal of or change in fault throw with depth
4. Anomalous thickening or thinning of beds across faults
5. Character change of seismic profile across faults

These criteria are present along the major faults observed in Figure 4.3. These criteria have been observed in more detail across seismic section B-B' in Figure 4.4. This seismic section cuts across the largest left-lateral wrench fault below RCP's study area at Rulison Field. Note how the main wrench fault, traced by the ant tracker in green, diverges immediately above reflector R3, to form the previously discussed “palm tree” structures. Furthermore, note the subtle offset and variance in displacement along the strike zone. The magnitude of displacement varies spatially and is therefore extremely challenging to trace manually. The wrench fault meets all five criteria mentioned above. Abrupt dip changes occur across the fault and can be seen by seismic reflector R1. The wrench fault also experiences reversal and change in fault throw with depth as indicated by seismic reflector R2. Anomalous thickening and thinning of beds is evident across the fault, especially towards the bottom of the fault by reflector R3. Lastly, some

seismic reflectors show character change, such as amplitude differences, across the fault. Most of the character change probably results from sedimentary facies and thickness changes that occur across the fault plane due to the strike-slip movement.

It becomes increasingly more difficult to distinguish between smaller wrench faults and channel features in the mid-upper part of the Williams Fork formation. As the larger faults splay and diverge into smaller fault segments their seismic appearance may look similar to the channel features deposited in this interval. In order to distinguish potential channels from the smaller fault segments it is important to study their pattern. The channels deposited in the reservoir interval are meandering and will have a sinuous pattern, whereas the faults will have more of a linear strike. Figure 4.5 is a time slice of the ant tracker cube through the upper reservoir zone, which consist of complex meander belts deposited in a fluvial system. Two potential channels have been identified and the sinuous pattern is clearly present in the larger channel. The surrounding linear features are considered to be faults given their linear strike and increased vertical extent. The smaller potential channel has been cut by the fault identified in Figure 4.5. The faults interpreted nearby these channel features suggest that the wrench faults may have influenced the distribution of the channel system at Rulison.



B
SW

B'
NE

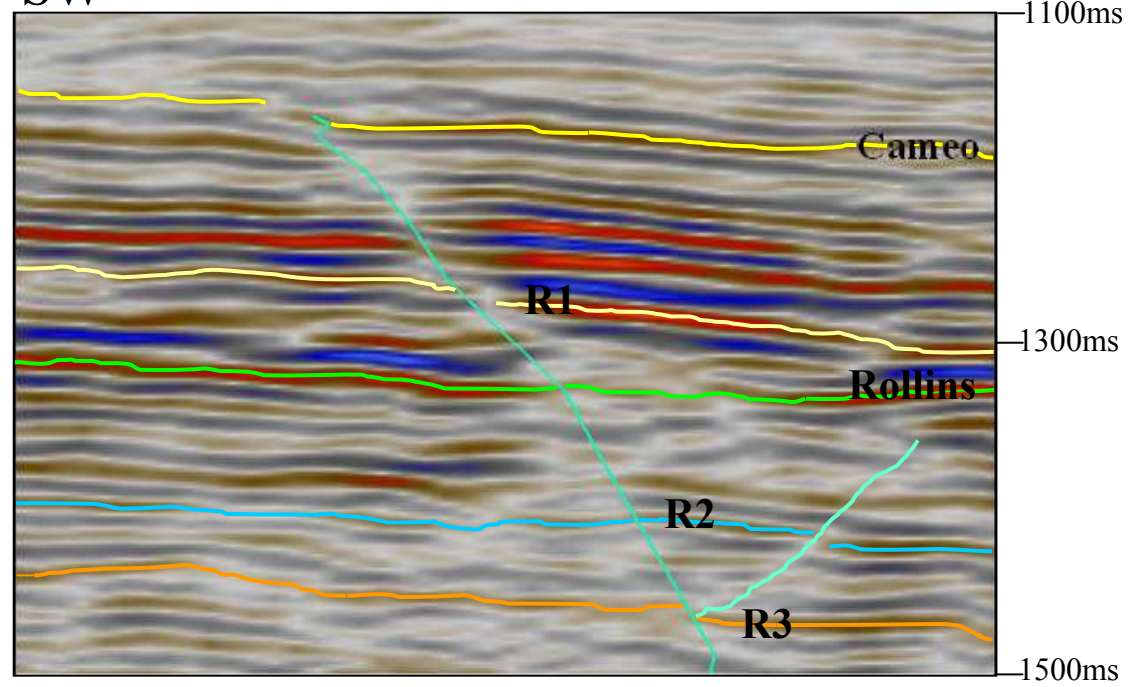


Figure 4.4: Cross section (B-B') of the largest wrench fault observed at RCP's study area in Rulison Field. Green line is the fault traced by the ant tracker software. R1-R3 reflectors illustrate areas which are characteristic of a wrench fault. See text for discussion

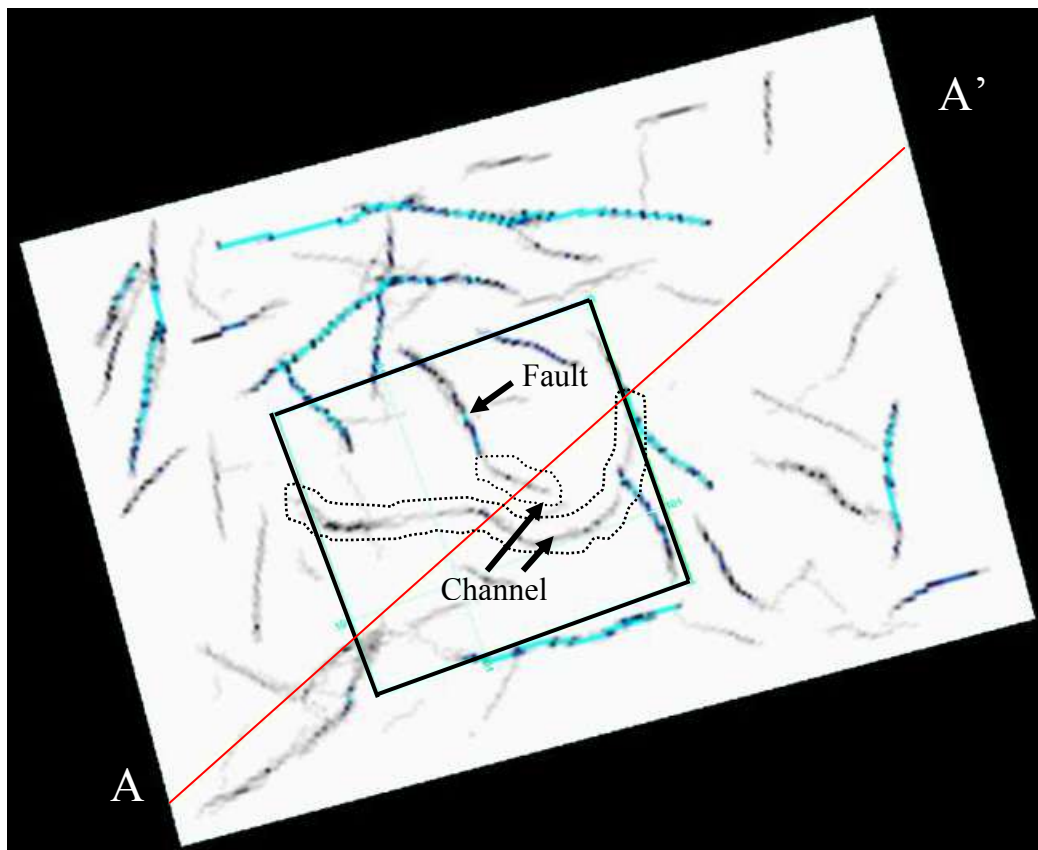


Figure 4.5: Time slice at 922 ms TWT from computed ant track attribute (upper reservoir). Two potential channels identified given their high sinuous pattern and low vertical extent. The surrounding linear features are considered to be faults given their linear strike and larger vertical extent. Red line indicates cross-section A-A' shown in Figure 4.3.

Four major continuous faults, which met the wrench fault criteria, have been identified below the reservoir. The faults are overlain on a Cameo time structure and well top maps which show the faults are parallel to the local structural trends (Figures 4.6 and 4.7). The Cameo horizon was selected because it has high lateral continuity, can be confidently identified and is located towards the lower part of the reservoir interval. The rightmost wrench fault show the largest discontinuities and is considered the largest fault propagating through RCP's study area at Rulison (Figures 4.6 and 4.7). The remaining three faults show less displacement, but are still considered to influence the reservoir above. Other smaller faults exist at this level, but the four shown are the largest most continuous faults below the reservoir.

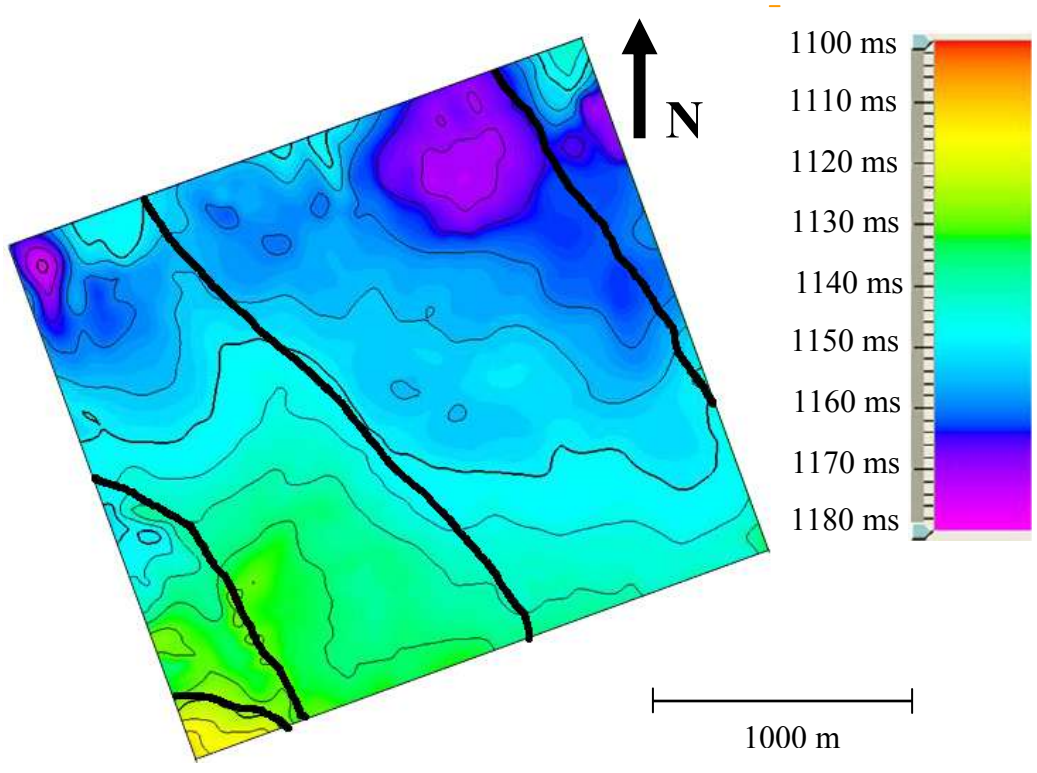


Figure 4.6: RCP study area. Time structure map of the Cameo horizon using P-wave data from RCP's 2003 survey. Black lines represent the largest most continuous faults observed on the Seitel data. Faults parallel structural contours at this depth and will diverge into smaller fault fragments in the main reservoir interval.

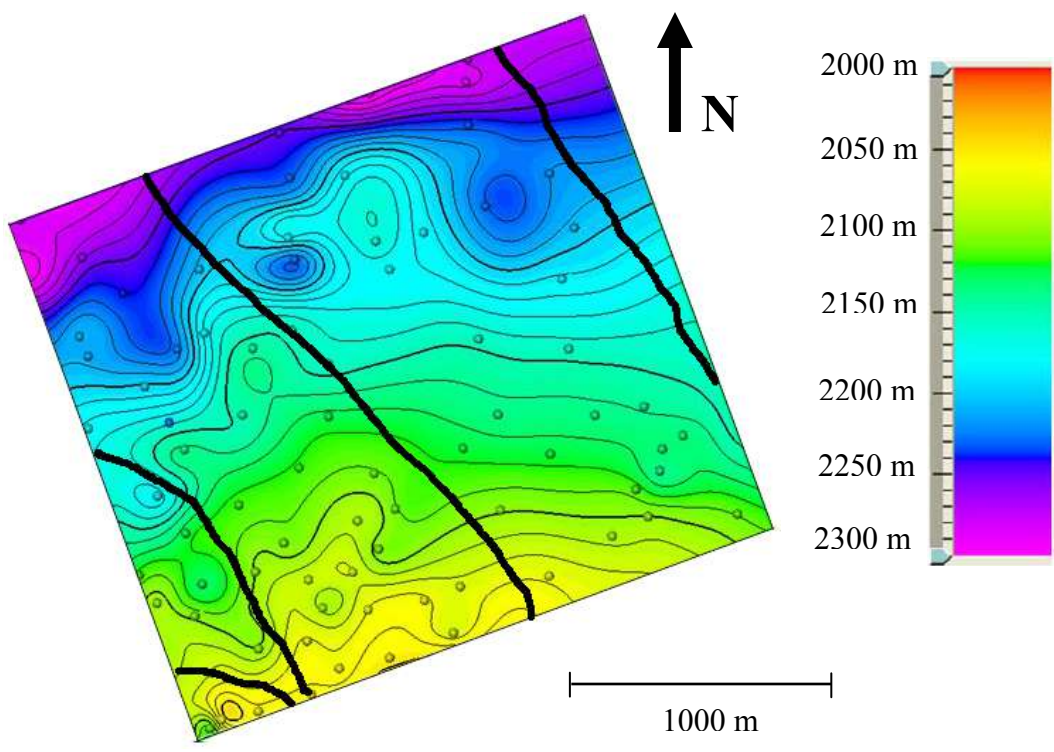


Figure 4.7: RCP study area. Structure map of the Cameo horizon using well top data provided by Williams Production Company. Dots indicate well top data used. Black lines are the largest, most continuous faults observed below the main reservoir using the ant tracker attribute. Faults parallel structural contours at this depth and will diverge into smaller fault segments in the main reservoir.

4.4.1 Fault Splaying in Rulison Field

The stresses induced by the larger more continuous strike slip faults below the reservoir are projected upward into the reservoir, creating numerous smaller fault segments which dominate the reservoir interval. The smaller branching faults are referred to as palm tree structures. Several time slices of the ant tracking cube have been made to understand the splaying of the faults. The splaying of the major faults into smaller less continuous fault segments in the reservoir is illustrated in Figure 4.3 and 4.8. The faults are generated as separate segments and only the larger wrench faults with ample offset will interconnect to form large continuous faults. The reason for the discontinuous character of wrench faults may be related to two major factors: variations in lithology and non-uniformities in the tectonic stress field (Mandl, 1988). Faulting is more prone to develop in competent, brittle beds (e.g. sand bodies), while incompetent beds such as ductile shale layers will accommodate a certain amount of strain by flow, or numerous small slips, before being offset by faulting (Mandl, 1988). Hence, only larger wrench faults with sufficient offset will propagate through the more ductile shale layers to form interconnected fault planes. Smaller wrench faults are restricted to competent brittle areas. Fault observations made on the FMI log, conducted in well RWF 542-20 (center of RCP survey), indicates that the smaller faults in the reservoir interval occur in the more brittle sand prone areas. Variations in the stress field as the basin was uplifted during the Post Laramide tectonism may also have lead to the development of individual segmentary faults.

Note the larger more continuous faults below the main reservoir interval at 1200ms (Figure 4.8a). This interval, referred to as the Cameo Coal zone of the Williams Fork Formation, consists of several coal intervals ranging from 30'-100' in depth (Cumella et al., 1992). Coals, especially mature coals found at Rulison tend to be mechanically very weak (Olson, 2003) and deform in a brittle manner. Hence, only the major faults with sufficient offset will propagate through the coal layers. Smaller wrench faults will disperse and "crumble" the coals, but not form distinct fault surfaces. The permeability of the coals tend to be about 10 times higher than that of sandstone (Olson, 2003) but is highly variable from zone to zone (Murray, 2002). This suggests that the coals are heavily fractured by the dispersing wrench faults.

As we move into the mid reservoir at 1010ms one can clearly see how the more continuous faults have been broken up into smaller fault fragments. The smaller wrench faults predominantly trend in a northwest direction in the reservoir interval, indicating that they are controlled by the larger, continuous faults observed below the reservoir. The previously discussed northeast stepovers are also evident in the middle of the reservoir. The northeast stepovers link the pre-existing faults together, creating fault intersections where enhanced deformation is likely to occur as the faults diverge or converge. Black circles in Figure 4.8 highlight a few fault block corners observed in the Mesaverde Formation. Their relevance to fault

block rotation and generation of natural fractures will be discussed in the following section.

The top of the reservoir, illustrated by a time slice at 890ms shows a significant decrease in faulting (Figure 4.8). The top of the reservoir is dominated by the UMV shale layer who according to Cumella and Ostby (2003) acts as a top seal to the Mesaverde gas reservoir. It appears that no significant faults break through the sealing UMV shale layer. However, faulting is evident again above the reservoir. A reason for this observation can be linked to the ductile properties of shale. Ductile shale tends to “heal” after being displaced by faulting, or even flow rather than fault in the first place, leaving almost no trace of structural movement. A time slice above the reservoir at 820ms is also shown in Figure 4.8. A fault block pattern, similar to the observations made in the reservoir, are present above the reservoir. Even though less structural features are present in the upper part of the Mesaverde formation, it is still believed to be heavily fractured. Williams Production Company is currently evaluating the possibility of storing produced water in the upper part of the Mesaverde Formation (Ostby, 2005). These fault maps should be used in the planning of such an event to better evaluate potential water storage reservoirs. The splaying of the faults in the Mesaverde Formation provide the outlines for the highly fractured zones within the Rulison Field.

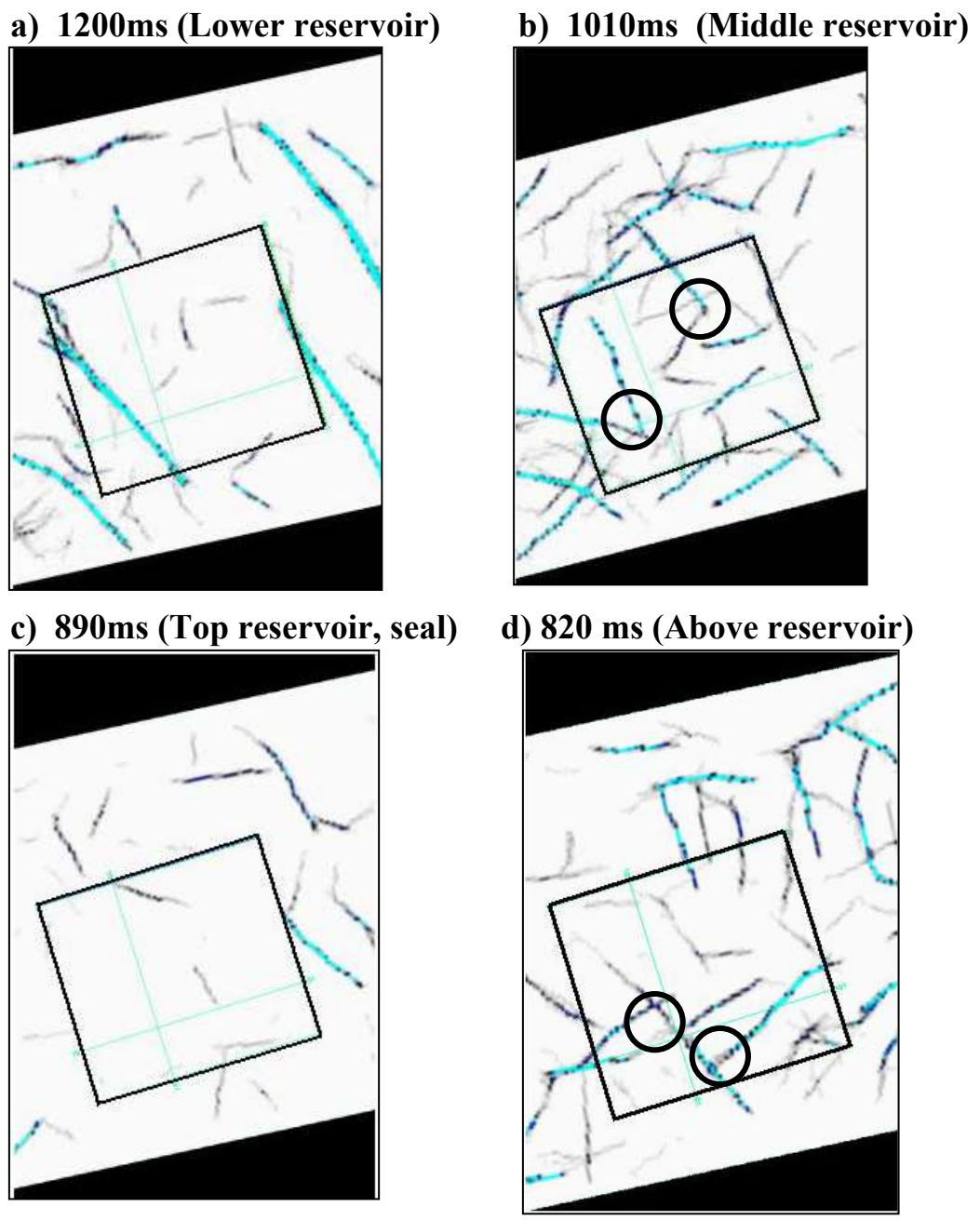


Figure 4.8. Time slices of ant tracking attribute (a-d). RCP study area outlined by black square. Blue lines represents fault geometry and become more complex in and above the main reservoir interval. Circles illustrate fault block corner areas which are more likely to fracture due to increased stress variations.

4.4.2 Fault Blocks and Predicted Fracture Areas at Rulison Field

At Rulison we see divergent/convergent wrench characteristics, and therefore expect to see associated fault block rotation and naturally fractured zones. Evidence suggests that the structural geometry and architecture in the Rulison reservoir is analogous to the previously discussed laboratory models by McClay (2001). A great variety of fault blocks is produced within the Mesaverde reservoir interval. By applying the ant tracker I have identified several of the fault blocks and their characteristics. In the following section I will discuss one fault block in detail.

As mentioned, wrench faults form in response to subsurface horizontal shear movement (Wilcox et al., 1973). As the amount of shear movement on the major northwest wrench faults below the reservoir increases, compressional and tensional stresses are generated in the overlying reservoir. As a result, more palm tree structures develop, and northeast en echelon stepovers occur. The palm tree structures and the en echelon faults combine in the reservoir to produce fault blocks which may undergo block rotation. Instead of moving parallel to the basement wrench fault, the reservoir fault blocks slightly converge (or diverge) causing compressional (or tensional) stresses which are further enhanced (Wilcox et al., 1973). As these fault blocks undergo diverging or converging rotation, natural fractures form in those areas where stress variations are high. The reservoir rock will experience the highest stresses in the vicinity of fault intersections and are considered a primary zone for enhanced natural fracturing.

Consider the following example as to how a fault block developed and how it pertains to natural fracturing (Figure 4.9). The two northwest trending left-lateral wrench faults x and y, are linked to the larger, more continuous wrench faults below the reservoir. The arrows indicate the slip motion on the wrench faults. A principal displacement zone occurred between wrench faults X and Y which led to a zone of wrench deformation. Maximum deformation probably took place during the final White River Uplift (~ 37-45 m.y.) as discussed in the basin stress history section. During this period of wrenching, the northeast stepover fault Z, progressively emerged as an interconnected series of earlier faults and fractures. The northeast stepover eventually linked the larger northwest wrench faults. The intersection of these faults created fault block corner areas which led to the development of the extensional quadrant E and E' (Figure 4.9). The slip motion on the bounding fault segments clearly indicates the extensional corners, and we expect to see associated open fractures in these zones.

The faults in the intersection areas outlines the boundaries where fault block convergence and divergence has taken place. The corner areas of these blocks can be linked to high stress zones, which is indicative of enhanced natural fracturing. The amount of natural fracturing is dependent on the degree these adjacent blocks either converge or diverge under deformation. The fault blocks, on convergence or divergence, will experience higher stresses in the vicinity of fault intersections, i.e. corner areas, and the natural fractures caused by this stress concentration is

believed to be more intense than the natural fractures resulting from subsequent slip on a fault plane. Kim et al. (2004) illustrated how extensional fractures are developed in the extensional quadrants of fault segments. Hence, more extensional fractures are expected to exist in the fault block corner area, such as the extensional quadrant E and E', where fault segments diverge.

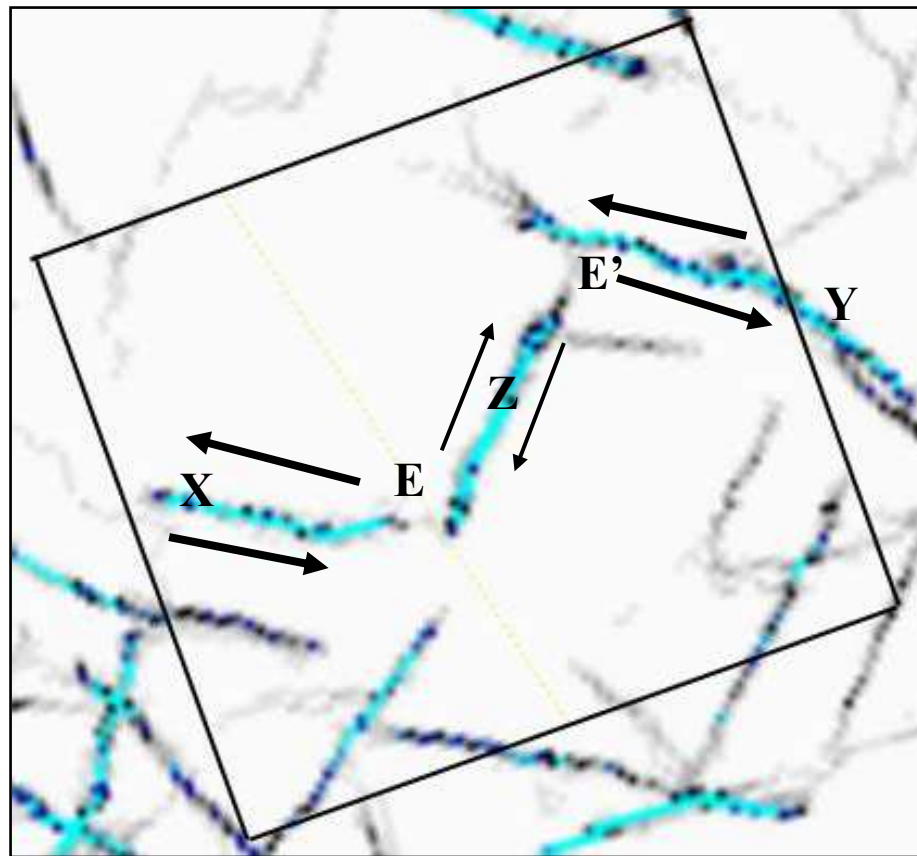


Figure 4.9: Time slice at 1130 ms TWT from computed ant track attribute (mid-lower reservoir). Blue lines represents wrench fault pattern and arrows indicate slip movement. Fault block corners E and E' experience extension and is more likely to fracture due to increased stress variations as fault segments X-Z and Y-Z diverge.

Fault block corners involving divergent wrenching tends to be downthrown, whereas convergent fault block corners tend to be upthrown (Wilcox et al., 1973). This information can be used to characterize an extensional area from a compressional area. A seismic cross section (C-C') through the fault block corner E identified in Figure 4.9, show that its vertical displacement sense changes along strike, which according to Wilcox et al. (1973) is typical of wrench fault systems (Figure 4.11). Note that the fault block bounded by Z tilts to the right. The downthrown side of the fault block correspond to the diverging fault block corner, which also suggests it is in an extensional corner.

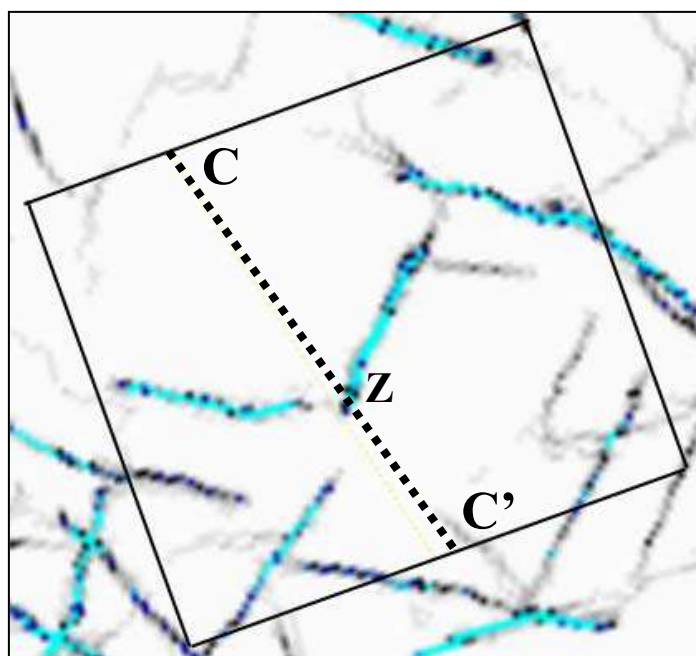


Figure 4.10: Time slice at 1130 ms TWT from computed ant track attribute. Dotted line illustrate seismic cross section through fault block corner shown in Figure 4.11.

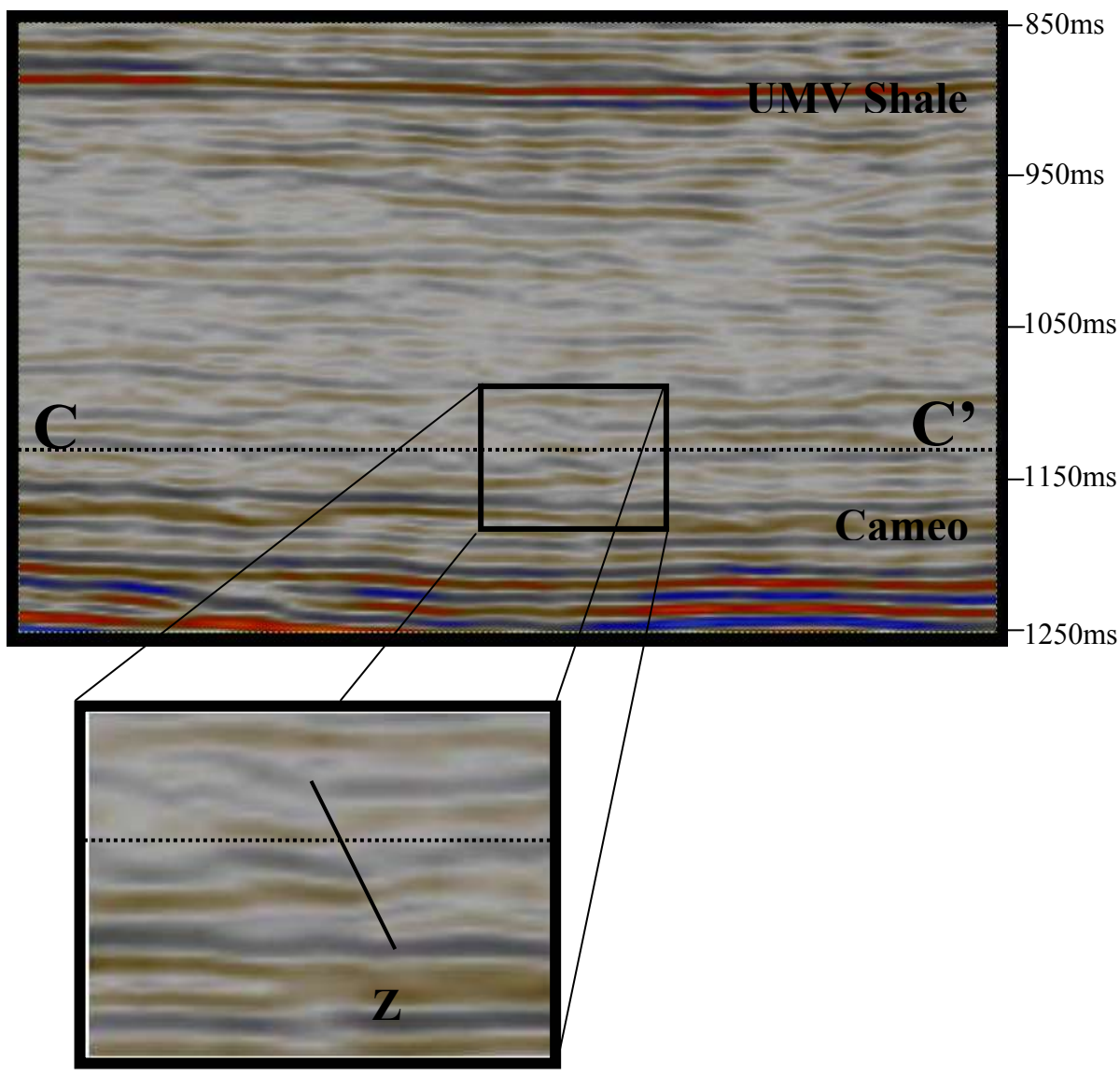


Figure 4.11: Seismic cross section C-C' through fault block corner. Fault block has been enhanced and is bounded by Z. Right side of the fault block has been downthrown and correspond to the extensional quadrant E, seen in Figure 4.9. Dotted line represents time slice at 1300 ms seen in Figure 4.9. Vertical exaggeration 10x.

The extensional fault block corner is expected to contain an increased density of open natural fractures and therefore a well drilled into this corner should experience high production. It is interesting to note that the very best producing well in the field, the Clough 19, intersects this fault block corner. Mahendra Kusuma, a fellow RCP student, studied the time lapse changes between an earlier survey conducted by the DOE in 1996 and RCP's survey in 2003. His preliminary results show an anomaly over the fault block corner (Figure 4.12). Note how the anomaly (red), indicating the gas drainage area, is located in the extensional quadrant corresponding to where we expect an increase in natural fracture density. Preliminary results from time-lapse analysis from the 2003 and 2004 RCP survey also show a similar but smaller anomaly (Keighley, 2005). Time lapse anomalies correspond to fault block corner areas throughout the reservoir interval and another example is given in Figure 4.13. The black circles highlight areas where fault block corners exist, and one can clearly see that time lapse anomalies, produced by Mahendra Kusuma (2005), occur where the smaller wrench faults converge or diverge. Hence, these fault block corner areas produce the interconnected natural fractures necessary for gas production.

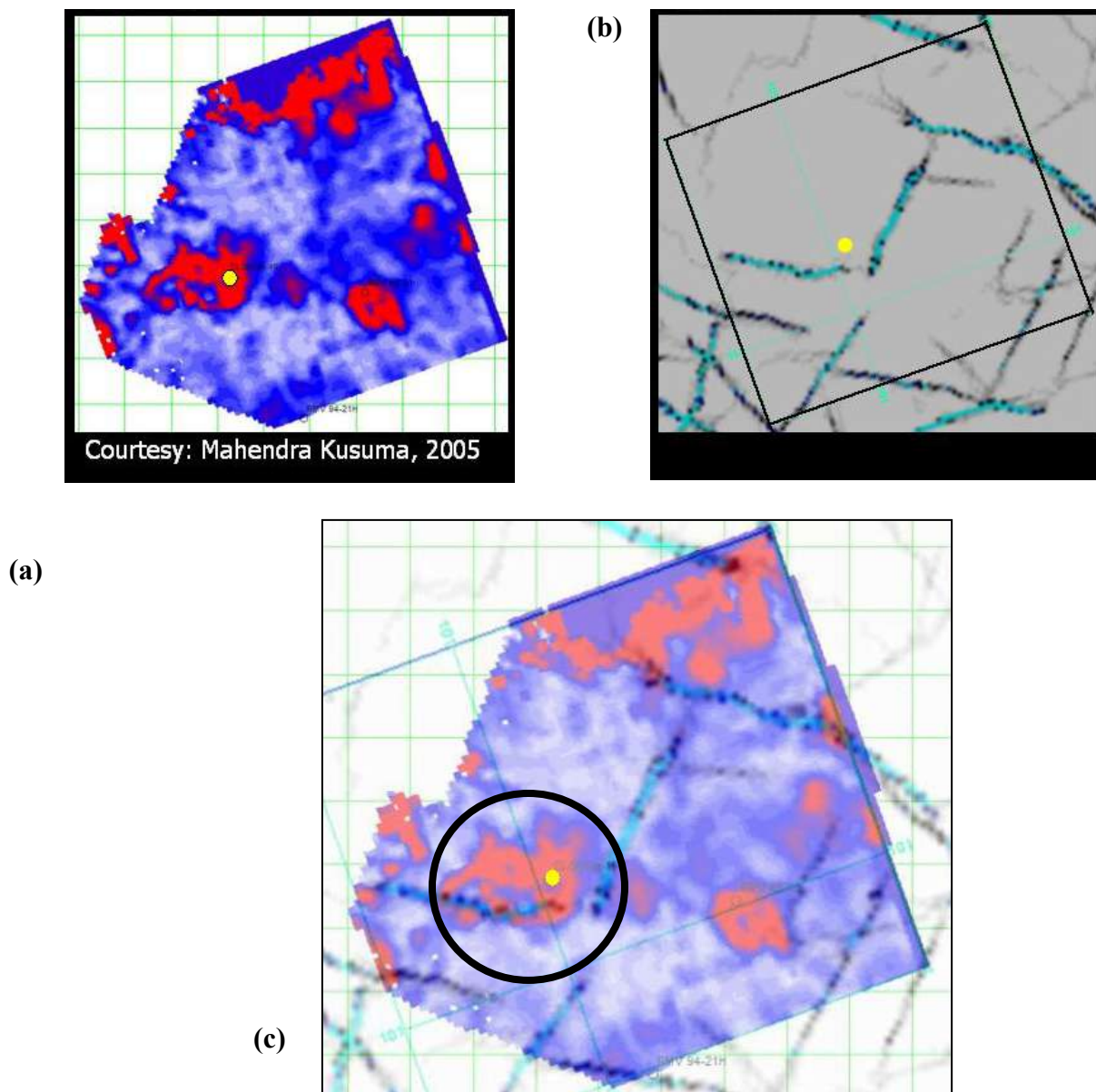


Figure 4.12: a) Preliminary time lapse anomaly between 1996 DOE survey and 2003 RCP survey at 1080 ms RCP time (Approximately 1110 ms Seitel time) (Courtesy Mahendra Kusuma, 2005). Yellow dot represents best producing well in the field, Clough 19. b) Time slice at 1130 ms Seitel time from computed ant track attribute showing fault architecture at this depth. c) Overlay of fault geometry with time lapse anomaly show that drainage area (red) is within extensional quadrant highlighted by black circle.

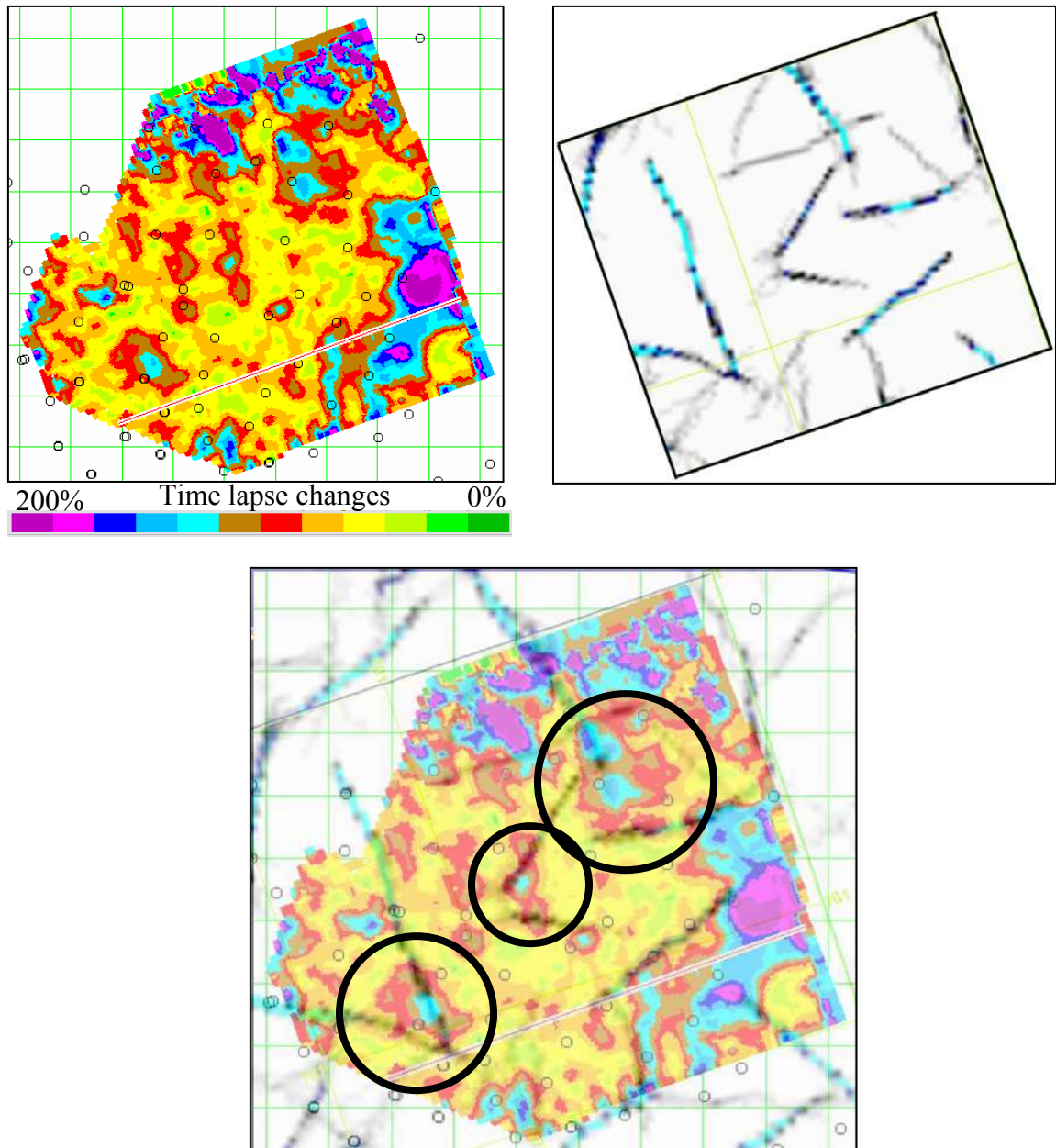


Figure 4.13: a) Preliminary time lapse anomaly between 1996 DOE survey and 2003 RCP survey at 980 ms RCP time. (Courtesy Mahendra Kusuma, 2005). b) Time slice of computed ant track attribute through center of time-lapse anomaly. c) Black circles illustrate areas where time lapse anomalies correspond to fault corners experiencing enhanced natural fracture density.

The formation of individual blocks in the reservoir is supported by pressure data. There is pressure difference between closely spaced wells, especially in an east-west direction (Ostby, 2005). Gas and water cumulative production and rates, carbon dioxide content of the gas, and bottomhole pressure data all indicate that the Divide Creek reservoir, located 13 miles southeast of Rulison, is compartmentalized by a series of fault blocks (Hoak and Klawitter, 1997). A similar scenario exists at Rulison, where the fault blocks have offset the reservoir continuity. The thin reservoir sands at Rulison are easily isolated by the small displacement faults observed in the Mesaverde Formation. The north and northeast trending faults indicated in Figure 4.14 has compartmentalized the upper reservoir in the southeast corner of the RCP study area. Note how the time lapse anomaly in the southeast corner is bounded and do not extend beyond the faults. This observation suggests that the faults are sealing faults and are responsible for reservoir compartmentalization. The sealing properties are probably a result of clay smearing as the wrench faults propagate. Wrench fault characterization in conjunction with time lapse analysis is therefore highly valuable and can be used to predict undrained reservoir sands, isolated by sealing faults.

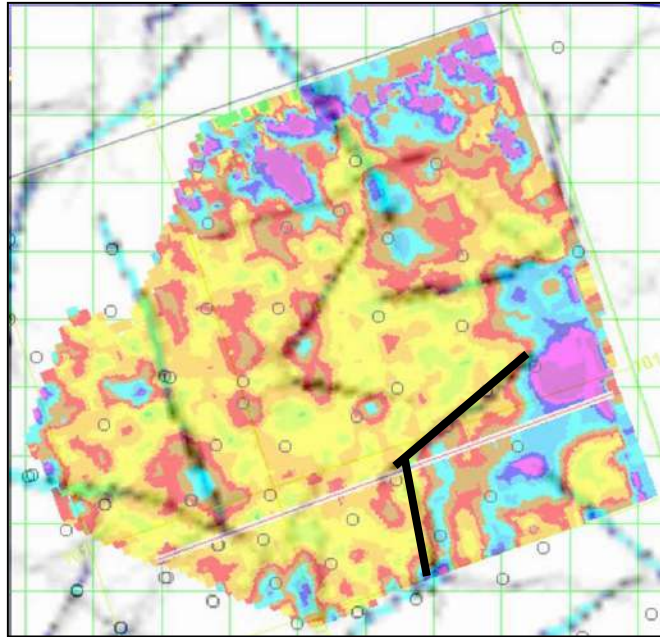


Figure 4.14: The highlighted north and northeast fault are sealing faults, bounding the time lapse anomaly in the southeast corner.

4.5 Correlation of Faults and EUR

Expected Ultimate Recovery (EUR) data was obtained, courtesy of Williams Production Company, to further test my fracture hypothesis. The EUR data include actual and predicted production potential from the Williams Fork fluvial section, the Cameo Coal group, and unperforated producible intervals still behind-pipe at shallower levels. The wells shown in Figure 4.15 has EUR values which range from 0.36 to 3.39 Bcf, with an average of 1.58 Bcf per well. Note that the higher producing wells colored in orange, red and yellow, trend in a northwest direction, parallel to the

basement structural trends below the reservoir in Rulison Field. This relationship suggests a structural control on fractured reservoir production, also observed by Hoak and Klawitter (1997). He also added that the northwest production trend lies perpendicular to the depositional trends, confirming the dominance of structural control on the zones of enhanced production in Rulison field.

Additional observations indicate that the best producing wells are located in the extensional areas between the largest northwest trending wrench faults in the reservoir. A high fracture density is expected in this zone due to the fault block rotation. In addition, the minor northeast stepovers link the wrench faults introducing northeast and northwest fracture sets. The northeast fractures interconnect the dominating west-northwest fractures creating greater permeability and therefore high production. As mentioned, Clough 19 (yellow dot with red circle) is the best producing well in the field and intersects the previously discussed extensional fault block corner as seen in Figure 4.12. In addition, better producing wells are also associated with the fault corner areas discussed in Figure 4.13. The immediate wells surrounding the fault block areas and their EUR values are displayed in Figure 4.16. The better producing wells are located within the fault block corner areas. The EUR values drop as we move away from the corner areas expected to have higher natural fracture density. Well RMV 141-16, marked with an x on Figure 4.16, is an exception as it is a low producer, yet located in a fault block corner area. Completion techniques

and net sand thickness may be other factors which have influenced this well's performance.

Williams Production company currently operates with an east-west drainage ellipse for their wells. Given the structural complexity at Rulison, it is likely that the drainage ellipses vary according to the fault geometry. Hence, structural interpretation should be taken into account when frac jobs are designed for future wells.

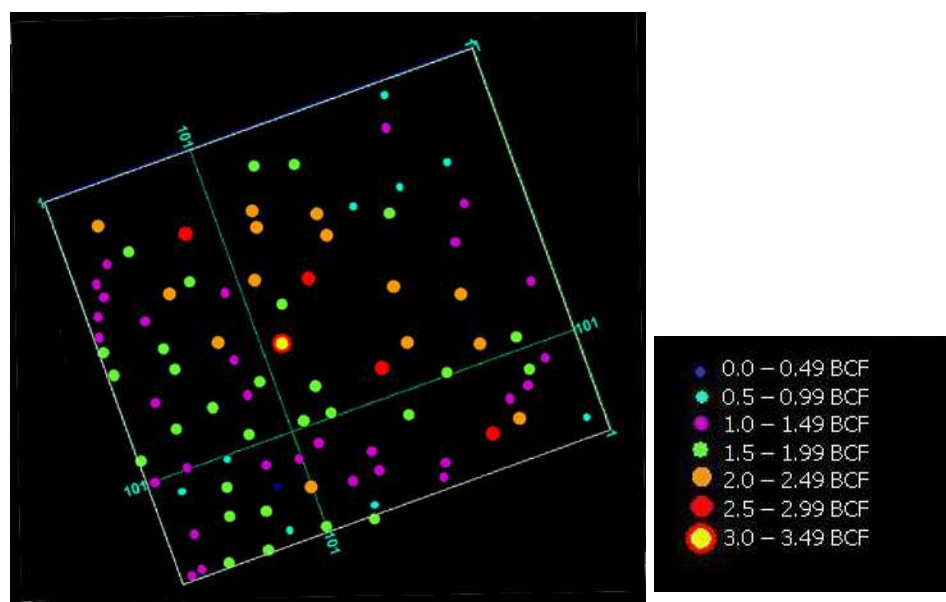


Figure 4.15: Estimated Ultimate Recovery (EUR) map for all the wells in the RCP study area. Note that best producing wells trend in a northwest direction, suggesting a link to the structural trends below the reservoir.

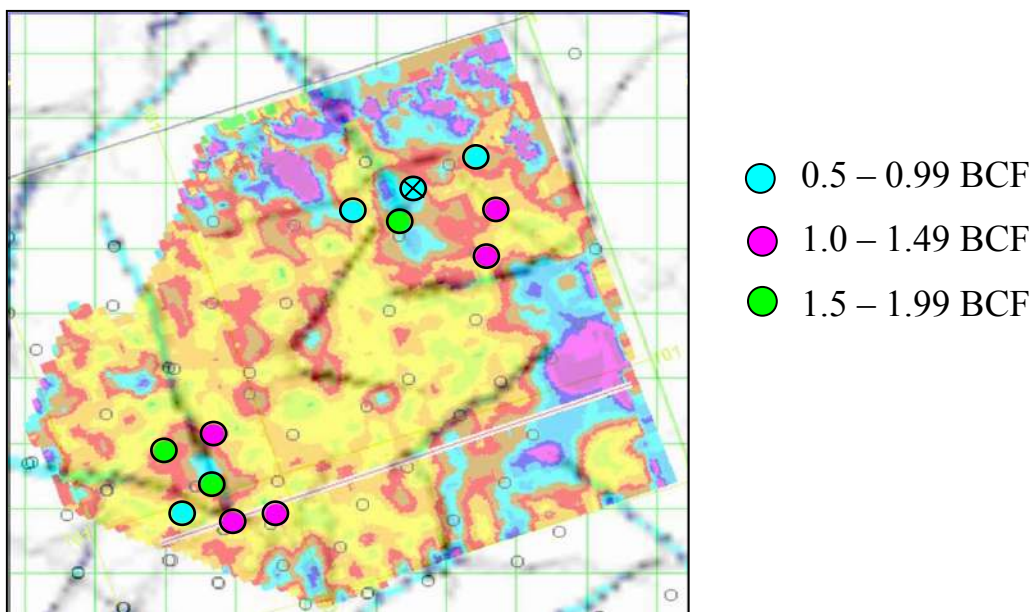


Figure 4.16: Better EUR wells are associated with fault block corner areas and corresponding time lapse anomalies. EUR values decrease away from fault block corner areas.

4.6 Conclusions

The ant tracking software provides a significantly improved image of the subtle faults in the reservoir interval at Rulison Field. My interpretation suggests that the reservoir is dominated by a wrench fault system, a system characterized by larger, continuous, faults below the reservoir diverging into smaller fault segments in the reservoir interval. Wrench fault tectonics and its structural architecture is strongly linked to areas of enhanced natural fracturing at Rulison. The natural fracture zones are associated with fault trends and areas of deformation such as structural corners and fault

intersections. Higher permeabilities and increased production is expected in the fault block corner areas, which experience larger stress variations. This observation is corroborated by correlation of preliminary time lapse results by Mahendra Kusuma and Donny Keighley and EUR data from Williams Production Company. Experimental laboratory results provided templates for the seismic interpretation of the complex wrench fault system at Rulison (McClay, 2001). In the next chapter, shear wave splitting analysis will be used to verify areas of higher fracture density predicted from the fault interpretation.

CHAPTER 5

SHEAR SPLITTING PARAMETERS AT RULISON

5.1 Introduction

The presence of natural fractures dramatically improves production rates in the tight gas formations at Rulison Field. Establishing the presence and specific location of these natural fractures is essential to optimize production. Seismic anisotropy, and in particular shear wave anisotropy, provides a powerful tool for analyzing the fracture properties within reservoirs (Martin and Davis, 1987; Lewis et al., 1991). Evidence of anisotropy in the fractured reservoir at Rulison has the potential to be a powerful interpretation tool for characterizing the intensity and orientation of these fractures. In this chapter, the shear wave splitting parameters will be analyzed to identify areas of enhanced natural fracturing.

5.2 Shear Wave Anisotropy Properties

Anisotropy, defined as “variation in a physical property with direction” (Tatham and McCormack, 1991), provides a practical means for analyzing fracture properties. Shear wave anisotropy is especially important for delineating natural fractures by exploiting the unique characteristics of shear waves. Shear wave propagation is controlled largely by the rigidity of the rock mass. In the presence of an aligned fractured media an incident

shear wave will split into two orthogonal waves which will travel at different velocities depending on the fracture properties (Figure 5.1). The shear wave that is polarized perpendicular to the cracks (S_{\perp}) will intersect more fracture planes and sample a less rigid medium and therefore travel at a lower velocity. The shear wave that is polarized parallel to the cracks (S_{\parallel}) intersects less fracture planes and samples a more rigid portion of the medium and will therefore travel faster. For the remainder of this chapter S_{\parallel} and S_{\perp} will be referred to as S1 (fast) and S2 (slow), respectively. The amount of splitting (time difference between the two S-waves) is proportional to the fracture density. The fracture density can be approximated by the shear splitting parameter ($\gamma^{(s)}$), which is the fractional difference in velocity of the fast (V_{s1}) and slow (V_{s2}) shear waves. The shear splitting parameter ($\gamma^{(s)}$) is estimated in the following way:

$$\gamma^{(s)} = \frac{\Delta t_{s2} - \Delta t_{s1}}{\Delta t_{s1}} \quad (5.1)$$

where Δt_{s1} is the time difference between two seismic horizons in the (S1) fast shear wave data and Δt_{s2} is the time difference between the corresponding horizons in the (S2) slow shear wave volume. The shear wave splitting time measurement is an average, weighted by thickness of the shear splitting parameter over the interval bounded by the selected horizons. If the chosen horizons are spaced far apart in time and depth and not all of the units within the interval are anisotropic, then the method will severely

underestimate the shear splitting parameter (Thomsen, 1988). According to Reasnor (2001) this is a fundamental reason why Thomsen (1988) referred to shear wave time analysis as a low vertical resolution anisotropy tool.

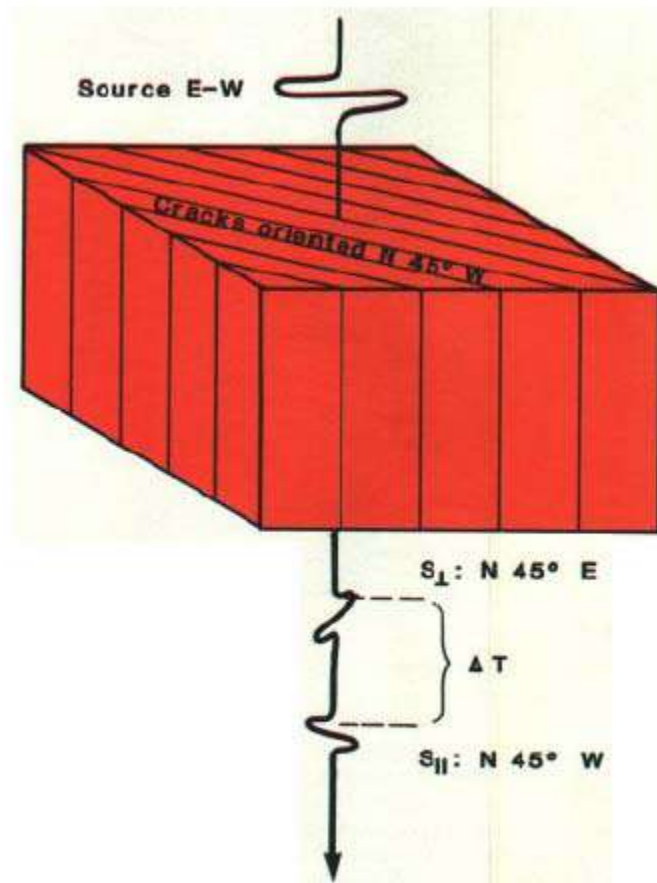


Figure 5.1: Schematic illustrating shear wave propagation and splitting in a unidirectional fractured medium. When encountering the fractures the incident shear wave will split into two waves with polarization of the faster (S_{II}) wave parallel to the fracture planes and the slow (S_{\perp}) wave will propagate perpendicular to the fracture planes. (From Martin and Davis, 1987).

Seismic anisotropy can also be estimated by analyzing amplitude differences over the same interval between the fast and slow shear wave volumes. Mueller (1992) identified the lateral variability in fracture zones with great accuracy by studying the shear wave amplitude differences caused by fracturing in the Austin chalk of central Texas. The fracture zones were characterized by a low reflectivity on the slow S2 data and high reflectivity on the fast S1 data.

The anisotropy can be estimated from amplitudes using the following relation (Thomsen, 1988):

$$R_{S1} - R_{S2} = \frac{1}{2} \Delta\gamma \quad (5.2)$$

where γ_1 and γ_2 are the shear wave splitting above and below the reflecting horizons, respectively. Thomsen (1988), concluded that shear wave amplitude analysis is a higher vertical resolution tool, than shear wave time analysis. Reflectivities are directly proportional to seismic amplitudes. Hence, seismic amplitudes can be scaled to the magnitude of the reflection coefficients and the shear splitting parameter can be obtained from one layer to the next (Reasnor, 2001). In the next sections, time splitting parameters and amplitude differences on the shear wave data will be evaluated to identify zones of higher fracture density at Rulison Field.

5.3 Shear Wave Splitting Parameters at Rulison

Kendall (1996) observed strong evidence of fracturing from variations in amplitude strength between the fast and slow shear wave components in a tight gas reservoir in south central Wyoming. He found that shear wave amplitude anomalies coincided with production anomalies that were an order of magnitude more productive than production in the surrounding regions. Rulison Field is analogous to the field studied by Kendall (1996). In this Chapter, the Rulison Field shear wave data will be evaluated for such amplitude anomalies, including time splitting analysis, to characterize zones of higher fracture density.

Observations made by Burke (2005) on the FMI logs and stress modeling conducted by Higgins (2005) indicate that the thin more brittle sandstones beds are more likely to fracture than the surrounding more ductile shale layers. One can therefore assume that the shale is isotropic and that shear splitting parameters observed are linked to fractures in the discontinuous, lenticular, sand bodies. As mentioned earlier, these fluvial sand bodies may be stacked on top of each other in intervals ranging from 20 to 60 feet (Kuuskraa et al., 1997). Time splitting analysis over the reservoir interval will give an average measurement of the anisotropy caused by the fractures in the stacked, lenticular, sand bodies. Amplitude analysis estimate anisotropy at a finer scale allowing the interpreter to target specific zones in the reservoir.

Evidence of anisotropy in the fractured reservoir at Rulison is demonstrated by comparing the fast (S1) with the slow (S2) seismic section across inline 70 (Figure 5.2). Figure 5.3 compares reflection behavior between the fast (S1) and slow (S2) data set and both amplitude variations and time splitting is apparent. Variations in amplitude and time splitting between the two data sets are indicative of anisotropy. Lateral amplitude variations are observed throughout the reservoir interval, particularly within the black rectangle. In addition, a larger time sag is observed on the Cameo horizon below the rectangle in the slow (S2) volume. The amplitude variations and time splitting observed between the two data sets can be linked to areas of increased aligned fracture density in the reservoir sands. Both methods will be explored further in the following sections. The shear wave data has been rotated to a common, time-invariant, angle of N 45° W, based on VSP data.

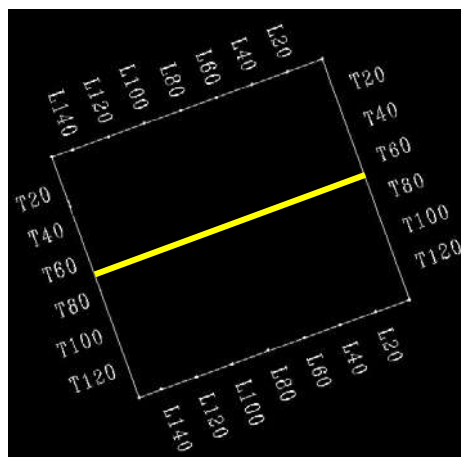


Figure 5.2: Yellow line represents inline 70 across RCP survey area. Comparison of seismic sections (S1 and S2) across inline 70 are shown in Figure 5.3.

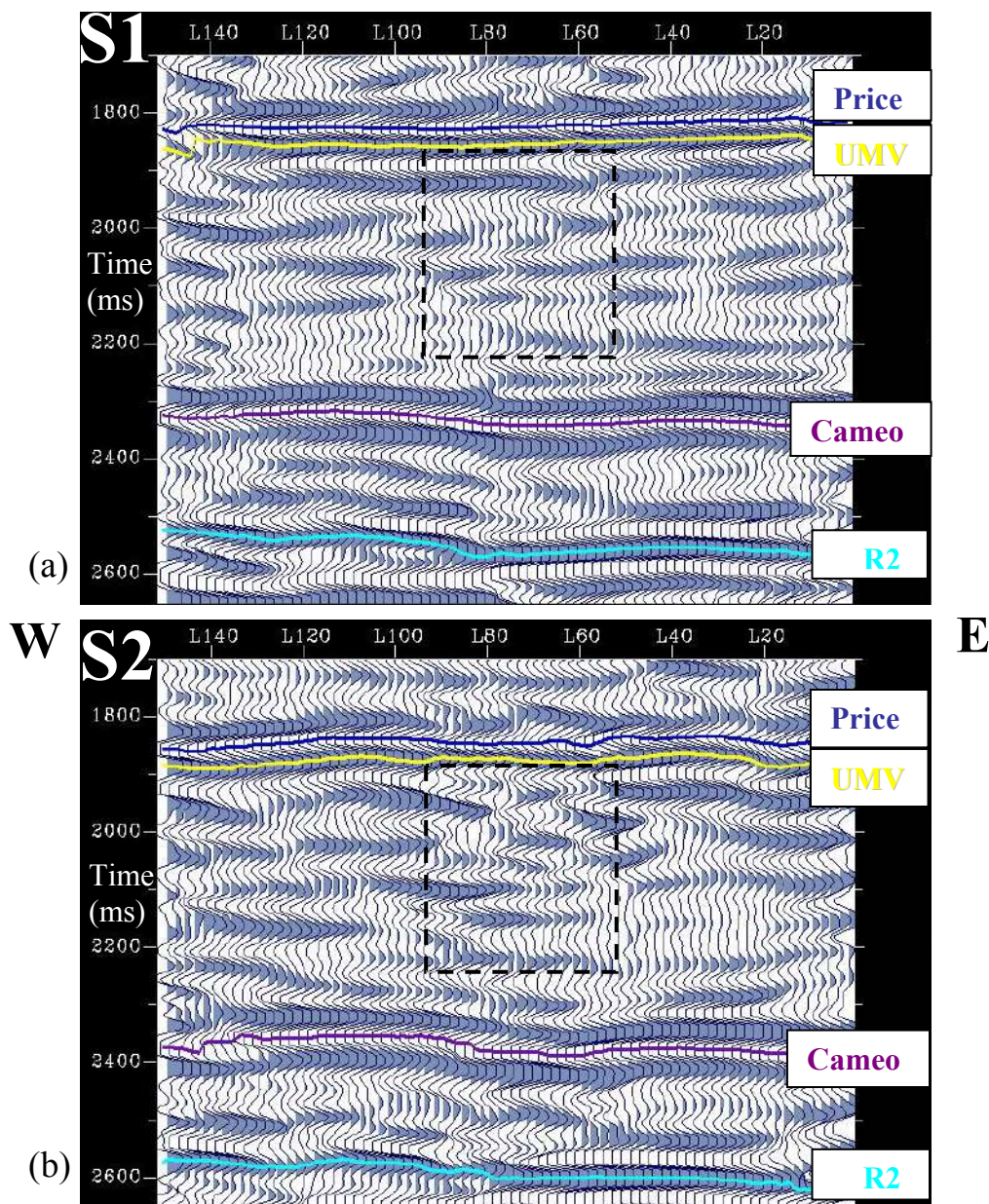


Figure 5.3: Amplitude and time splitting between S1 (a) and S2 (b) data sets along inline 70 are indicative of anisotropy. Shear wave splitting parameters between the two lines can be linked to areas of enhanced natural fracturing. Black rectangle outlines area of particularly high amplitude variations. A larger time lag is observed in the S2 volume below the black rectangle on the Cameo horizon, also indicative of anisotropy.

5.3.1 Time Splitting Analysis at Rulison

Three seismic horizons (Price Coal, Cameo and R2) were selected for the time splitting analysis (See figure 5.3 for reference on horizons). They were selected because they have high lateral continuity and could be confidently identified throughout the RCP study area. The Price Coal horizon is a half a wavelength above the previously discussed UMV horizon which is thought to be the top of the reservoir due to its sealing characteristics. The Cameo horizon is a coal layer in the lower part of the reservoir which can easily be correlated across the field. The R2 horizon is the deepest horizon which has been correlated across the field and is considered the base of the reservoir.

Applying Thomsen's (1988) time splitting analysis to the Rulison shear wave data produced shear wave splitting ranging from 0-21 % between the Price Coal – Cameo horizon and Price Coal – R2 horizon (Figure 5.4 and Figure 5.5, respectively). In the southwest corner of Figure 5.4, anisotropy values are extraordinary high and are linked to edge effects. As a result these values are considered unreliable. The anisotropy ranges from 0-8% in the higher fold areas in the central region of the survey. When the shear wave splitting is high and positive, the polarization directions are oriented in a uniform direction, indicating a dominate single aligned fracture set parallel to the pre-determined fast direction of N 45° W. A few areas experience “negative anisotropy,” recognized by black flecks on the time splitting maps, implying that the fast shear azimuth is perpendicular or

oblique to the rotation angle suggesting the presence of a northeast fracture trend. The data have not been rotated to the local orientations in those areas. Positive anisotropy anomalies dominate the reservoir interval indicating that northwest fractures are dominant.

In general, the same anisotropy anomalies are observed in both time splitting maps (Figure 5.4 and 5.5). However, the anomalies tend to have less magnitude between the Price Coal - R2 interval compared to the Price Coal - Cameo interval. This suggests that the interval above the Cameo is more anisotropic due to fracturing than below the Cameo horizon. This observation corroborates fracture trends predicted from the fault interpretation discussed in Chapter 4. In addition, the high anisotropy values, observed on both time splitting maps, generally trend in a northwest/north-northwest direction, suggesting that the anisotropy is linked to the dominantly northwest trending faults below the reservoir.

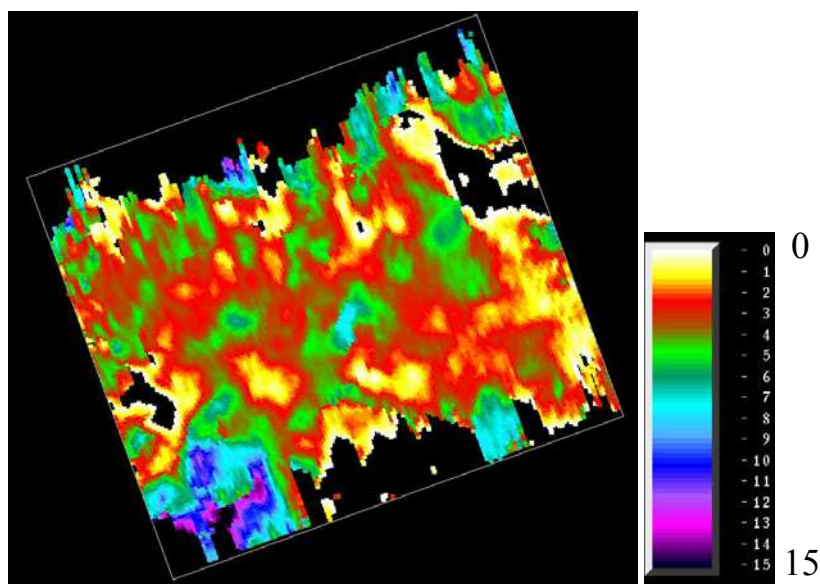


Figure 5.4: Time splitting analysis (average anisotropy) calculated between Price Coal and Cameo horizon. Anisotropy ranges from 0-8% in high fold areas. High anisotropy observed in the southwest corner and along the survey boundaries are caused by edge effects in the S2 volume.

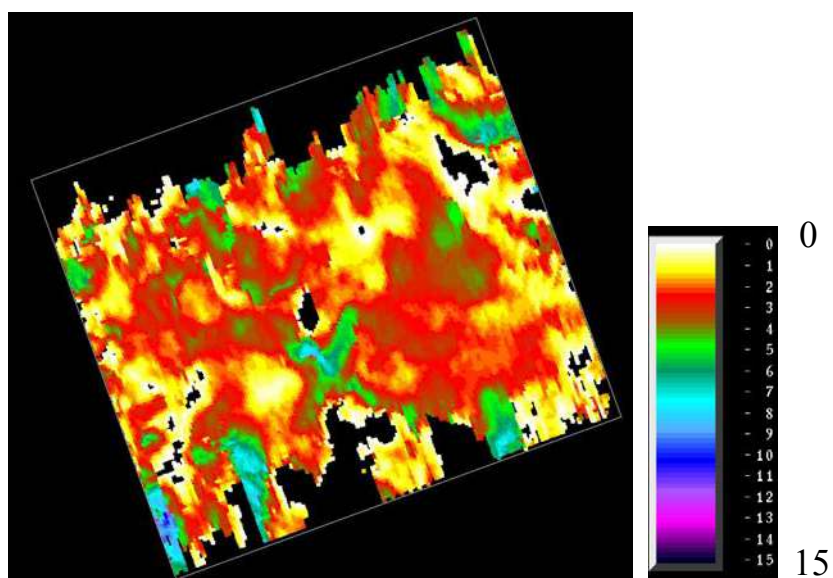


Figure 5.5: Time splitting (average anisotropy) analysis between Price Coal and R2 horizon. Similar anisotropy anomalies, but with less magnitude observed at this interval compared to the Price Coal-Cameo interval in Figure 5.4.

Thomsen (1988) stated that the use of travel time analysis is a stable measurement of average anisotropy over large depth intervals, but of low vertical resolution. As mentioned, the small lenticular sand bodies at Rulison are highly discontinuous with a vertical stacked thickness of 20 to 60 feet (Kuuskraa et al., 1997) Anisotropy caused by the sand bodies is not accounted for by the traveltimes differences between S1 and S2 over the larger reservoir interval. In order to characterize the reservoir at a finer scale, amplitude analysis between split wave data is necessary. Amplitude analysis were conducted for detailed reservoir characterization of these thin discontinuous, lenticular sand bodies.

5.3.2 Amplitude Analysis at Rulison

By comparing amplitude information in the stacked sections of fast (S1) and slow (S2) shear wave data, variations in lateral fracture intensity can be measured at Rulison Field. To further investigate the amplitude variations at Rulison Field, the reservoir interval was divided up into series of 50 ms windows hung from the Price Coal horizon and the Cameo horizon. Figure 5.6 shows the amplitude variations between S1 and S2 over a 50 ms window hung from the Cameo horizon (lower reservoir). As mentioned earlier, this interval is characterized by brittle, heavily fractured coal layers intersected by a few continuous northwest trending faults. The amplitude analysis over this interval show very little anisotropy with values

predominantly in the 0% range, indicated by the turquoise color (Figure 5.6). Coal tends to form small orthogonal cleats (Murray, 2002) and therefore appear isotropic because there is no dominant fracture direction. Martin Terrell (2004) illustrated how orthogonal fracture sets appear isotropic, and therefore do not create an anisotropic seismic response. Even though the coal layers are heavily fractured the shear wave splitting analysis produced anisotropy in the 0% range due to the small fractures and their orthogonal orientation. Some large anisotropy variations are present close to the edges of the survey and are assumed to be associated with edge effects, or sand bodies with a predominant fracture direction. A negative anomaly trending northwest can be observed in the southeast corner of Figure 5.6 and is potentially linked to the previously discussed northwest trending fault at this level. Similar amplitude analysis were conducted throughout the reservoir interval and results show that the anomalies created from high fractured sand bodies vary spatially through the reservoir.

For comparison, a similar amplitude analysis was carried out over a 50 ms window towards the top of the reservoir. Figure 5.7 illustrates the amplitude measured shear splitting between S1 and S2 at 50-100 ms below the Price Coal horizon (top of the reservoir). One would expect to observe fracturing at this interval due to the abundance of palm tree structures, fault intersections and fault block rotation. Large amplitude variations are present suggesting that this interval indeed is heavily fractured. The upper Williams Fork is characterized by less mudrock and thicker, more laterally continuous

sand bodies (Pranter, 2003). More abrupt amplitude variations are observed in the upper part of the reservoir compared to the lower reservoir. The abrupt amplitude variations present in Figure 5.7 are therefore linked to areas of increased directional fracture density. Positive red colored areas indicate zones where the natural azimuthal polarization direction of the fast shear wave component is parallel with the N 45° W rotation angle, implying a predominant northwest fracture direction. The negative purple areas indicate that the fast shear azimuth is perpendicular to the rotation angle. Hence, those areas may correspond to areas of a dominant northeast fracture direction. The large amplitude variations seen throughout the reservoir interval above the Cameo horizon suggest that the sand bodies are heavily fractured and that different fracture directions dominate throughout the reservoir.

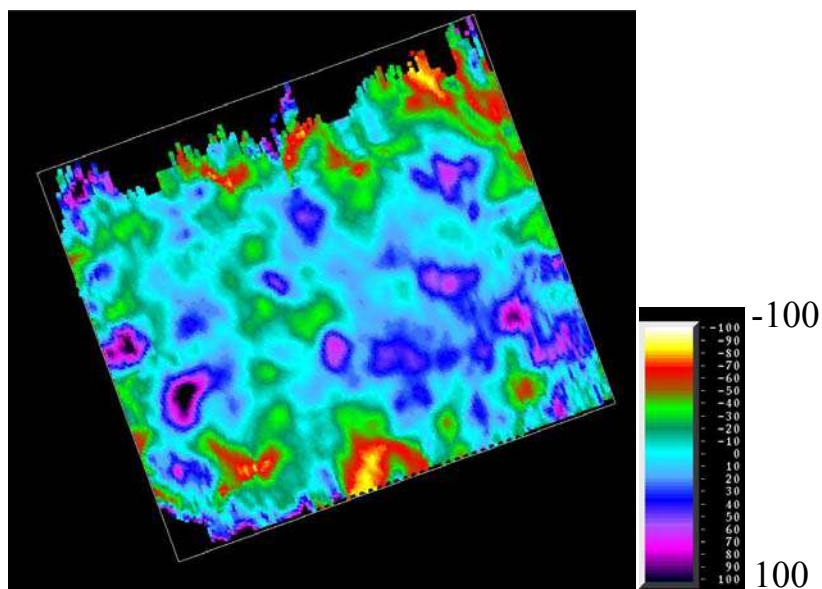


Figure 5.6: Shear wave splitting parameter map calculated from S1-S2 amplitudes at a 50 ms window hung from the Cameo horizon (lower reservoir). Note predominantly low anisotropy at this level caused by small orthogonal fracture sets, creating an “isotropic medium” in the coal layers.

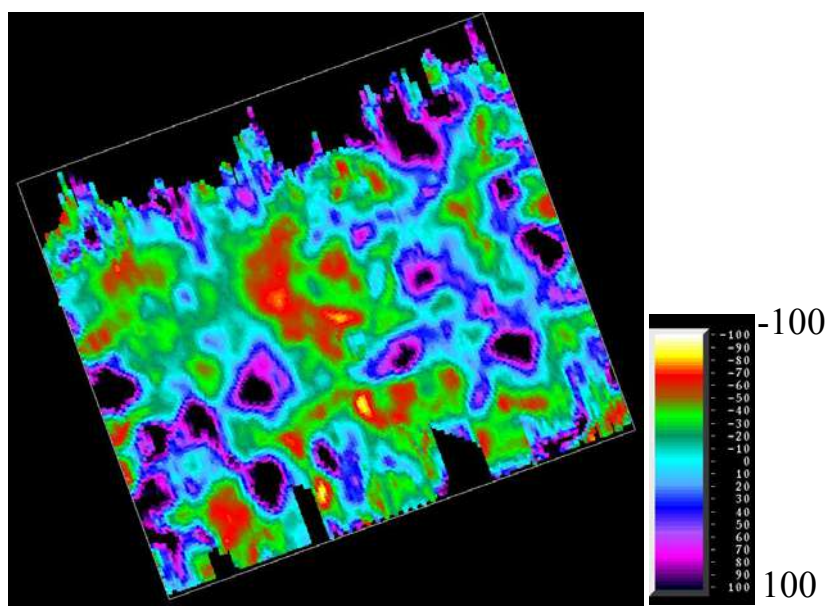


Figure 5.7: Shear wave splitting parameter map calculated from S1-S2 amplitudes at 50-100 ms below the Price Coal horizon (top of reservoir). Note numerous high amplitude variations indicative of directional fracturing.

Since shear wave propagation is mainly by the rigidity of the rock mass, shear waves are especially useful for characterizing fractured reservoirs under different stress conditions (Davis, 2002). The fluvial sand bodies at Rulison are overpressured and it is thought that the fractures remain open in the sand reservoirs due to the overpressured gas saturation. It is therefore reasonable to assume that the anomalies caused by large amplitude variations between the S1 and S2 volume are associated with the overpressured, fractured gas saturated sand bodies. Amplitude analysis can therefore be used to identify missed overpressured zones.

Now the question remains, “Can amplitude analysis confirm areas of higher fracture density predicted from the fault interpretation at a finer scale?” Let us consider the fault block pattern which was discussed in detail in Chapter 4. Recall how we would expect the northeast stepover in figure 4.9 to introduce a northeast fracture set. In addition, we would expect to see an enhanced fracture density in the extensional quadrants E and E'. A 50 ms window amplitude analysis between S1 and S2 volume was generated over the fault pattern and the amplitude variations are shown in figure 5.8b. Note the very large negative anomaly, indicating a predominant northeast fracture direction, which correlate with the northeast stepover. It is possible that the anisotropy anomaly is responding to shear fractures induced by the northeast stepover. An overlay can be seen in Figure 5.9 and it is clear that the northeast fracture anomaly from the amplitude analysis correspond to the northeast stepover observed in the ant tracking cube. In addition, the fault

block corner where we would expect the most intense fracturing to occur correlates with a large negative amplitude anomaly, indicating that the extensional fault quadrant is dominated by an abundant northeast fracture trend.

As mentioned, the shear wave data has been rotated to a common, time-invariant angle of N 45° W. Work on the dipole sonic log by Burke (2005) suggests that northeast and northwest fractures dominate the reservoir. Regardless of rotation angle, the validity of the amplitude measured shear splitting is not compromised, because the rotation process maximizes the difference between S1 and S2 wave amplitudes (Reasnor, 2001). This ensures that areas of large shear splitting will remain large when rotation angle is changed. However, the magnitude of these areas in relation to one another may change and the error in the calculated shear splitting value will be minimized with proper rotation. Therefore, a time variant Alford rotation may greatly improve data quality and reduce the error in estimating the shear splitting value of the reservoir interval.

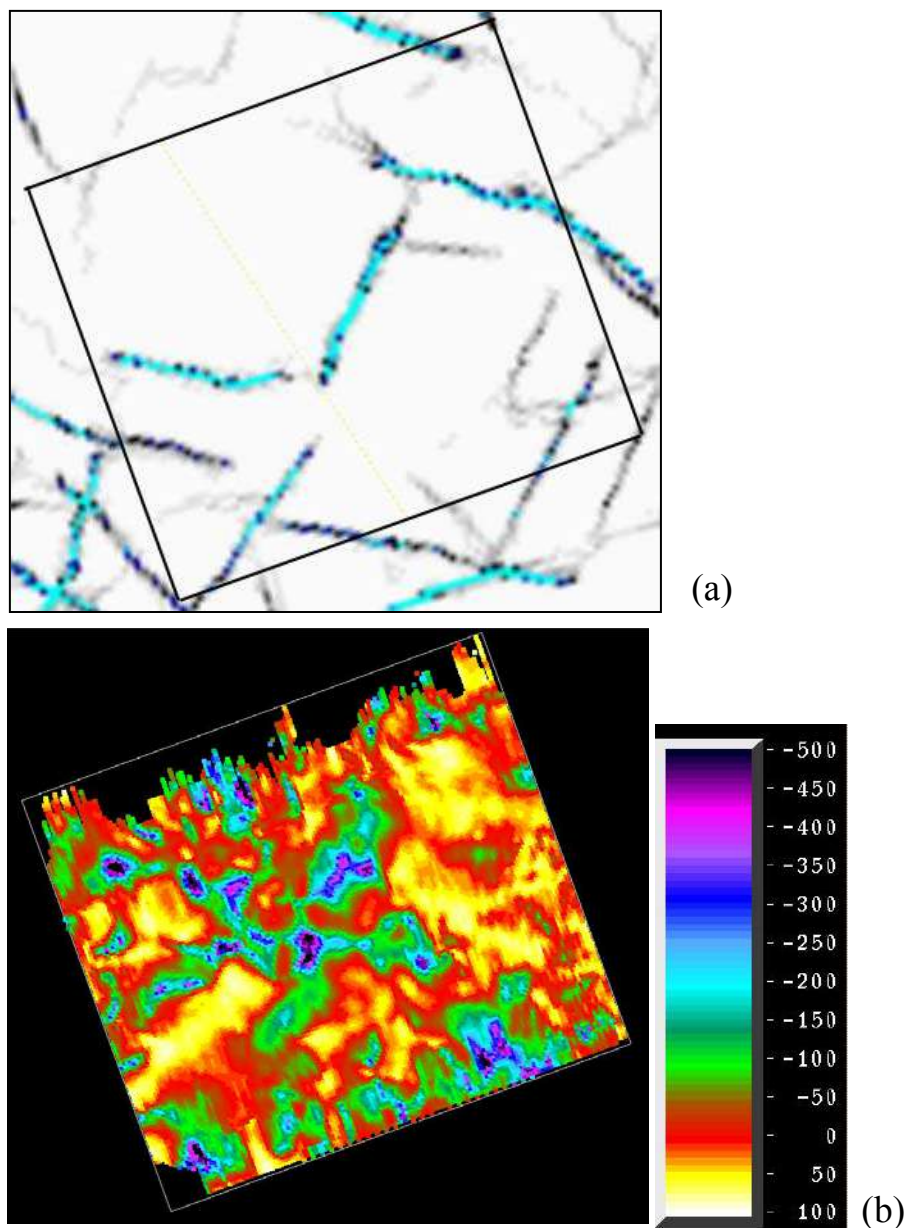


Figure 5.8: a) Time slice of ant tracking cube at 1130 ms reflecting fault pattern observed at this level. b) Shear wave splitting parameter calculated from amplitude differences between S1 and S2 over the fault pattern (50ms window). Note how the northeast stepover fault correspond to northeast anisotropy anomaly, illustrating a correspondence between fault interpretation and shear anisotropy.

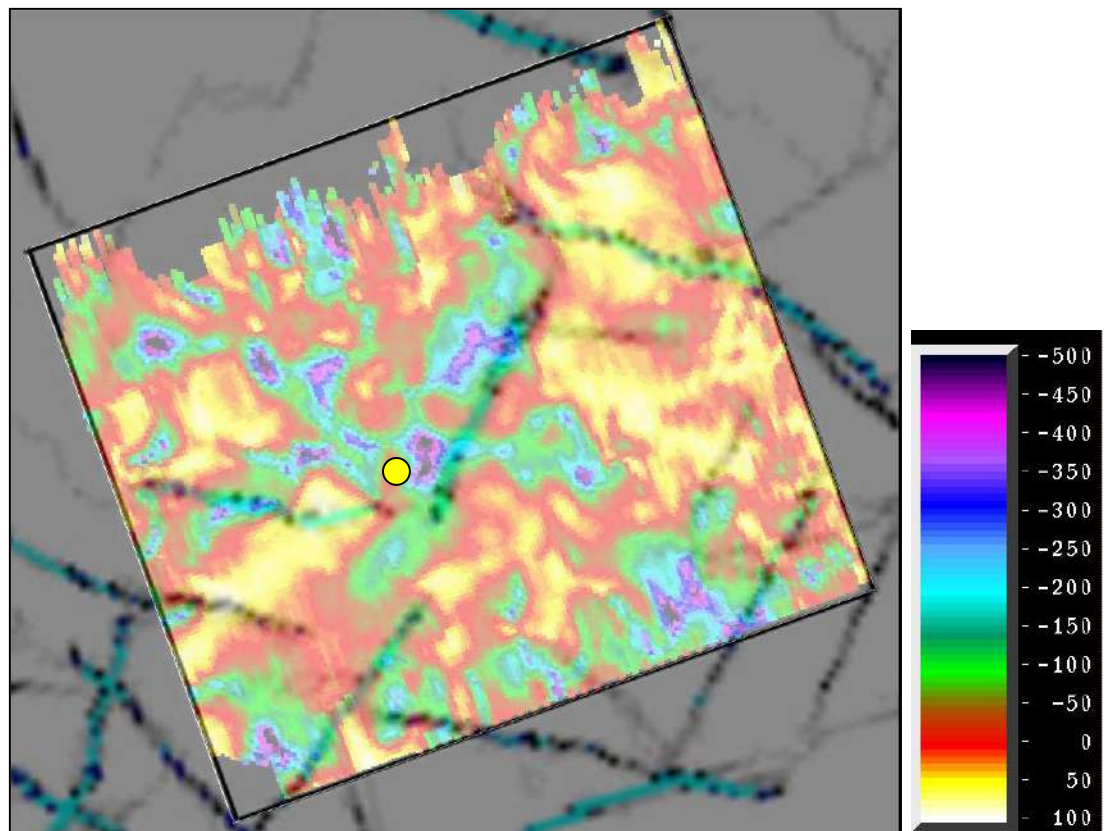


Figure 5.9: Overlay of fault pattern with amplitude variations from previous figure. Northeast stepovers correlate with negative amplitude anomaly indicating a predominant northeast fracture direction. Yellow dot represents best producing well in the field, Clough 19. Note the large negative anomaly associated with the fault block corner, where Clough 19 is located, indicating enhanced natural fracturing.

5.4 Conclusions

Analysis of the shear wave anisotropy at Rulison Field provides insight into areas of enhanced natural fracturing. Time splitting analysis provide an average estimate of the anisotropy (i.e. fracture density), whereas amplitude analysis has a much higher vertical resolution and can be used to calculate anisotropy at a much finer scale. Results show that fractures predicted from fault interpretation correspond to areas of shear anisotropy. Hence, the shear wave splitting analysis is complementary to the fault interpretation carried out with the ant tracker. Integration of these different independent data sets is critical as they serve to enhance the interpretation.

CHAPTER 6

CONCLUSIONS AND RECOMMENDATIONS

6.1 Conclusions

The work described throughout this thesis has resulted in an understanding of the fault geometry and its linkage to natural fractures at Rulison Field. From this study the following conclusions are drawn:

- The Ant Tracking software provides a significantly improved image of the subtle faults, compared to conventional fault enhancing attributes, in the reservoir interval at Rulison Field.
- The faults were interpreted to be part of a wrench fault system. Occurrence of splay faults confirmed. Wrenching and fault block rotation are the causative mechanisms for natural fracturing at Rulison Field.
- Areas of high shear wave anisotropy correspond to areas of higher fracture density. Shear wave anisotropy in conjunction with fault imaging was used to find “sweet spots” or areas of higher fracture density in Rulison Field.

6.2 Recommendations

Based on the interpretation, analysis, and conclusions presented the following recommendations are made:

- A larger multicomponent survey should be acquired in the future to enhance the imaging of the main wrench faults rather than just the area between these faults.
- The fault model and associated fracture zones should be incorporated into a 3-D geomechanical model which may help the targeting of new wells as the infill drilling program continues in the RCP study area at Rulison Field.

REFERENCES

- Armstrong, R. L., 1974. Magmatism, orogenic timing, and orogenic diachronism in the Cordillera from Mexico to Canada: *Nature*, v. 274, p. 348-351.
- Asgarov, H., 2004. Wrench faulting at Weyburn Field, Saskatchewan, M.Sc. Thesis, Colorado School of Mines.
- Berg, R. R., 1962. Mountain flank thrusting in Rocky Mountain foreland, Wyoming and Colorado: *Am. Assn. Petrol. Geol. Bull.*, v. 46. p. 2019-2032.
- Burke, L., 2005. Anisotropy from RWF 542-20 cross dipole sonic log analysis., in Keighley, D and Rumon, M., eds., *The Reservoir Characterization Project Spring 2005 report*.
- Christie-Blick, N. and Biddle, K. T., 1985. Deformation and basin formation along strike-slip faults. In: Biddle, K. T. and Christie-Blick, N. (eds.), *Strike-slip Deformation, Basin Formation, and Sedimentation: Society of Economic Palaeontologists and Mineralogists, Special Publication, 37*, p. 1-34
- Cross, T. A. and Pilger, R. H. Jr., 1978. Constraints on absolute motion and plate interaction inferred from Cenozoic igneous activity in the western United States: *Am. J. Sci.*, v. 278, p. 865-902.
- Cumella S. P., and Ostby D. B., 2003. Geology of the basin-centered gas accumulation, Piceance Basin, Colorado. *Piceance Basin 2003 Guidebook: Rocky Mountain Association of Geologists*, p. 171-193.
- Davis, T. L., 2002. Integrating data into high resolution reservoir characterization., proposal no. 6949, Colorado School of Mines.

- Dorigo, M., Maniezzo, V., and Colomi, A., 1996. The Ant System: Optimization by a colony of cooperating agents: IEEE Transactions on Systems, Man, and Cybernetics, Part-B, Vol. 26, No.1, p. 1-13.
- Dowland, K. A., 1993. Simulated Annealing. In: Reeves, C. R., (ed) Modern Heuristic Techniques for Combinatorial Problems: Blackwell Scientific Publications, Oxford, p. 20-40.
- Fletcher, Sam., 2005. Unconventional gas vital to US supply: Oil and Gas Journal, no. 28, p. 20-25.
- Hemborg, H. T., 2000. Gas Production Characteristics of the Rulison, Grand Valley, Mamm Creek, and Parachute Fields, Garfield County, Colorado: Turning Marginally Economic Basin-Centered Tight-Gas Sands into Profitable Reservoirs in the Southern Piceance Basin: Colorado Geological Survey, Resource Series 39, p. 1-30.
- Hintze, L. F., 1988. "Geologic History of Utah." Brigham Young University Geology Studies Special Publication 7, 202p.
- Higgins, S., 2005. Integrated reservoir analysis utilizing geomechanical modeling., in Keighley, D and Rumon, M., eds., The Reservoir Characterization Project Spring 2005 report.
- Gries, R., 1983. Oil and gas prospecting beneath Precambrian of foreland thrust plates in Rocky Mountains: Am. Assn. Petrol. Geol. Bull., v. 67. p. 1-28.
- Hoak, T. E. and Klawitter A. L., 1997. Prediction of Fractured Reservoir Production Trends and Compartmentalization Using an Integrated Analysis of Basement Structures in the Piceance Basin, Western Colorado. Fractured reservoirs: Characterization and Modeling Guidebook: Rocky Mountain Association of Geologists, p. 67-102.

Kendall, R. R. and Kendall, J. M., 1996. Shear-wave amplitude anomalies in south-central Wyoming: *The Leading Edge*, v. 15, p. 913-920.

Keighley, D., 2005. 2003 – 2004 P-wave time lapse cross equalization and preliminary findings., in Keighley, D and Rumon, M., eds., *The Reservoir Characterization Project Spring 2005 report*.

Kim, Y. S., Peacock, D. C. P. and Sanderson, D. J., 2004. Fault damage zones: *Journal of Structural Geology*, v. 26, p. 503-517

Kusuma, M., 2005. 1996 – 2003 Time lapse P-wave seismic analysis at Rulison field., in Keighley, D and Rumon, M., eds., *The Reservoir Characterization Project Spring 2005 report*.

Kuuskraa, V. A., T. Barrett, R. Mueller, and J. Hansen, 1997. Reservoir characterization for development of Mesaverde Group sandstones of the Piceance Basin, Colorado. *Innovative Applications of Petroleum Technology Guidebook: Rocky Mountain Association of Geologists*, Denver, Colorado, p. 254.

Kuuskraa, V. A., D. Decker and H. Lynn H. B., 1997. Optimizing Technologies for Detecting Natural Fractures in the Tight Sands of the Rulison Field, Piceance Basin, *Conference Proceedings of the Natural Gas Conference 1997*, paper NG6-3.

Lewis, C., Davis, T. L. and Vuillemoz, C., 1991. Three dimensional multicomponent imaging of reservoir heterogeneity, Silo field, Wyoming: *Geophysics, Soc. of. Expl. Geophys.*, 56, p. 2048-2056.

Lorenz, J. C., 1985. Tectonic and Stress Histories of the Piceance Creek Basin and the MWX Site, from 75 Million Years Ago to the Present. Sandia National Laboratories report SAND84-2603. 55p. (available from National Technical Information Service, Springfield, Virginia.

Lorenz, J. C., 1990. Geology, Multiwell Experiment final report, part IV. The fluvial interval of the Mesaverde Formation: Sandia National Laboratories, Report SAND 89-2612/A, p. 3.1-3.54 (pc-2).

Lorenz, J. C. and Finley, J. S., 1991. Regional Fractures II: Fracturing of Mesaverde Reservoirs in the Piceance Basin, Colorado: The American Association of Petroleum Geologists Bulletin. V. 75, No 11., p. 1738-1757.

Martin, M. A. and Davis, T. L., 1987. Shear wave birefringence – A new tool for evaluating fractured reservoirs: The Leading Edge, 06, p. 22-28.

McClay, K. and Bonora, M., 2001. Analog models of restraining stepovers in strike-slip fault systems: AAPG Bulletin, v. 85, No. 2, p. 233-260.

Mueller, M. C., 1992. Using shear waves to predict lateral variability in vertical fracture intensity: The Leading Edge, no. 2, p. 29-35.

Myal, R. F., and K. H. Frohne, 1991. Drilling the SHCT well in the Piceance Creek Basin, Colorado. Society of Petroleum Engineers Paper 21866. Society of Petroleum Engineers Joint Rocky Mountain Regional Meeting and Low- Permeability Reservoir Symposium, p. 611-622.

Ostby, D. Personal communication. 10 Mar. 2005.

Pedersen, S. “Ant Tracker” 2 May 2005. E-mail to Kjetil Jansen. 2 May 2005.

Pedersen, S., Randen, T. and Sonneland, L., 2001. Automatic extraction of fault surfaces from three-dimensional seismic data, 71st Ann. Internat. Mtg: Soc. of Expl. Geophys., p. 551-554

Petrel Workflow Tools. (Version 2004) [Computer Software Manual]. Oslo, Norway: Schlumberger Information Solutions.

Pranter, M. J., Cole, R. D., Hurley, N. F., 2003. Stratigraphic Architecture, Reservoir Characteristics, and 3-D Outcrop Modeling Using High-Resolution Laser Imaging (Lidar). Proposal, Energy and Minerals Applied Research Center, University of Colorado at Boulder.

Randen, T., Monsen, E., et al., 2000. Three-Dimensional Texture Attributes for Seismic Data Analysis: Ann. Int. Mtg., Soc. Expl. Geophys., Exp. Abstr.

Reasnor, M., 2001. Forward modeling and interpretation of multicomponent seismic data for fracture characterization, Weyburn field, Saskatchewan, M.Sc. Thesis: Golden, CO, Colorado School of Mines.

Reinecke, K. M., Rice, D. D. and Johnson, R. C., 1991. Characteristics and Development of Fluvial Sandstone and Coalbed Reservoirs of Upper Cretaceous Mesaverde Group, Grand Valley, Colorado: Rocky Mountain Association of Geologists, p. 209-225.

Seitel Data, Rulison 3D Survey Garfield County, CO. (2002). Retrived Februrary 2, 2005, from <http://www.seiteldata.com/library/us3dland/co/Rulison.pdf>

Silver, E. A., 2004. An overview of heuristic solution methods: Journal of the Operational Research Society, 55, p. 936-956.

Spencer, C. W., 1984. Pore pressure variations at the MWX site as a factor in the interpretations of in-situ stress and natural fractures. Unpublished written communication with John C. Lorenz, January 1984. In Lorenz, J. C., 1985.

Sylvester, A. G. (ed.), 1984. Wrench Fault Tectonics: AAPG Reprint Series No. 28.

Tatham, R. H. and McCormack, M. D., 1991. edited by E. B. Neitzel and D. F. Winterstein. Multicomponent Seismology in Petroleum Exploration, SEG investigation in geophysics series, no. 6., 248 p.

Thomsen, L., 1988. Reflection seismology over azimuthally anisotropic media: *Geophysics*, v. 53, no. 3, p. 304-313.

Townsend, C., Firth, I. R., Westerman, R. et al. 1998. Small seismic-scale fault identification and mapping. In: Jones, G., Fisher, Q. J. and Knipe, R. J. (eds) *Faulting, Fault Sealing and Fluid Flow in Hydrocarbon Reservoirs*: Geological Society, London, Special Publications, 147, p. 1-25.

Tweto, O., 1980. Summary of Laramide Orogeny in Colorado: Rocky Mountain Association of Geologists. 1980 Symposium, p. 129-134.

Wilcox, R. E., Harding, T. P. and Seely, D. R., 1973. Basic Wrench Tectonics. In: Sylvester, A. G. (ed.), 1984. *Wrench Fault Tectonics*: AAPG Reprint Series No. 28., p. 291-313.